Branching fraction measurements of the rare B decays $B^0 \to K^{*+}\pi^-$ and $B^0 \to K^{*0}\pi^0$.

Dominic Lavin

School of Physics
The University of Edinburgh

Thesis submitted for the degree of Doctor of Philosophy

March 26 2004

Abstract

This thesis describes analyses of the rare B meson decay channels $B^0 \to K^{*+}\pi^-$ and $B^0 \to K^{*0}\pi^0$ with final state $B^0 \to K^+\pi^-\pi^0$. The analyses use the 2002 summer data set corresponding to 88.8 million $B\bar{B}$ pairs, recorded by the BABAR experiment in runs I and II. Branching fractions of $\mathcal{BR}(B^0 \to K^{*+}\pi^-) = (8.42^{+2.51}_{-2.23}\text{ stat} \pm 0.87\text{ syst}) \times 10^{-6}$ and $\mathcal{BR}(B^0 \to K^{*0}\pi^0) = (2.1^{+1.3}_{-1.1}\text{ stat} \pm 0.6\text{ syst}) \times 10^{-6}$ were measured with an upper limit of $\mathcal{BR}(B^0 \to K^{*0}\pi^0) < 4.1 \times 10^{-6}$ at the 90% confidence level.

Acknowledgements

I would like to acknowledge the Particle Physics and Astronomy Research Council (PPARC) who provided funding during my Ph.D program. I would also like to thank my supervisor Dr. Franz Muheim for his guidance and support in the research and preparation of this thesis.

Contents

List of Figures

List of Tables

Chapter 1

Introduction

Before the 1950s, physicists believed that the electromagnetic, strong nuclear and weak nuclear interactions were invariant under the discrete symmetry operations of charge conjugation, temporal inversion and spatial inversion. The charge conjugation operation C transforms particles into their corresponding anti-particles whereas the operations of spatial P and temporal inversions T transform $(t, \bar{x}) \rightarrow (-t, -\bar{x})$. Spatial inversions are usually referred to as *parity* transformations.

In 1956, Lee and Yang [1] questioned the assumption that parity conservation held in the weak interaction. Up to this point there had been very little experimental activity in the area and parity conservation had always been assumed to hold. In 1957, the experimental work of Wu *et al* [2] on the nuclear β decay of ^{60}Co demonstrated that parity invariance was not only violated but 'maximally' violated. This maximal violation of parity was confirmed in the measurement of Goldhaber [3] demonstrating that neutrinos are always observed with negative (left-handed) helicity. In addition, C symmetry is also violated, since no left-handed anti-neutrinos are ever observed. Thus, the weak interaction separately violated C and P though was believed to conserve the combined operation of CP (Landau [4]).

In 1964, the experiment of Christenson, Fitch, Cronin and Turlay [5] first observed CP violation in the decays of neutral kaons. The effect was small but confirmed that the physics of sub-atomic particles was much more interesting than had been previously assumed. In 1967, Sakharov [6] showed that the violation of CP symmetry is a necessary requirement in order to dynamically generate baryon asymmetries in the early Universe. Thus, CP violation provides an insight into the cosmological puzzle relating to the disappearance of antimatter from the Universe.

The current understanding of sub-atomic processes and the mechanism for CP violation is contained within the Standard Model of particle physics. The Standard Model is a gauge field theory with three fermion generations consisting of quarks and leptons. Within each generation there is both an up $U = (u, c, t)$ and down $D = (d, s, b)$ type quark, one charged lepton $l = (e^-, \mu^-, \tau^-)$ and a corresponding neutrino $\nu = \nu_e, \nu_\mu, \nu_\tau$. The mediators of each force are given by the gauge bosons of the Standard Model described by the gauge symmetry group:

$$G_{SM} = SU(3)_C \times SU(2)_L \times U(1)_Y. \tag{1.1}$$

where $SU(3)_C$ generates the 8 gluon fields (g) of the strong nuclear interaction described by quantum chromodynamics (QCD). $SU(2)_L$ generates the massive gauge vector boson fields ($W^\pm, Z^0$) of the weak nuclear interaction and $U(1)_Y$ generates the photon field (γ) of the electromagnetic interaction. The strength of each interaction is determined by the coupling constants. The electro-magnetic coupling is denoted α_{EM}, the weak coupling is denoted α_W and α_s denotes the strong interaction coupling constant.

The Standard Model naturally includes a mechanism for CP violation for three quark generations. However, the observed baryon asymmetry indicates that a larger amount of CP violation is required than the Standard Model predicts.

In order to confirm whether the Standard Model is sufficient, we must test its predictions against measurements. The Standard Model predicts large CP asymmetries in the neutral $B_d\bar{B}_d$ system and the *BABAR* experiment has been designed to measure this and compare the results with the Standard Model predictions. In 2001, both the *BABAR* [7] and BELLE [8] experiments observed CP violation in the neutral B_d meson system. The current aims of each experiment are to further measure CP violation in the $B_d\bar{B}_d$ system and search for signs of physics beyond the Standard Model.

The *BABAR* detector is situated at the Stanford Linear Accelerator Center, California, where e^+e^- collisions are provided by the PEP-II collider. As PEP-II continues to achieve record luminosities, measurements of rare hadronic B decays have become possible. These decays have small branching fractions of the order $\mathcal{O}(10^{-6})$. Of particular interest are rare decays which proceed through the second order 1-loop, flavour changing neutral current transitions. These are commonly referred to as 'penguin diagrams' and are sensitive to new physics effects outside of the Standard Model. Any new physics (*e.g.* from supersymmetry) may enhance the contributions of these penguin transitions above those predicted by the Standard Model. A very promising measurement is the $\sin(2\beta)$ comparison of the tree level decay mode $B^0 \to J/\Psi K_s$ and the penguin transition decay mode $B^0 \to \phi K_s$. Significant differences in the measured values of $\sin(2\beta)$ would provide evidence for the existence of new physics.

Rare B decay amplitudes often have multiple contributions from different processes with different phase structures. Examples include the mode $B^0 \to K^{*+}\pi^-$ which contains contributions from both tree level processes and the 1-loop penguin processes. Such decay modes are excellent candidates in which to observe direct CP effects. Any enhancement of the penguin amplitudes could result in large direct CP asymmetries contradictory to the Standard Model.

This thesis presents analyses of the rare decay modes $B^0 \to K^{*+}\pi^-$ and $B^0 \to K^{*0}\pi^0$ with a data sample of $81 fb^{-1}$ corresponding to $88.9\, B\bar{B}$ pairs. Both of these decays involve penguin transitions and are thus potential probes for new physics.

Chapter 2

Theory

2.1 The Cabbibo-Kobayashi-Maskawa matrix

The Cabbibo-Kobayashi-Maskawa matrix was introduced in 1973 by Kobayashi, M. and Maskawa, T. [9] to provide a mechanism for CP violation in the Standard Model. This unitary mixing matrix transforms the massless fermions in the weak interaction basis to the physical massive fermion basis.

Massive fermions are generated from the Yukawa interactions [10] where the scalar Higgs field [11] couples to the massless fermions of the interaction basis. Equation 2.1 shows the transformations of the up type quarks and down type quarks where the states u_k^W and d_k^W represent weak eigenstates and u_i^M and d_i^M denote the mass eigenstates. The matrices U and V are unitary transformation matrices which transform to the mass basis. They arise in the diagonalisation of the mass matrix of Yukawa couplings.

$$u_i^M = \sum_{k=1}^{3} U_{ik} u_k^W, \quad d_i^M = \sum_{k=1}^{3} V_{ik} d_k^W. \tag{2.1}$$

Within the mass basis, the interactions of quarks with the charged $W^{\pm}$ gauge bosons of the weak interactions can be written as:

$$\mathcal{L}_{W^{\pm}} = -\frac{g}{\sqrt{2}} \sum_{i,j} (V_{jk} U_{ki}^{\dagger}) \bar{u}_i^M \gamma^{\mu} (1 - \gamma^5) d_j^M W_{\mu}^{\pm} + h.c. \tag{2.2}$$

where $i, j, = 1, .., 3$ denotes the three quark generations and the Cabbibo-Kobayashi-Maskawa matrix is defined as $(V_{CKM})_{ij} \equiv V_{jk} U_{ki}^{\dagger}$.

The Cabbibo-Kobayashi-Maskawa(CKM) matrix is complex and 3 dimensional and has in general 18 free parameters. Unitarity of the CKM matrix provides 9 constraints. The remaining 9 parameters can be expressed in terms of 3 Euler angles which are the independent rotations in 3 dimensions and 6 pure phases. However, some of these phases can be removed under a redefinition of the CKM elements where $V_{ud} \to e^{i(\phi_d - \phi_u)} V_{ud}$, with $d = d, s, b$ and $u = u, c, t$. This rephasing removes 5 of the 6 phases since only relative phases between fields can be observed. This leaves one remaining phase which can not be removed. It is this complex phase that allows for CP violation within the Standard Model.

The CKM matrix does not have a unique parameterisation. The standard parameterisation used by the Particle Data Group was introduced by Chau and Keung in 1984 [12]. It is given explicitly in terms of the Euler angles and one complex phase by:

$$V_{CKM} = \begin{pmatrix} 1 & 0 & 0 \\ 0 & c_{23} & s_{23} \\ 0 & -s_{23} & c_{23} \end{pmatrix} \begin{pmatrix} c_{13} & 0 & s_{13}e^{-i\delta} \\ 0 & 1 & 0 \\ -s_{13}e^{i\delta} & 0 & c_{13} \end{pmatrix} \begin{pmatrix} c_{12} & s_{12} & 0 \\ -s_{12} & c_{12} & 0 \\ 0 & 0 & 1 \end{pmatrix}$$

$$= \begin{pmatrix} c_{12}c_{13} & s_{12}c_{13} & s_{13}e^{-i\delta} \\ -s_{12}c_{13} - c_{12}s_{23}s_{13}e^{i\delta} & c_{12}c_{23} - s_{12}s_{23}s_{13}e^{i\delta} & s_{23}c_{13} \\ s_{12}c_{23} - c_{12}c_{23}s_{13}e^{i\delta} & -c_{12}s_{23} - s_{12}c_{23}s_{13}e^{i\delta} & c_{23}c_{13} \end{pmatrix} \tag{2.3}$$

where $c_{ij} \equiv \cos(\theta_{ij})$ and $s_{ij} \equiv \sin(\theta_{ij})$, θ_{ij} are the Euler rotation angles and $e^{-i\delta}$ is the complex phase which generates CP violation.

A popular parameterisation introduced by Wolfenstein[13] uses $\lambda = \sin(\theta_{12}) \simeq 0.22$ as an expansion parameter. The CKM matrix is then given in terms of the real parameters λ, A, ρ, η up to $\mathcal{O}(\lambda^3)$ as:

$$V = \begin{pmatrix} 1 - \frac{\lambda^2}{2} & \lambda & A\lambda^3(\rho - i\eta) \\ -\lambda & 1 - \frac{\lambda^2}{2} & A\lambda^2 \\ A\lambda^3(1 - \rho - i\eta) & -A\lambda^2 & 1 \end{pmatrix} + \mathcal{O}(\lambda^4). \tag{2.4}$$

In this parameterisation the unitarity of the CKM matrix only holds approximately. The CKM parameters can be determined experimentally from processes involving the weak interaction. Methods available to determine these parameters are discussed in detail in reference [14]. The current experimental bounds (90% confidence limits) for the moduli of the CKM elements are shown in equation 2.5 where the results are taken from the particle data book 2002 [15].

$$\begin{pmatrix} V_{ud} = 0.9741 - 0.9756 & V_{us} = 0.219 - 0.226 & V_{ub} = 0.0025 - 0.0048 \\ V_{cd} = 0.219 - 0.226 & V_{cs} = 0.9732 - 0.9748 & V_{cb} = 0.038 - 0.044 \\ V_{td} = 0.004 - 0.014 & V_{ts} = 0.037 - 0.044 & V_{tb} = 0.9990 - 0.9993 \end{pmatrix}. \tag{2.5}$$

2.2 The unitarity triangle

The unitarity of the CKM matrix leads to a number of conditions among its elements. Of primary importance in the B_d system is the unitarity condition shown in equation 2.6.

$$V_{ud}V_{ub}^* + V_{cd}V_{cb}^* + V_{td}V_{tb}^* = 0 \tag{2.6}$$

It can be geometrically represented as a triangle in the complex plane as shown in figure 2.1.

Typically equation 2.6 is divided by $|V_{cd}V_{cb}^*|$ and a phase convention is chosen so that $V_{cd}V_{cb}^*$ is real. This rescaling allows the three triangle vertices to be given simply by $(0,0), (1,0)$ and (ρ, η) where ρ and η are Wolfenstein parameters.

Within the Standard Model the three angles of the unitarity triangle satisfy $\alpha+\beta+\gamma = \pi$ and are defined as:

$$\alpha \equiv \arg\left(-\frac{V_{td}V_{tb}^*}{V_{ud}V_{ub}^*}\right), \; \beta \equiv \arg\left(-\frac{V_{cd}V_{cb}^*}{V_{td}V_{tb}^*}\right), \; \gamma \equiv \arg\left(-\frac{V_{ud}V_{ub}^*}{V_{cd}V_{cb}^*}\right) \tag{2.7}$$

The remaining sides of the unitarity triangle are:

$$\overline{0A} \equiv -\frac{V_{ud}V_{ub}^*}{V_{cd}V_{cb}} = \rho + i\eta, \; \overline{AB} \equiv -\frac{V_{td}V_{tb}^*}{V_{cd}V_{cb}} = 1 - (\rho - i\eta). \tag{2.8}$$

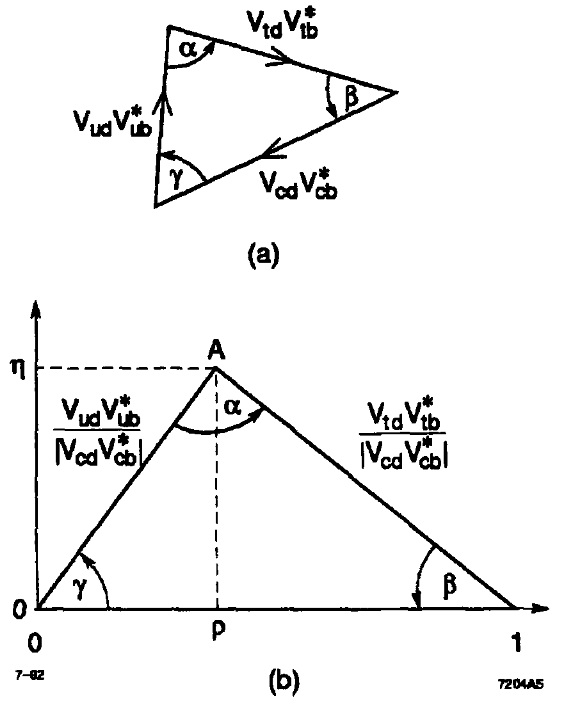

Figure 2.1: The unitarity triangle. The diagram above shows the unitary relation $V_{ud}V_{ub}^* + V_{cd}V_{cb}^* + V_{td}V_{tb}^* = 0$ in graphical form. The lower diagram shows the unitarity triangle with the sides rescaled by $V_{cd}V_{cb}^*$. The figure is reproduced from reference [16].

A common replacement which improves the precision on the ρ, η apex is given by:

$$\bar{\rho} = \rho(1 - \frac{\lambda^2}{2}), \quad \bar{\eta} = \eta(1 - \frac{\lambda^2}{2}), \tag{2.9}$$

The main aims of the *BABAR* and BELLE experiments are to measure the CKM angle β and provide constraints on the other angles γ and α which are much harder measurements. In addition, *BABAR* and BELLE will improve the precision on the values of $|V_{cb}|$ and $|V_{ub}|$.

These measurements over-constrain the unitarity triangle and will determine the level of agreement with the Standard Model picture of CP violation. Detailed discussions on the many methods available to measure these angles are given in the *BABAR* physics book [16]. Current best constraints of the unitarity triangle are shown in figure 2.2 [17]. The constraints in figure 2.2 are provided by measurements of the CP violation parameter ϵ_k from kaon decays; the $B\bar{B}$ mixing parameters Δm_s and Δm_d; $|V_{ub}|$ and $|V_{cb}|$ from $B \to X_u l\nu$ [18] [19] and $B \to X_c l\nu$ [20] [21] decays. The $\sin(2\beta)$ measurements [22] [23] provide the final constraint.

In figure 2.2 we give the world average result obtained from the heavy flavour

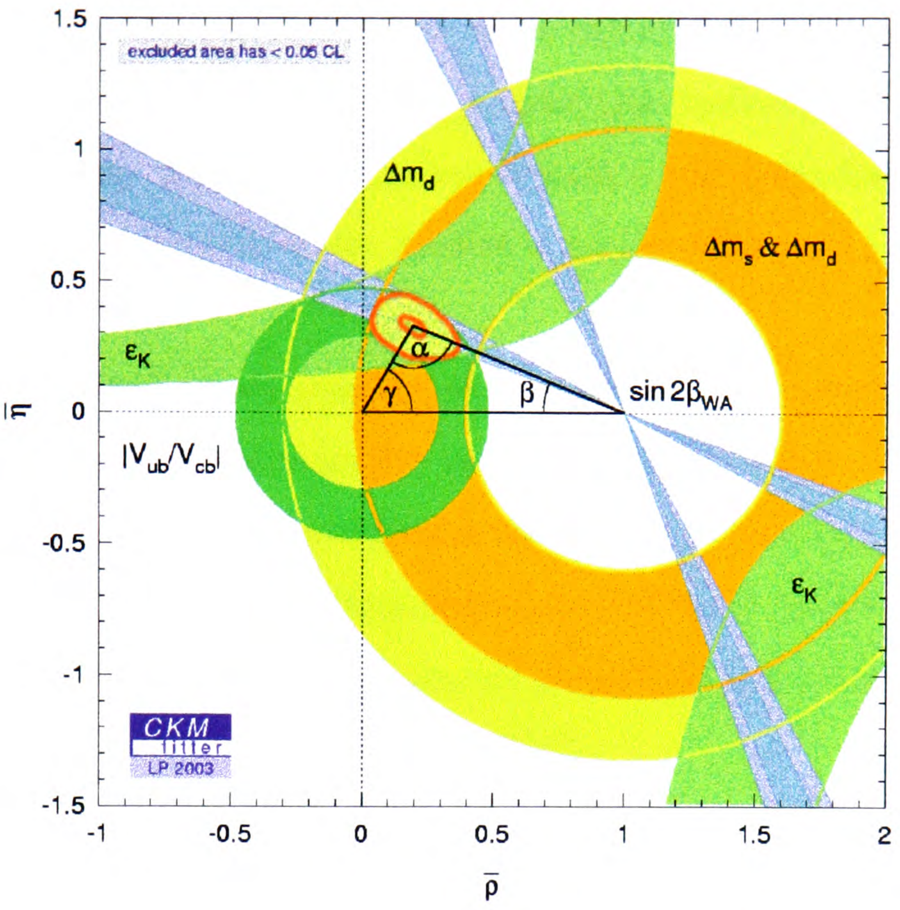

Figure 2.2: Status of the full Standard Model CKM fit in the $\bar{\rho}, \bar{\eta}$ plane showing $\sin(2\beta), \Delta m_{B_d}, \Delta m_{B_s}, \epsilon_k$ & $|V_{ub}/V_{cb}|$. The world average value for $\sin(2\beta)$ is 0.736 ± 0.049.

working group [24].

2.3 Rare hadronic B decays

Quantitatively predicting the properties of hadronic B decays is a complicated and difficult problem. The complex dynamics of these decays involve both the strong and electro-weak forces and several different energy scales including the W mass ($80\,\mathrm{GeV/c^2}$), the different quark masses and the quantum chromodynamic (QCD) scale $\Lambda_{\mathrm{QCD}} \approx 200\,\mathrm{MeV}$. The parameter Λ_{QCD} is the energy scale for quark confinement. While lowest non-vanishing order perturbation theory is sufficient for electro-weak interactions, all orders of QCD must be considered.

In QCD the strong force gauge coupling α_s is small for large energies and approaches 1.0 for low energies (e.g.Λ_{QCD}). This energy dependence allows the effects of the strong interactions at high energies to be calculated perturbatively. However, the strong interaction dynamics confining quarks into hadrons occur at lower energies where α_s is strong. Such dynamics are therefore non-perturbative in nature. It is these long-distance dynamics which present a major difficulty in calculating decay amplitudes.

In the following sections we provide an overview of the current theoretical approaches to predict decay amplitudes for rare hadronic B decays. We first introduce the effective Hamiltonian which provides the framework in which to study hadronic B decays. We then discuss the theoretical approaches of QCD factorisation and $SU(3)$ flavour symmetry where we concentrate on the theoretical predictions for the penguin dominated modes $B^0 \to K^{*+}\pi^-$ and $B^0 \to K^{*0}\pi^0$.

2.4 Effective field theory

In order to appropriately model the dynamics involved in weak hadronic B decays we must include the contributions from the strong force due to quark confinement. In contrast, the electro-weak scale which mediates the decay of the b quark is $\mathcal{O}(M_W) = 80\,\mathrm{GeV/c^2}$. Using an approach based on the operator product expansion (OPE) [25] an effective Hamiltonian is constructed which separates out the non-perturbative (long-range dynamics) and perturbative (short-range dynamics) contributions at a prescribed energy scale μ. Figure 2.3 illustrates the approach in the tree level process involving the non-local W exchange boson. Here, we see that for a prescribed energy scale where $\mu \ll M_W$ the W exchange is described by an effective local four-fermion vertex. This effective vertex describes those W exchange effects visible for energies less than μ. The effects of the W exchange at higher energy scales greater than μ are included in the $C(\frac{M_W}{\mu}, \alpha_s)$ coefficient interpreted as an effective coupling coefficient.

The effective Hamiltonian sufficient to describe $B \to K^*\pi$ decays is taken from [27] and shown below in equation 2.10:

$$\mathcal{H} = \frac{G_F}{\sqrt{2}} \sum_{p=u,c} V_{pb}V_{pD}^{*}\Big[C_1(\mu)O_1^p + C_2(\mu)O_2^p + \sum_{i=3}^{10} C_i(\mu)O_i + C_{7\gamma}(\mu)O_{7\gamma} + C_{8g}(\mu)O_{8g}\Big]. \tag{2.10}$$

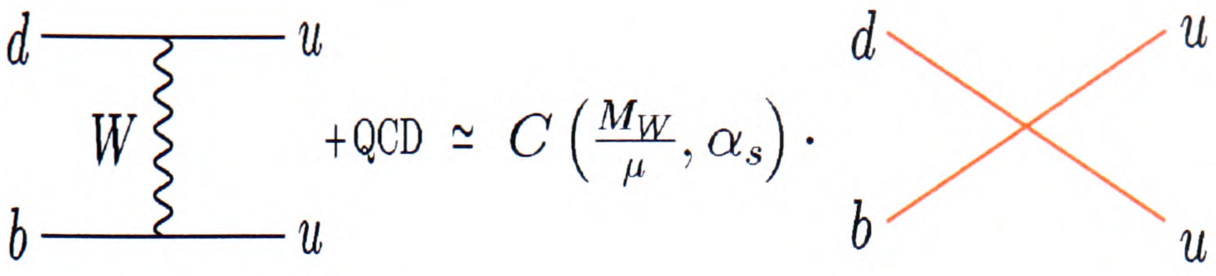

Figure 2.3: Pictorial representation of the OPE approach reproduced from reference [26].

Where $D = d, s$ depending on whether we are describing $|\Delta S| = 1$ $(b \to s)$ transitions or $|\Delta S| = 0$ $(b \to d)$ transitions. The terms $V_{pb}V^*_{pD}$ are products of the CKM matrix elements and G_F is the Fermi coupling constant. The $C_i(\mu)$ are the Wilson coefficients evaluated at the factorisation scale $\mu = \mathcal{O}(m_b)$ and the O_i are local 4-quark operators. The operators are given in detail in [28]. The Hamiltonian includes effects to order $\mathcal{O}(\alpha_s, \alpha_{\text{em}})$ where tree level W exchange contributions are represented in the effective theory by O_1 and O_2. These operators generate the $b \to u(c)q\bar{q}'$ transitions. Operators $O_3, \ldots, O_6$ arise from 1-loop 'QCD-penguins' which contribute at $\mathcal{O}(\alpha_s)$. The operators $O_7, .., O_{10}$ arise from electro-weak penguin diagrams. The 1-loop penguin diagrams provide a mechanism for the neutral flavour changing $b \to s(d)q\bar{q}$ transitions. Figure 2.4 shows graphically, the tree level, QCD and electro-weak penguin transistions.

The final terms O_{8g} and $O_{7\gamma}$ represent the chromomagnetic and electromagnetic dipole operators. Operators $O_{2,3,5,8,10}$ represent colour suppressed tree, QCD and electro-weak penguin diagrams. Using the effective Hamiltonian of equation 2.10, decay amplitudes for hadronic B decays $B \to M_1M_2$ can be determined as:[1]

$$\mathcal{A}(B \to M_1M_2) = \langle M_1M_2|\mathcal{H}|B\rangle = \sum_i C_i(\mu)\langle M_1M_2|O_i|B\rangle(\mu) + \mathcal{O}(\frac{k^2}{M_W^2}), \tag{2.11}$$

where M_i, $i = 1, 2$ represent the two final state mesons. The $C_i(\mu)$ are the Wilson coefficients which contain all effects of QCD dynamics above the factorisation scale μ (short-distance physics). The Wilson coefficients $C_i(\mu)$ are initially calculated at

---

[1] up to small power corrections $\mathcal{O}(\frac{k^2}{M_W^2})$ where k^2 is the W momentum

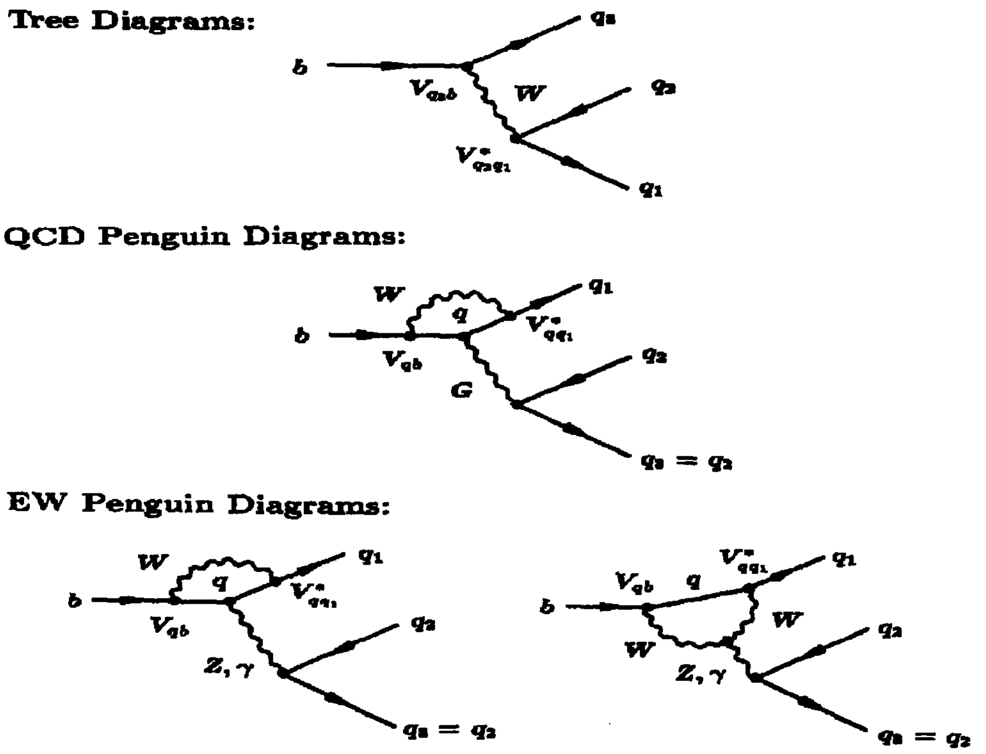

Figure 2.4: Graphical representation of tree level, QCD and electro-weak penguin transitions for hadronic b quark decays.

the required order in the full theory at the energy scale $\mu_W = \mathcal{O}(M_W, m_t)$. Once determined they are evolved from μ_W down to $\mu = \mathcal{O}(m_b)$ using the renormalisation group techniques as described in the literature [25]. All the low-energy contributions below μ (long-distance physics) are contained in the matrix elements $\langle M_1 M_2 | O_i | B \rangle$. The calculation of the matrix elements $\langle M_1 M_2 | 0_i | B \rangle$ is an extremely difficult problem since they must be calculated using non-perturbative methods an example of which is Lattice QCD. Details on the method can be found in reference [29].

2.5 QCD factorisation

This section introduces the theoretical approach of QCD factorisation for $B \to M_1 M_2$ decays where M_1 and M_2 are light mesons e.g. $B^0 \to K^{*+}\pi^-$, $B^0 \to K^{*0}\pi^0$. All of the theoretical work in this area is concerned with the calculation of the matrix elements $\langle M_1 M_2 | O_i | B \rangle$. Previous approaches have assumed that the weak decay matrix elements involving a local four fermion operator can be factorised as:

$$\langle M_1 M_2|O_i|B\rangle = \langle M_1|j_1^\mu|B\rangle\langle M_2|j_2^\mu|0\rangle = F^{B\to M_1} f_{M_2}. \tag{2.12}$$

where j_1^μ and j_2^μ are interaction currents and $|0\rangle$ represents the vacuum state. $F^{B\to M_1}$ is a non-perturbative hadronic decay form factor describing the $B \to M_1$ decay and f_{M_2} is the decay constant of the final state particle M_2. We illustrate the approach with the $B^0 \to K^{*+}\pi^-$ decay involving the $b \to u[s\bar{u}]$ tree level process corresponding to operator $O_1 = (\bar{u}b)_{V-A}(u\bar{s})_{V-A}$, $M_1 = \pi^-$ and $M_2 = K^{*+}$ where we obtain from equation 2.12:

$$\langle \pi^- K^{*+}|O_1|B_d^0\rangle = \langle \pi^-|(\bar{u}b)_{V-A}|B\rangle\langle K^{*+}|(u\bar{s})_{V-A}|0\rangle = F^{B\to\pi} f_{K^*}. \tag{2.13}$$

This approach assumes that the (BM_1) system and the M_2 system completely decouple from each other and neglects gluon exchange between the two systems. The QCD factorisation approach extends this method to include $\mathcal{O}(\alpha_s)$ corrections to the factorised matrix elements of equation 2.12. In essence, QCD factorisation tries to disentangle hard and soft gluon exchange using a hard scattering approach to evaluate the hard contributions and showing that the effects of soft gluon exchange are suppressed by a factor $\mathcal{O}(\Lambda/Q)$. Here, Q denotes the hard scattering scale, typically the mass of the b quark denoted by m_b. Hadronic matrix elements are evaluated within QCD factorisation using formula 2.14 [30] which is illustrated in figure 2.5. Equation 2.14 is the leading term of the heavy quark expansion in $1/m_b$ and α_s, relying on the fact that $m_b \gg \Lambda_{QCD}$ and soft collinear factorisation arguments.

$$\begin{aligned}\langle M_1 M_2|O_i|B\rangle = F^{B\to M_1} &\int_0^1 du T_i^I(u)\Phi_{M_2}(u)\\ &+ \int_0^1 d\eta du dv T_i^{II}(\eta, u, v)\Phi_B(\eta)\Phi_{M_1}(u)\Phi_{M_2}(v).\end{aligned} \tag{2.14}$$

Each of the $\Phi_X(u), \Phi_X(v), \Phi_X(\eta)$ are the momentum distribution amplitudes of the meson $X = M_1, M_2, B$ [30] where u, v, η denote momemtum. $F^{B\to M_1}$ is a form factor which includes the non-perturbative long distance effects. $T^{I,II}$ are the perturbatively calculable hard scattering kernels containing contributions arising from the inclusion

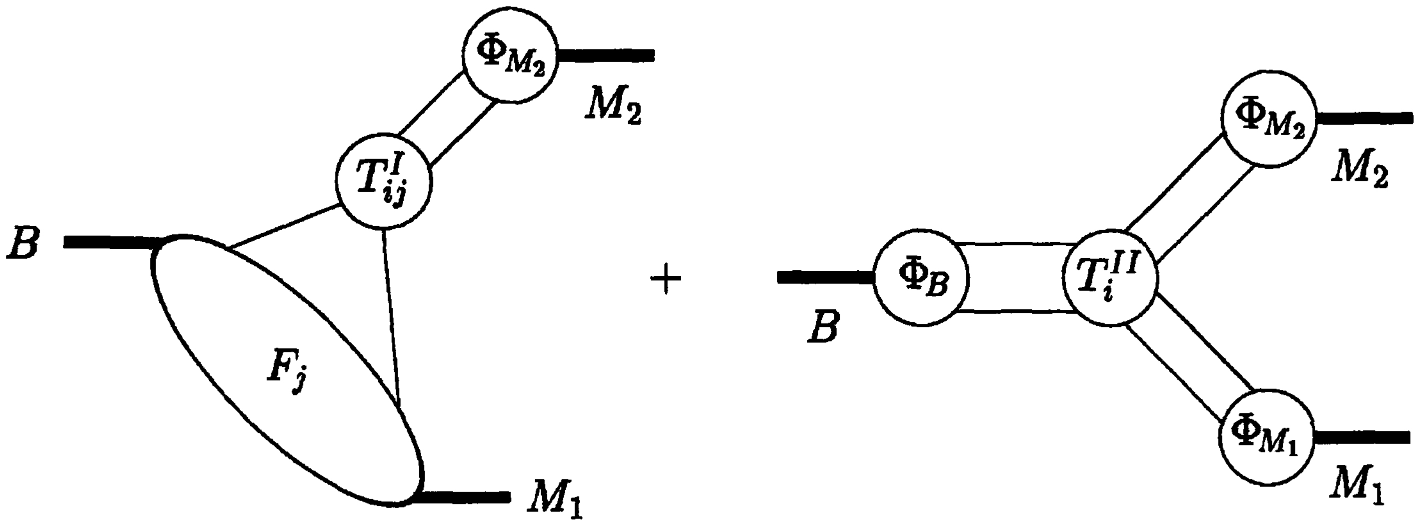

Figure 2.5: Graphical representation of the QCD factorisation formula taken from [30].

of non-factorisable corrections to the matrix element. The term non-factorisable refers to the inclusion of hard gluon exchange between the (BM_1) and M_2 systems. Corrections are obtained at $\mathcal{O}(\alpha_s)$ from leading order, penguin, electro-weak penguin and the $\mathcal{O}(\Lambda/m_b)$ hard spectator contributions which are shown in figure 2.6.

Contributions from weak annihilation effects where the spectator quark is annihilated in the decay are not calculable within QCD factorisation. Attempts to integrate the Φ distributions break down as the integrals become infinite. However, although annihilation contributions are non-calculable they are suppressed by a factor f_B/m_b and are treated as higher order power corrections. These power corrections from weak annihilation are parameterised respectively by the complex parameter:

$$X_A = (1 + \rho_A e^{i\phi_A}) \ln \frac{m_B}{\Lambda_h}, \quad \rho \leqslant 1, \Lambda_h = 0.5\,\text{GeV}. \tag{2.15}$$

where ϕ_A is an arbitrary strong (QCD) phase due to possible soft rescattering effects. Soft gluon exchange for the spectator scattering contribution is also non-calculable within QCD factorisation. This contribution is also suppressed and it is parameterised by another complex parameter X_H which has the same form as X_A. Thus, all soft gluonic exchanges between the M_2 and (BM_1) systems are suppressed by at least one power of $\mathcal{O}(\Lambda/m_b)$.

The results of calculating the hard scattering kernels $T^{I,II}$ are described by the coefficients $a_i(M_1M_2)$. The general form of the QCD factorisation $a_i(M_1M_2)$ coefficients

(a) Gluonic vertex corrections

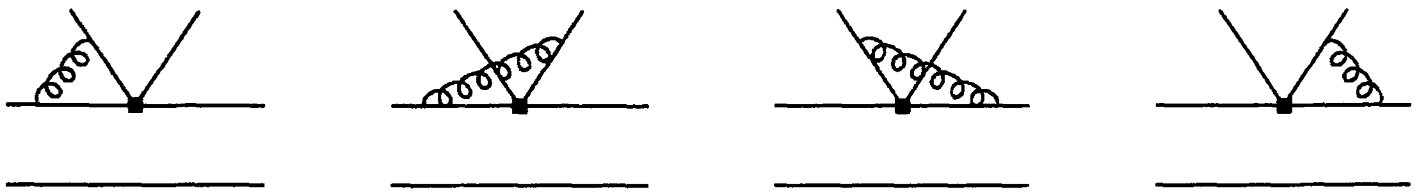

(b) 1 loop radiative corrections

(c) Hard spectator corrections

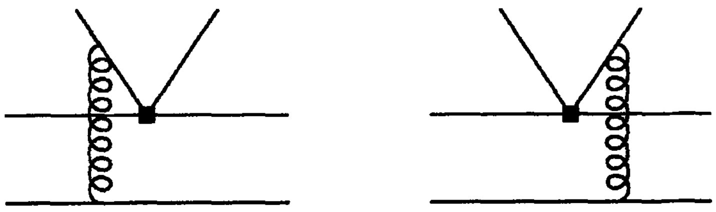

(d) Non-calculable suppressed annihilation corrections

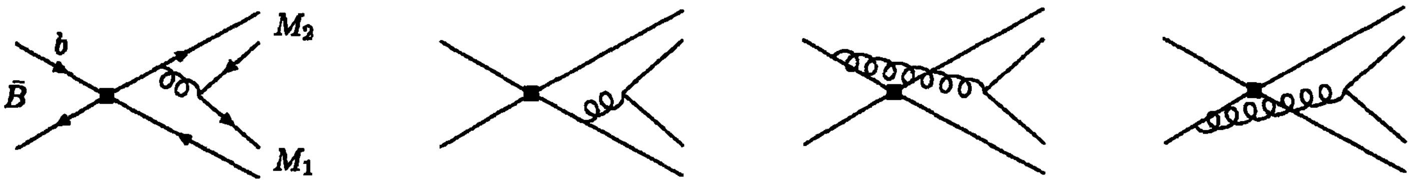

Figure 2.6: Next-to-leading order contributions to the a_i coefficients determined by the calculation of the hard scattering kernels $T^{I,II}$.

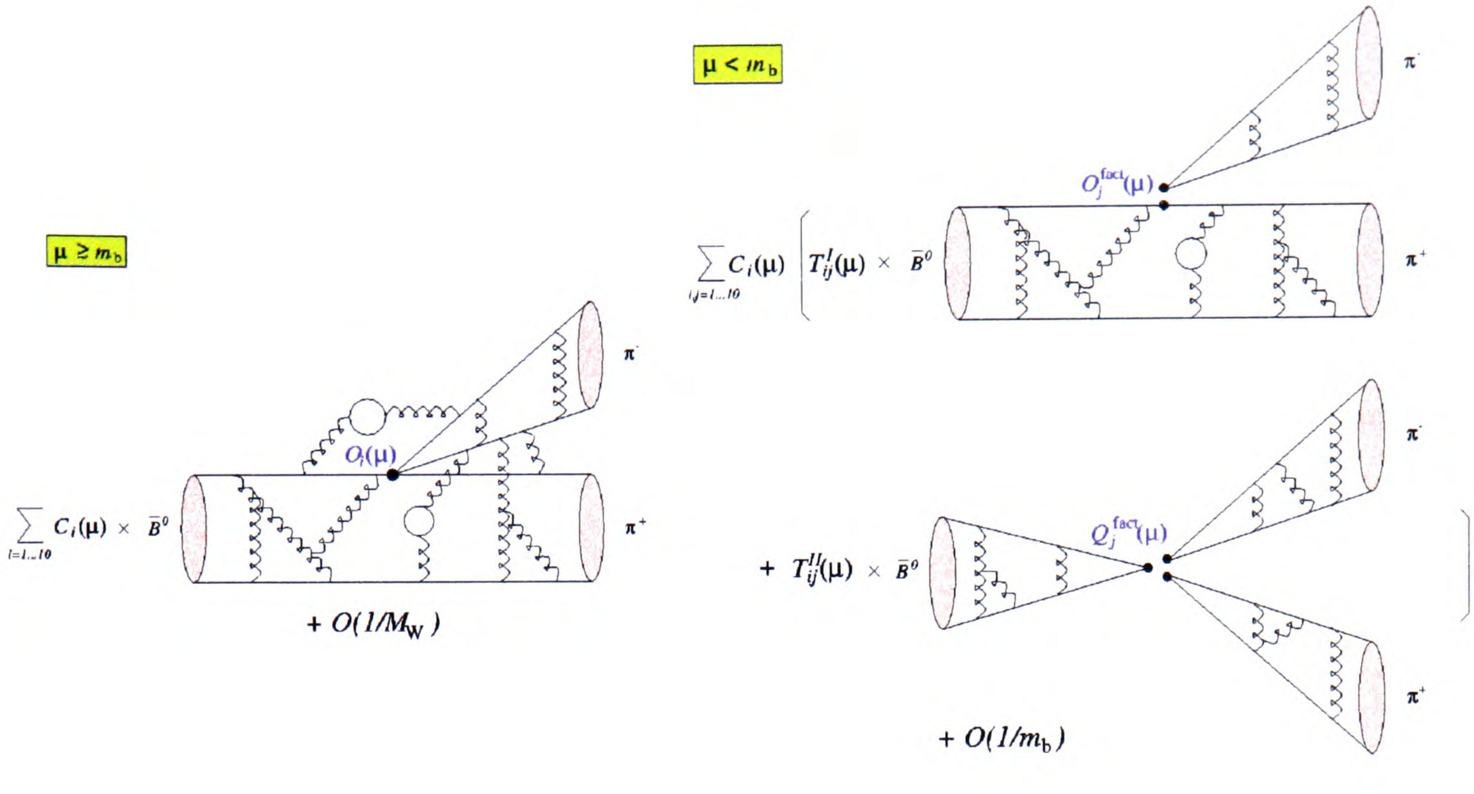

Figure 2.7: Diagram of the full calculation showing the use of OPE and QCD factorisation The figure shown is for the decay mode $B^0 \to \pi^+\pi^-$ reproduced from reference [31].

at next-to-leading order are given [27] by:

$$\begin{aligned} a_i(M_1M_2) &= (C_i + \frac{C_{i\pm1}}{N_C})N_i(M_2) \\ &+ \frac{C_{i\pm1}}{N_C}\frac{C_F\alpha_s}{4\pi}[V_i(M_2) + \frac{4\pi^2}{N_C}H_i(M_1M_2)] + P_i(M_2)\,, \end{aligned} \tag{2.16}$$

where the upper (lower) sign applies when i is odd (even). N_C is the numbers of QCD colours and the leading order coefficient N_i is the normalisation integral for the relevant distribution amplitude Φ_{M_2}. The contribution $V_i(M_2)$ is due to the vertex corrections, $H_i(M_1M_2)$ comes from hard spectator corrections and $P_i(M_1M_2)$ is the contribution from penguin contractions. We may now write each contributing matrix element of the amplitude given in equation 2.11 in the QCD factorised form as:

$$\langle M_1M_2|O_i|B\rangle = a_i \times F^{B\to M_1} \times f_{M_2}. \tag{2.17}$$

The calculation is illustrated [31] in figure 2.7.

2.5.1 Predictions for $B^0 \to K^{*+}\pi^-$ and $B^0 \to K^{*0}\pi^0$

Theoretical predictions based on the QCD factorisation approach depend on a number of assumptions and are dominated by the parameterisation of the power corrections arising from annihilation contributions (X_A). Following reference [27] we neglect contributions due to weak annihilation where the spectator quark is annihilated in the decay. For $B^0 \to K^{*0}\pi^0$ the colour suppressed electro-weak penguin contributions are also neglected.

The $B^0 \to K^{*0}\pi^0$ and $B^0 \to K^{*+}\pi^-$ decay amplitudes[2] at leading order $\mathcal{O}(\Lambda_{\mathrm{QCD}}/m_b)$ are given in equation 2.18:

$$\begin{aligned} \mathcal{A}_{B^0\to K^{*+}\pi^-} &= \sum_{p=u,c} V_{pb}V_{ps}^*\left\{A_{K^*\pi}\left[\delta_{pu}\alpha_1 + \alpha_4^p + \beta_3^p\right]\right\}, \\ \sqrt{2}\mathcal{A}_{B^0\to K^{*0}\pi^0} &= \sum_{p=u,c} V_{pb}V_{ps}^*\left\{A_{K^*\pi}\left[-\alpha_4^p - \beta_3^p\right] + A_{\pi K^*}\left[\delta_{pu}\alpha_2 + \frac{3}{2}\alpha_{3,EW}^p\right]\right\}. \end{aligned} \tag{2.18}$$

where δ_{pu} is the Kronecker delta. The α_i coefficients are linear combinations of the a_i coefficients given in equation 2.16 introduced in the 2003 paper by Beneke and Neubert. For more information see the reference [27]. Each coefficient α_i represents the contribution from the process which generated its operator O_i. Therefore, α_1 is due to the tree level process, α_2 is due to the colour suppressed tree level process. $\alpha_{3,EW}$ is the dominant electro-weak contribution. α_4 denotes the QCD penguin contribution. The β_3 contribution is from gluonic hard scattering terms arising from the hard spectator scattering contribution. The terms $A_{\pi K^*}$ and $A_{K^*\pi}$ are given by:

$$\begin{aligned} A_{K^*\pi} &= -2im_{K^*}\frac{G_F}{\sqrt{2}}\epsilon_{K^*}^* p_B A_0^{B\to K^*}(0)f_\pi, \\ A_{\pi K^*} &= -2im_{K^*}\frac{G_F}{\sqrt{2}}\epsilon_\pi^* p_B F_+^{B\to\pi}(0)f_{K^*}, \end{aligned} \tag{2.19}$$

where F_+ and A_0 denote pseudoscalar (P) and vector (V) meson form factors which parameterise the long range dynamics. The term ϵ^* is the polarisation of the vector meson and f_M, $M = K^*, \pi$ are the meson decay constants where for the vector K^*

---

[2] This includes all contributions at $\mathcal{O}(\Lambda_{\mathrm{QCD}}/m_b)$.

Mode	Theory QCD $\mathcal{BR}(10^{-6})$ factorisation	Experiment $\mathcal{BR}(10^{-6})$		
		BABAR	BELLE [32]	CLEO [33]
$B^0 \to K^{*0}\pi^0$	$2.5^{+0.1+0.5+0.3+2.6}_{-0.1-0.4-0.3-0.5}$	-	< 3.5	< 3.6
$B^0 \to K^{*+}\pi^-$	$8.1^{+1.4+1.3+0.8+6.2}_{-1.2-1.2-0.8-1.6}$	-	$14.8^{+4.6+2.8}_{-4.4-1.3}$	$16^{+6}_{-5} \pm 2$

Table 2.1: Branching fractions for $\mathcal{BR}(B \to K^*\pi)$ modes from QCD factorisation and measured values from the *BABAR*, BELLE and CLEO experiments.

meson f refers to a longitudinal polarised meson. Table 2.1 shows the QCD factorisation predictions from [27] for the modes $B^0 \to K^{*0}\pi^0$ and $B^0 \to K^{*+}\pi^-$ along with the current measured branching fractions.

There are large theoretical errors in the QCD factorisation predictions. The errors given on the predictions in table 2.1 come from a variety of sources. The first error corresponds to the variation in the CKM parameters $|V_{cb}|$, $|V_{ub}/V_{cb}|$, and the CKM angle γ which is varied in the range 70 ± 20^o. The second and third errors are more theoretical in nature. The origins of these errors include the variation of the quark masses, form factors, decay constants and uncertainties arising from the calculation method. More detailed information can be found in [27]. The final error arises due to size estimates of the power corrections parameterised by X_A and X_H.

2.6 $SU(3)$ flavour symmetry

Here we introduce the approach to charmless hadronic B decays based on $SU(3)$ flavour symmetry of the u, d, s quarks. $SU(3)$ flavour symmetry generalises isospin symmetry by assuming that the u, d, s quarks are indistinguishable to the strong force. For example, under $SU(3)$ flavour symmetry the strong force dynamics for the decay modes $B^0 \to \pi^+\pi^-$ and $B^0 \to K^+\pi^-$ would be identical. $SU(3)$ flavour symmetry is not exact since the mass of the strange quark is larger than the u, d quarks. In the $SU(3)$ flavour symmetry approach [34] symmetry breaking effects are parameterised by the ratio of the kaon and pion decay constants f_K/f_π.

2.6.1 Diagrammatics

In 1981 Zeppenfeld [35] showed that under $SU(3)$ flavour symmetry the weak Hamiltonian given in equation 2.10 contains only five possible $SU(3)$ invariant amplitudes. These $SU(3)$ amplitudes can be related to a set of five independent combinations of the six decay diagrams that construct all decays of B mesons. The three dominant decay diagrams consist of the tree, colour suppressed tree and QCD penguin. The remaining three diagrams involve the decay of the spectator quark and are described as the weak exchange, weak annihilation and penguin annihilation diagrams [36].

Decay amplitudes within the $SU(3)$ approach are constructed using the four dominant independent amplitudes consisting of a tree contribution T; a colour-suppressed contribution C; a penguin contribution P and a singlet penguin contribution S (where the colour singlet $q\bar{q}$ pair forms an $SU(3)$ flavour singlet state e.g.η). The smaller electro-weak contributions P_{EW} are included as in the references [36] [37] where they are combined with T, C, P and S into the amplitudes denoted t, c, p, s shown in equation 2.20. The analysis neglects contributions from the smaller weak exchange, weak annihilation and penguin annihilation diagrams which involve the annihilation of the spectator quark.

$$\begin{aligned} t &\equiv T + P^C_{EW}, & c &\equiv C + P_{EW}, \\ p &\equiv P - \frac{1}{3}P^C_{EW}, & s &\equiv S - \frac{1}{3}P_{EW}. \end{aligned} \tag{2.20}$$

2.6.2 Analysis method

The $SU(3)$ approach does not attempt an explicit calculation of matrix elements. Rather, in the analysis [34] a fit to the available data is performed to extract magnitudes and phases for the $SU(3)$ amplitudes (t, p, c, s). Once these are determined, predictions can be made for a large range of B decay modes. The fit uses measurements of modes with well determined $SU(3)$ amplitudes. An example is $B^+ \to K^{*0}\pi^+$ which is a pure penguin mode that directly determines the amplitude p. The fit requires as input the measurements from the decays $B^0 \to K^{*+}\pi^-$ which involves both t and p and $B^0 \to K^{*0}\pi^0$ involving the amplitude c.

2.6.3 $SU(3)$ predictions for $B^0 \to K^{*+}\pi^-$ and $B^0 \to K^{*0}\pi^0$

The decay diagrams for the $B^0 \to K^{*+}\pi^-$ and $B^0 \to K^{*0}\pi^0$ modes are shown in figures 2.8 and 2.9. Table 2.2 gives the results from the $SU(3)$ analysis [34] for different values of the CKM phase $\gamma = 63^o, 26^o, 162^o$. These values are chosen as they correspond to minima from the fit. The amplitude expressions shown are standard in the literature [36] [37] [34]. The primed notation denotes that the transitions are $|\Delta S| = 1$. The p subscript denotes that the spectator quark is included in the pseudo-scalar meson (π). The v subscript denotes that the spectator quark is included in the vector meson (K^*).

Mode	Amplitude	Theory $SU(3)$ $\mathcal{BR}(10^{-6})$		
		$\gamma = 26^o$	$\gamma = 63^o$	$\gamma = 162^o$
$B^0 \to K^{*0}\pi^0$	$-\frac{1}{\sqrt{2}}(c_v^{'} - p_p^{'})$	$1.3^{+1.3}_{-0.7}$	$0.8^{+1.0}_{-0.6}$	$0.7^{+1.0}_{-0.3}$
$B^0 \to K^{*+}\pi^-$	$-(t_p^{'} + p_p^{'})$	$15.3^{+1.3}_{-1.1}$	12.4 ± 0.9	$15.5^{+1.2}_{-1.1}$

Table 2.2: Branching fraction predictions from $SU(3)$ flavour symmetry for the modes $B^0 \to K^{*+}\pi^-$ and $B^0 \to K^{*0}\pi^0$.

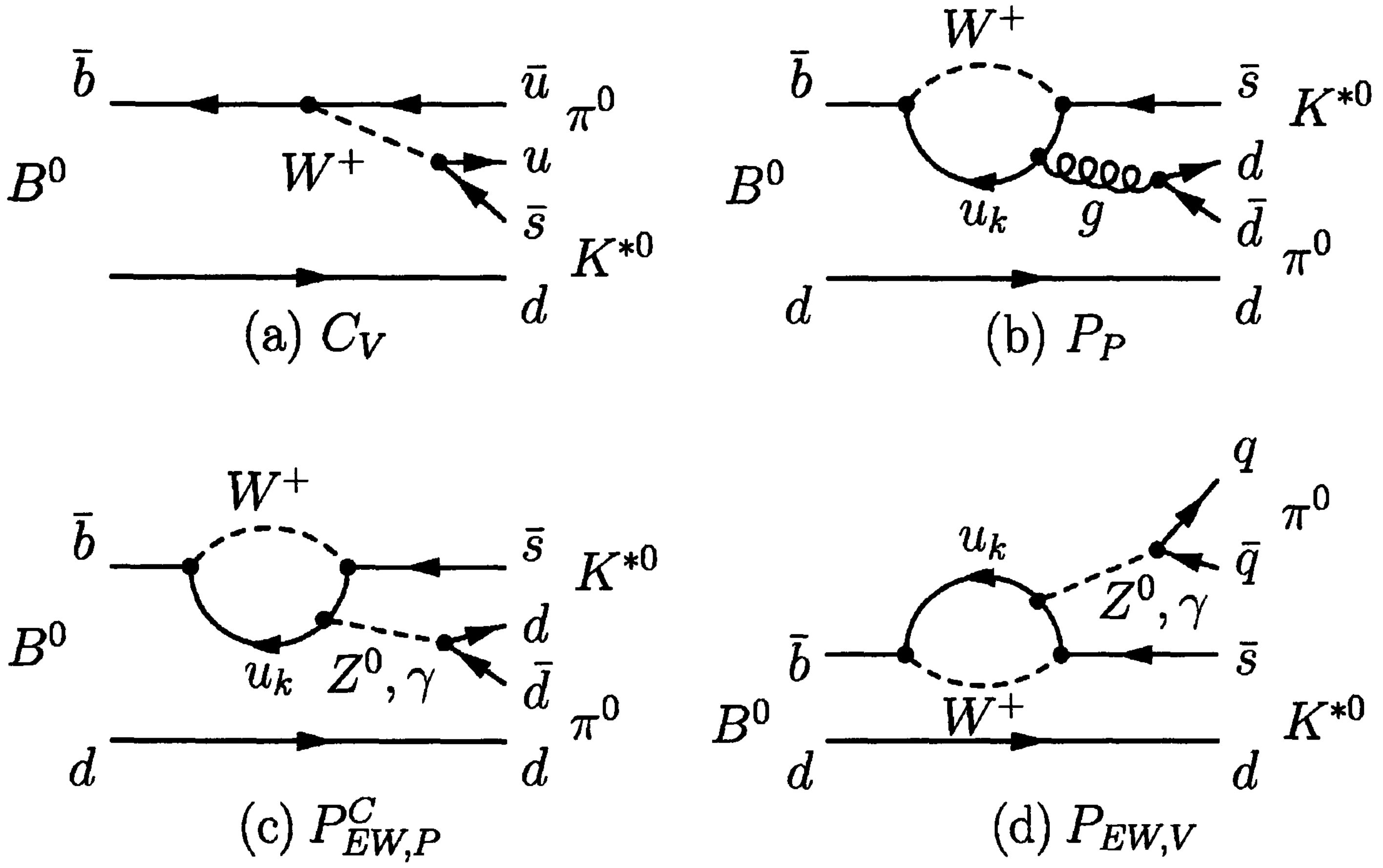

Figure 2.8: Decay diagrams for $B^0 \to K^{*0}\pi^0$.

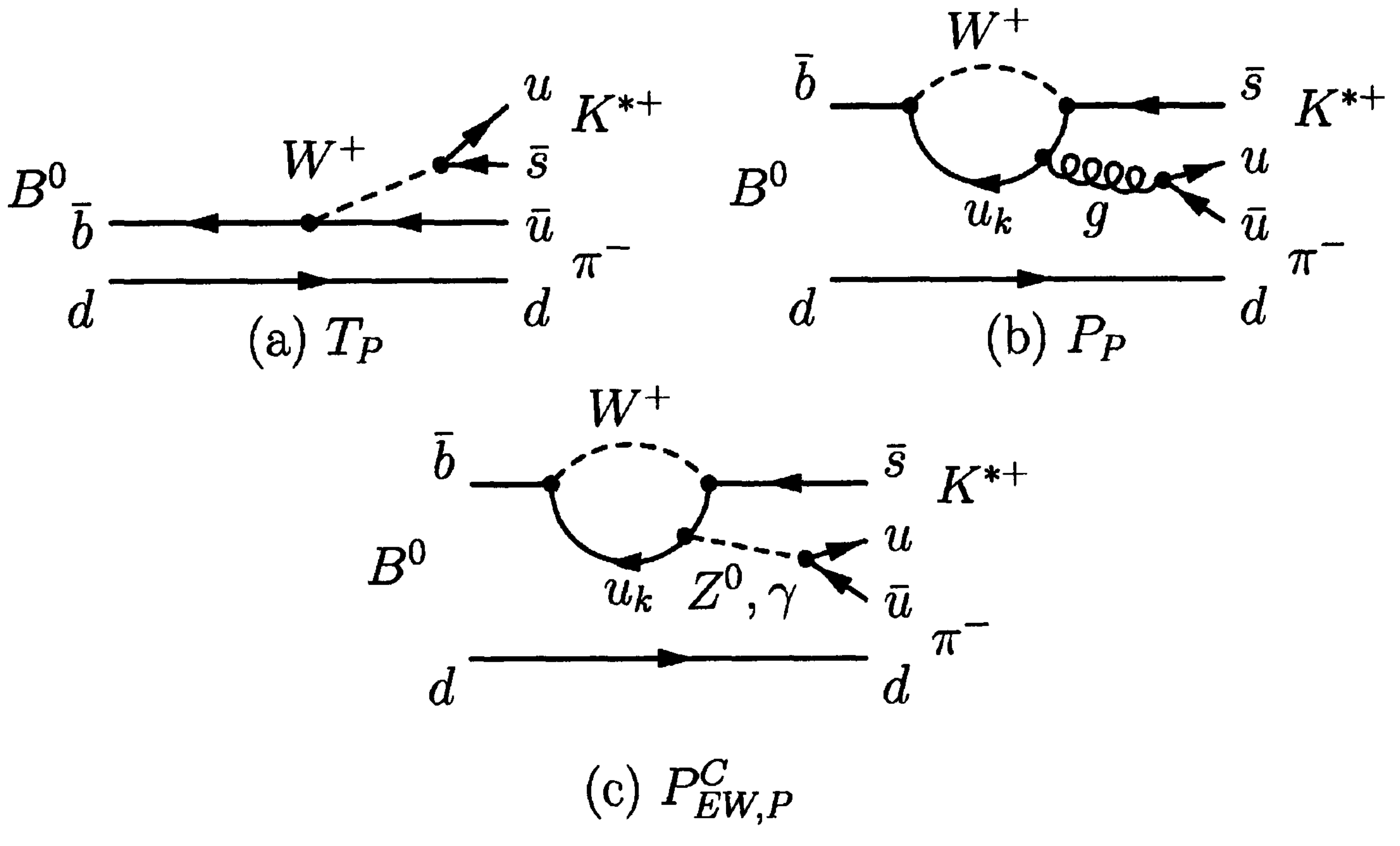

Figure 2.9: Decay diagrams for $B^0 \to K^{*+}\pi^-$.

Chapter 3

The *BABAR* detector

In this chapter we give an overview of the *BABAR* detector and the PEP-II collider which provides the electron positron ($e^{-}e^{+}$) collisions. We first describe the PEP-II collider based at the Stanford Linear Accelerator Center U.S.A and then discuss each subdetector of the *BABAR* detector.

3.1 The PEP-II collider

PEP-II is an asymmetric $e^{+}e^{-}$ collider designed to operate at a center of mass energy 10.58 GeV corresponding to the mass of the $\Upsilon(4S)$ resonance. The $\Upsilon(4S)$ decays exclusively to $B^{0}\bar{B}^{0}$ and $B^{+}B^{-}$ meson pairs providing an excellent laboratory in which to study the physics of B mesons.

The electron and positron energies are respectively, 9.0 GeV and 3.1 GeV and introduce a Lorentz boost factor of $\beta\gamma = 0.56$ to the $\Upsilon(4S)$. This boost is essential in order to separate the two B meson decay vertices which is required for time-dependent CP measurements.

The *BABAR* detector is required to measure B decay modes with small branching fractions of $\mathcal{O}(10^{-6})$. To acheive this goal we require a machine with a high luminosity of $\mathcal{L} = \mathcal{O}(10^{34})\,\mathrm{cm}^{-2}\mathrm{s}^{-1}$. Figure 3.1 shows the layout of the PEP-II storage rings and linear accelerator (LINAC) used as the injection system into the PEP-II storage rings. Detailed descriptions of PEP-II and its performance can be found in references [38] and [39].

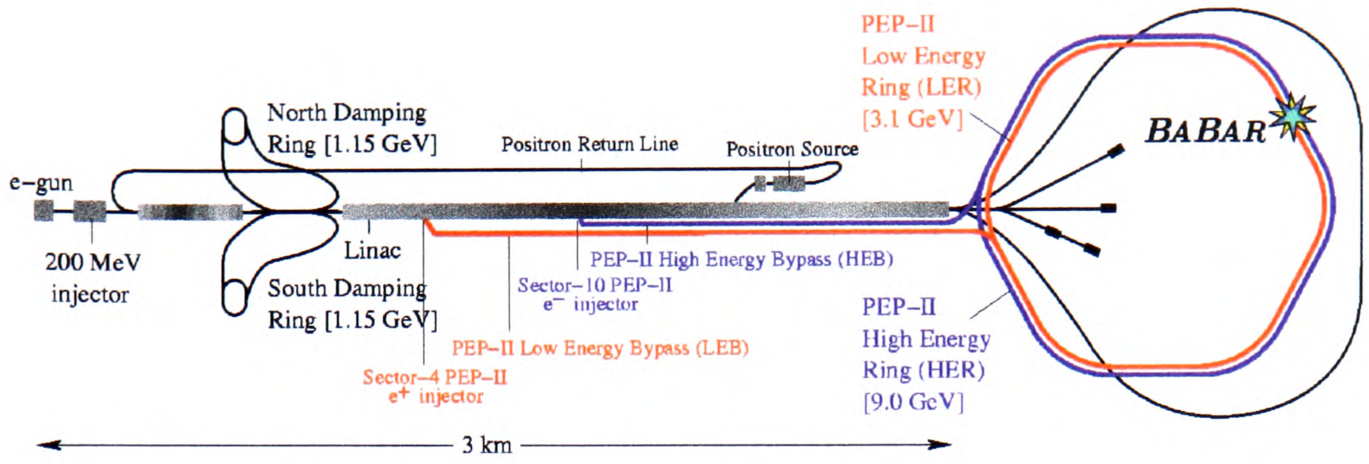

Figure 3.1: Layout of the PEP-II storage rings and linear accelerator based at SLAC.

3.2 The *BABAR* interaction region (IR)

Figure 3.2 shows the layout of the *BABAR* interaction region (IR). The dipole magnet B1 is used to separate the beams in the horizontal plane and QD1 is the first focusing quadrupole magnet into the interaction region. The quadrupoles QD1 and QD2 (1-3m) focus the low energy beam (LER) in the horizontal and vertical planes respectively. The quadrupoles QD4 and QD5 (4-7m) are responsible for the focusing of the high energy beam (HER). The design requirements and layout of the interaction region result in significant synchrotron radiation directly into the interaction region. This radiation arises due to the requirements of large beam currents (2.14 A) and occurs when the beam passes the magnets B1 and QD1. A number of measures [39] have been implemented to transfer the synchrotron radiation away from the interaction region. This has reduced the backgrounds to relatively low levels which have presented little problems. Other backgrounds arise from residual beam-gas interactions in the beampipe and beam-beam collisions resulting in electromagnetic showers into the interaction region. At the interaction point (IP) the beam sizes are 155 μm in the horizontal plane and 6.2 μm in the vertical plane with a bunch length of 1.0 cm.

3.3 The *BABAR* co-ordinate system

The system of co-ordinates used for the *BABAR* detector is defined as follows;

- The z-axis is directed along the direction of the electron beam.

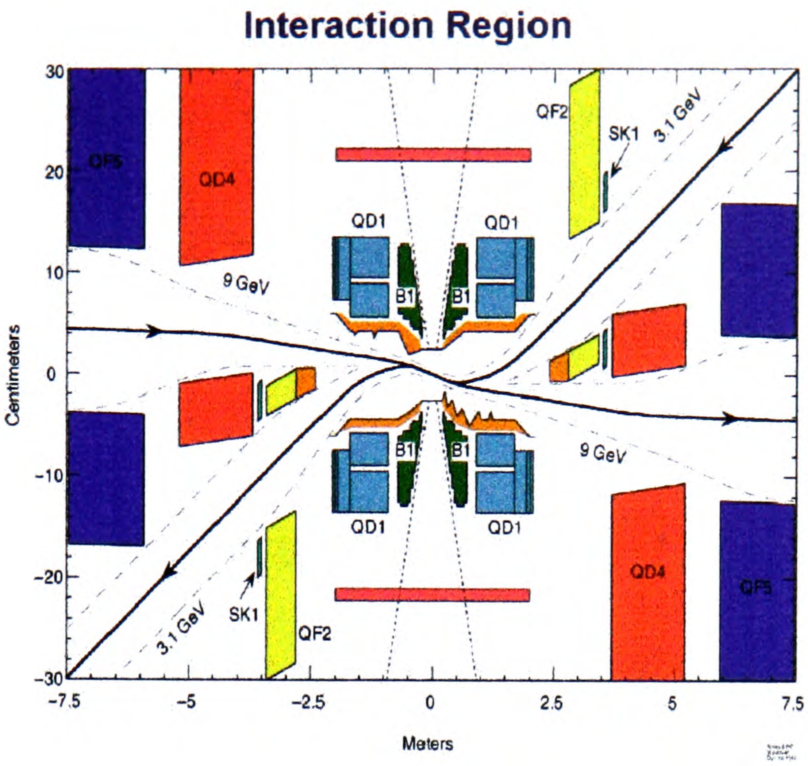

Figure 3.2: Horizontal view of the *BABAR* interaction region.

- The y-axis is vertically perpendicular to the beam axis.
- The x-axis is horizontally perpendicular to the beam axis.

3.4 The *BABAR* detector

The *BABAR* detector was designed to study CP violation in the B_d meson system. In order to meet this objective, several stringent requirements were placed on the detector.

- Excellent reconstruction efficiency and momentum resolution for charged particles over the range 60 MeV to 4.5 GeV
- Efficient identification of different particle types (μ, e, K, π, p) over a wide range of momenta. In particular $\pi - K$ discrimination for high momenta.
- Excellent energy and angular resolution for the detection of neutral particles (π^0, γ) in the range 20 MeV to 4 GeV.

Figure 3.3 shows both the transverse and longitudinal cross-sections of the *BABAR* detector. *BABAR* consists of 5 detectors operating in a large 1.5 Tesla superconducting magnet. A silicon vertex tracker which measures decay vertices and provides initial track information. A drift chamber which provides charged track measurements. A Cherenkov radiation detector which allows different particle types to be identified. An electromagnetic calorimeter for neutral particle detection and an outer detection system composed of an instrumented flux return used to detect muons and identify neutral hadrons (K_L,n).

3.5 The silicon vertex tracker (SVT)

The primary goal of the silicon vertex tracker is to provide precise measurements of the B meson decay vertices necessary for the measurement of time-dependent CP violation. In addition, the silicon vertex detector provides measurements used in the reconstruction of charged particle tracks and also provides initial track angle information. The SVT is the principal detector used to recontruct particle tracks with transverse momenta less than 120 MeV/c.

3.5.1 Design of the SVT

The final design layout of the SVT consists of five concentric layers of double-sided silicon strip sensors. The strips on either side are oriented orthogonally to each other with the outer ϕ strips oriented parallel to the beam and the inner z strips oriented perpendicularly to the beam direction. The inner three layers are responsible for performing measurements of the initial track parameters while all 5 layers are necessary for pattern recognition and low transverse momentum(P_t) tracking. Figure 3.4 shows both longitudinal and cross-sectional views of the SVT.

The arched design of the outer two layers minimises the amount of material in front of the drift chamber. This minimises multiple scattering effects which can degrade the performance of the drift chamber. The maximum SVT acceptance is restricted in polar angle (θ) by the position of the PEP-II beam optics and various mechanical and electronic components. Under these restrictions the final coverage of the SVT extends in polar angle from 20.1^o to 150.2^o.

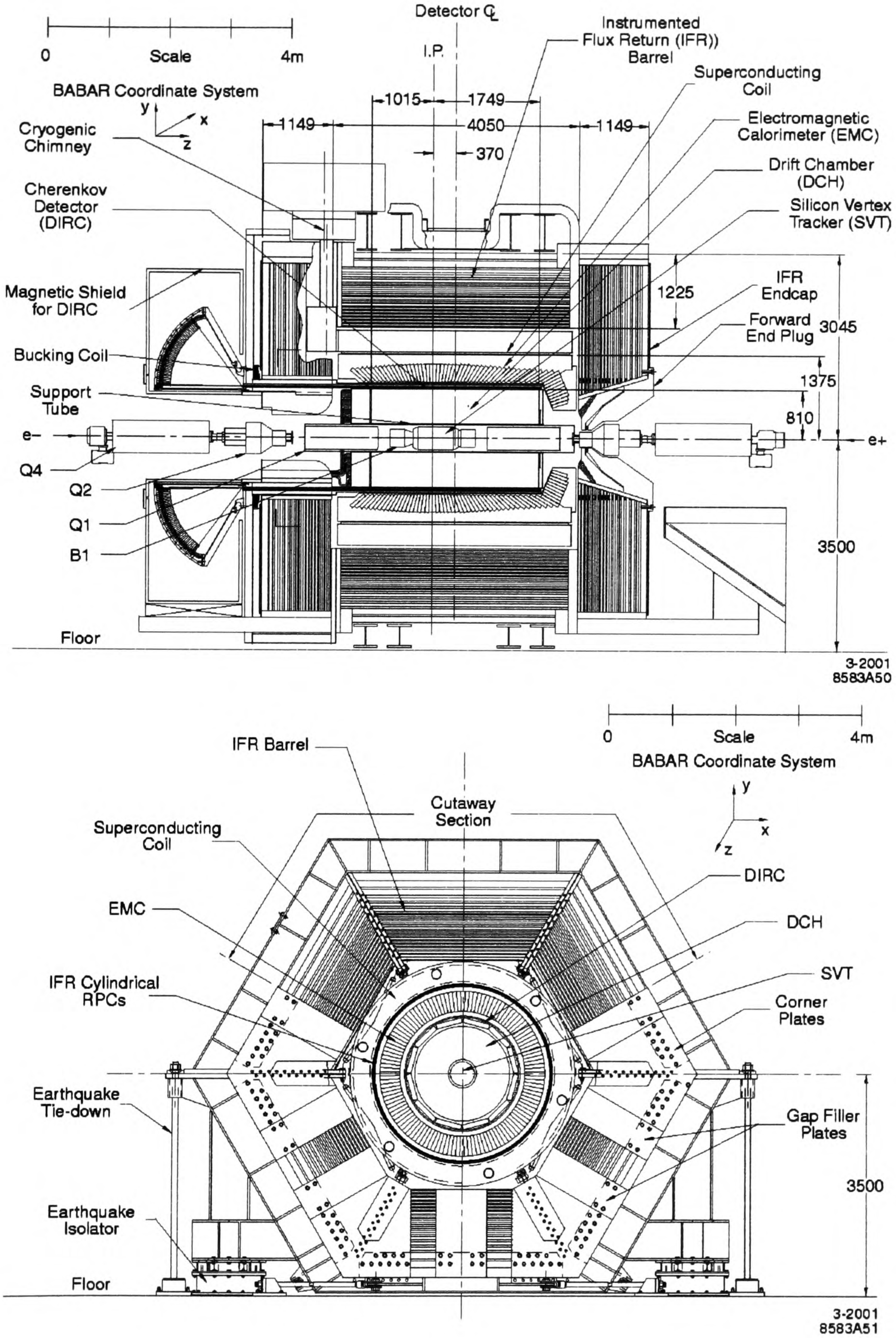

Figure 3.3: [40]Top: longitudinal cross-section of the *BABAR* detector. Bottom: transverse cross-section through the *BABAR* detector. The dimensions are in mm.

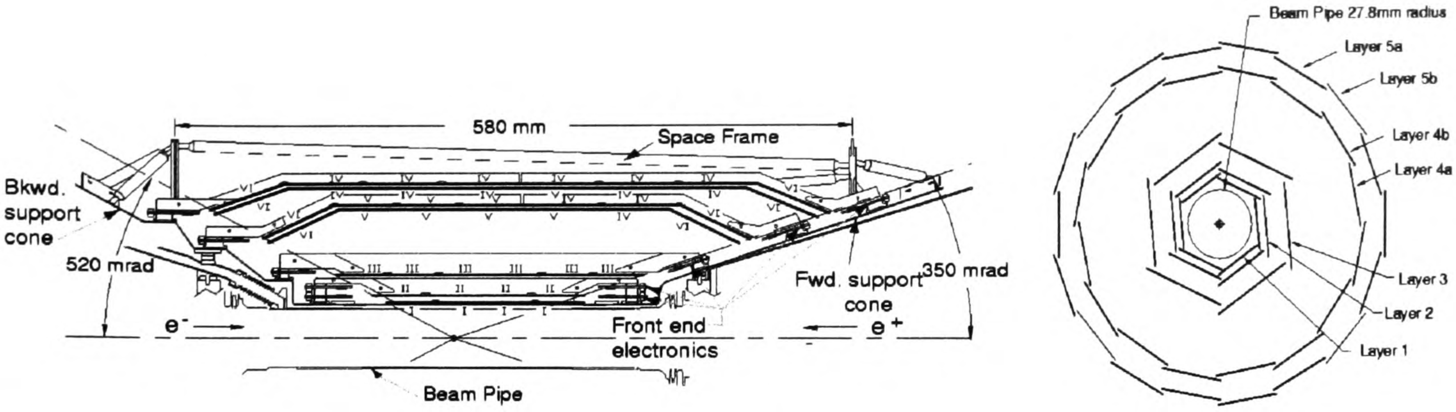

Figure 3.4: Longitudinal view (left figure) and transverse view (right figure) of the SVT showing the 5 layers of silicon and the asymmetric acceptance of the detector [40].

3.5.2 SVT performance

To significantly measure time-dependent *CP* violation the mean vertex resolution along the z-axis of the SVT needs to be a small as possible. Obtaining the best resolution throughout the SVT requires a design which provides the optimal information on the vertex separation while minimising multiple scattering of tracks into the drift chamber. Multiple scattering occurs when particles traverse the beryllium beampipe and the detector silicon. The longitudinal(z) and azimuthal(ϕ) spatial resolutions of the SVT are shown in figure 3.5 where the resolution in both z and ϕ varies between $20-40\,\mu$m.

3.6 The drift chamber (DCH)

The drift chamber is the main tracking detector for the *BABAR* detector. Its primary function is the efficient measurement of charged particle trajectories and the measurement of their momenta. The DCH is also used as one of the primary inputs into the level 1 trigger system.

The DCH complements the measurements of the track impact parameter and directions of the charged tracks provided by the SVT. It also provides the track incident angles into the Cherenkov radiation detector necessary to compute the Cherenkov angle used in particle identification. For low momentum particles $\lesssim 1$ GeV/c for π/p separation and $\lesssim 0.6$ GeV/c for π/K the DCH provides particle identification by measuring ionisation loss ($d\mathrm{E}/dx$) measurements. For the extreme forward and backward directions the DCH $d\mathrm{E}/dx$ measurements are the only way of identifying different charged particle

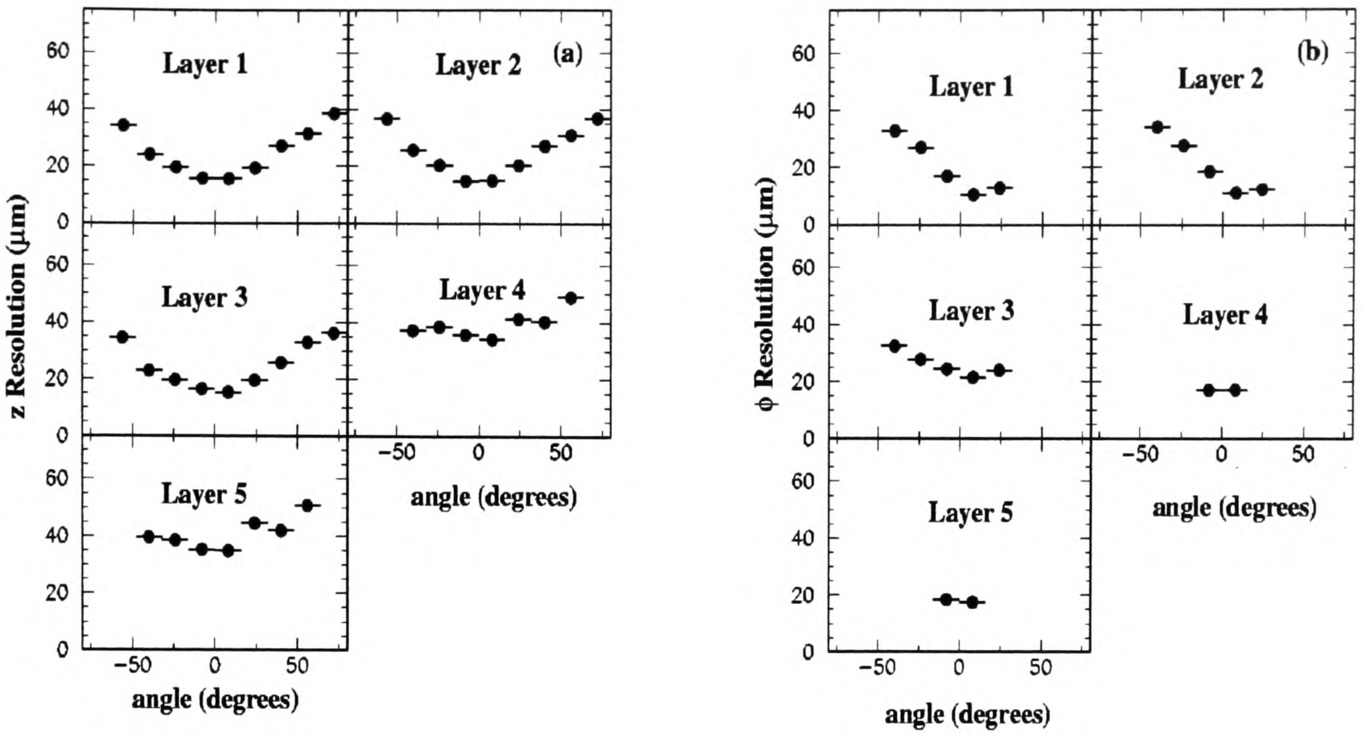

Figure 3.5: Resolution of the silicon vertex tracker in z and ϕ as a function of the track incidence angle for each of the 5 layers [40].

types. The most significant effect limiting the track parameter resolution and hence the performance of the drift chamber comes from multiple scattering. This occurs due to the momentum of B and D charged decay products being on average less than 1 GeV/c. In order to minimise the effects from multiple scattering the amount of material that is placed before the other sub-detectors (SVT, DIRC and EMC) and within the DCH has to be minimised. Further detailed information on the drift chamber can be found in [40].

3.6.1 Drift chamber mechanical design

Figure 3.6 shows the cross-sectional view of the drift chamber. The DCH has an acceptance in polar angle from 17^o to 156^o and is asymmetrically placed with respect to the interaction point (IP). This ensures that half the layers of the DCH are traversed at the limits of acceptance. The DCH design consists of a hollow cylindrical barrel of length 276 cm with an inner radius of 23.6 cm constructed from 1 mm beryllium and outer radius of 80.9 cm constructed from 2 layers [1] of 1.6 mm thick carbon-fibre

---

[1] covered in thin aluminium foil to provide RF shielding

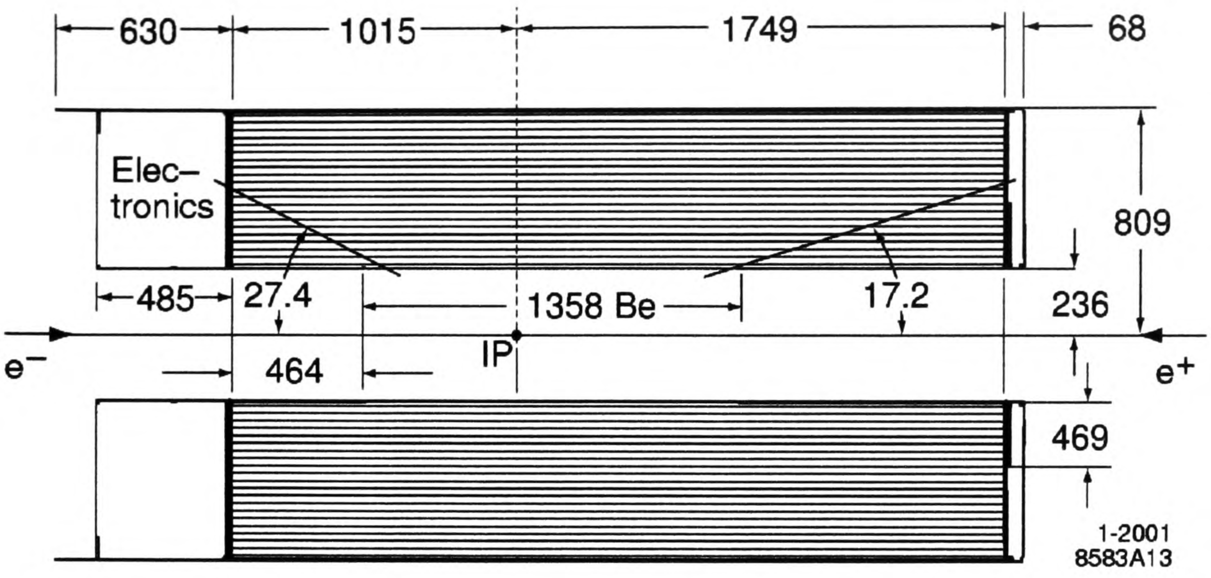

Figure 3.6: Longitudinal cross-section of the drift chamber design. The electronics are located on the back of the detector [40].

laminated to a 6 mm Nomex core. To reduce the impact on track parameter resolution from multiple scatterings the amount of material used for the exterior walls is kept to a minimum. The amount of material visible to a particle as it traverses the detector is measured in radiation lengths denoted X_0. For the DCH exterior walls the total material is equal to $0.28\% X_0$ for the inner wall and $0.54\% X_0$ for the outer wall.

The backward endplate is constructed from 24 mm aluminium while the thickness of the forward endplate is 12 mm. This difference in thickness is necessary to minimise the material before the forward endcap of the electromagnetic calorimeter. The sense wires are $20\,\mu$m gold plated tungsten-rhenium and are operated at 1930V, while the field shaping wires are $120\,\mu$m and $80\,\mu$m gold plated aluminium carrying 340V. Low-mass aluminium field wires and a 80:20 helium:isobutane gas mixture ensure that multiple scattering is held to a minimum ($0.2\% X_0$) while providing reasonable drift times and good dE/dx resolution. The total thickness of the DCH at normal incidence is $1.08\% X_0$. The chamber consists of 7104 hexagonal cells, of approximately 1.7×1.2 cm arranged into 10 super-layers each with 4 layers. This layout provides up to 40 spatial and ionisation loss measurements for tracks with transverse momentum $p_t > 180\,\mathrm{MeV}/c$. The arrangement of axial(A) and stereo(U,V) layers is shown in figure 3.7. Also shown are the ion drift isochrones for a typical cell operating in the

BABAR 1.5 Tesla magnetic field. The stereo angle varies between 40 mrad for the inner layer to 70 mrad for the outer layer and measures longitudinal(z) position with 1 mm resolution. The longitudinal measurements are required for track momentum measurements in the z direction and the reconstruction of decay vertices which originate outside the SVT e.g. K_s^0 decays.

3.6.2 DCH system performance

Figure 3.8 (left plot) shows the DCH $\mathrm{d}E/\mathrm{d}x$ measurements as a function of track momentum for different particle types. The measured resolution of the $\mathrm{d}E/\mathrm{d}x$ measurements is 7.5% determined from Bhabha scattering events.

Charged tracks reconstructed in the SVT and DCH are defined by 5 parameters $(d_0, \phi_0, \omega, z_0, \tan\lambda)$. The parameters d_0, z_0 are the distances of closest approach of the track to the origin, ϕ_0 is the azimuth angle of the track, λ is the dip angle relative to the transverse plane and $w = 1/p_t$ is the track curvature. Track finding and fitting procedures use the Kalman filter algorithm described in [41]. Track parameter resolutions are determined using e^+e^- and $\mu^+\mu^-$ pair events [40] which are given in equation 3.1. The values given correspond to the best possible values obtainable. At lower energies multiple scattering of the tracks will lower the resolution.

$$\begin{aligned} \sigma_{d_0} &= 23\,\mu\mathrm{m} \quad \sigma_{\phi_0} = 0.43\,\mathrm{mrad} \\ \sigma_{z_0} &= 29\,\mu\mathrm{m} \quad \sigma_{\tan\lambda} = 0.53\times10^{-3} \end{aligned} \tag{3.1}$$

The transverse momentum resolution can be parameterised using equation 3.2. Figure 3.8 (right plot) shows the transverse momentum resolution as a function of momentum determined from cosmic muon events.

$$\frac{\sigma(p_t)}{p_t} = (0.13 \pm 0.01)\% \times \frac{p_t}{(1\,\mathrm{GeV/c})} \oplus (0.45 \pm 0.03)\%. \tag{3.2}$$

3.7 The detector of internally reflected Cherenkov radiation (DIRC)

Of central importance to measure the many different hadronic B decay modes is the ability to identify between different particle species of the reconstructed tracks. In order

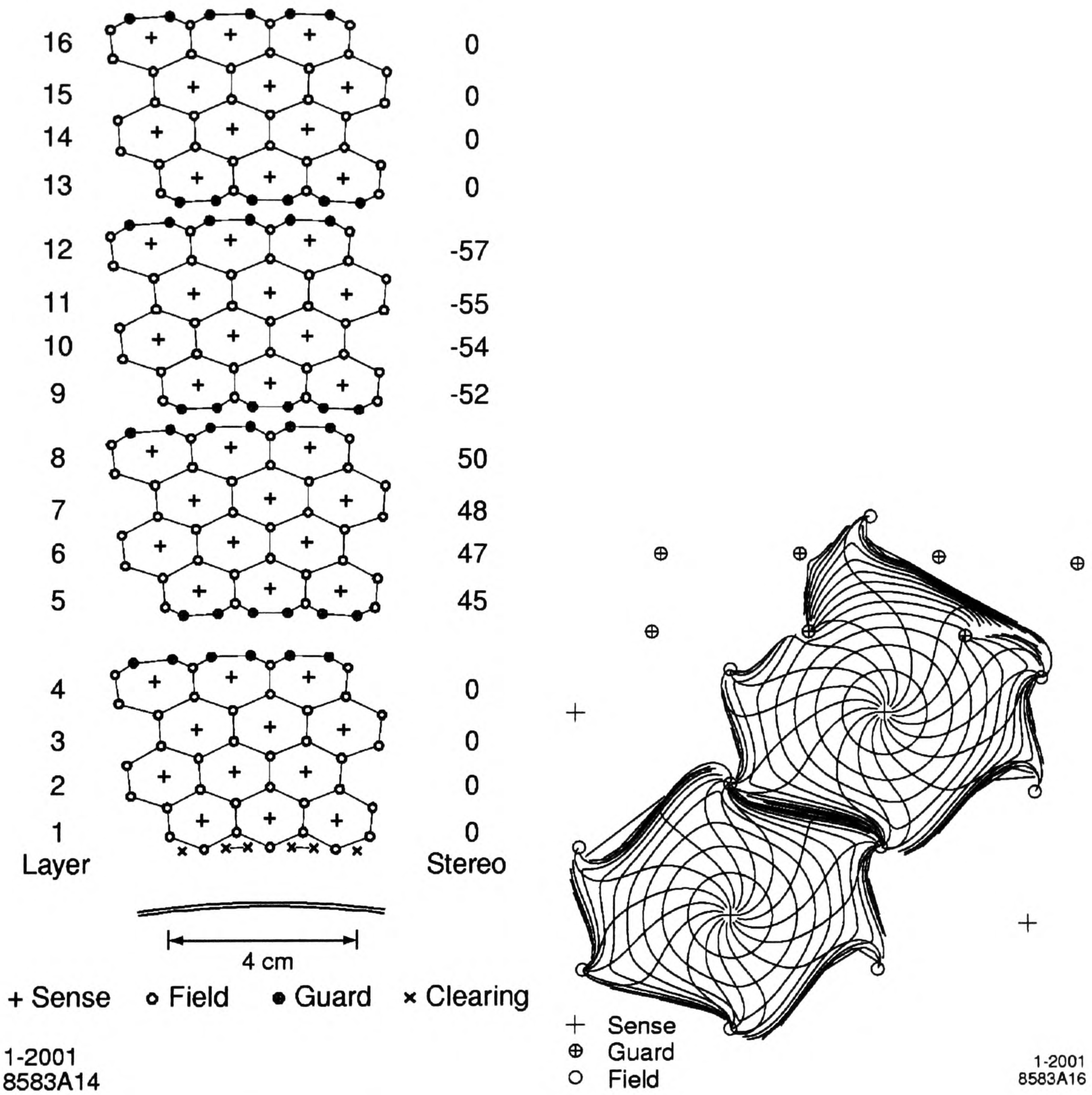

Figure 3.7: Left figure: Schematic layout of drift cells. The numbers on the right side are the stereo angles of the sense wires in mrads. Right figure: Drift cell isochrones (contours of equal drift times). The spacing between isochrones is 100 ns. Also shown are the ion drift trajectories [40].

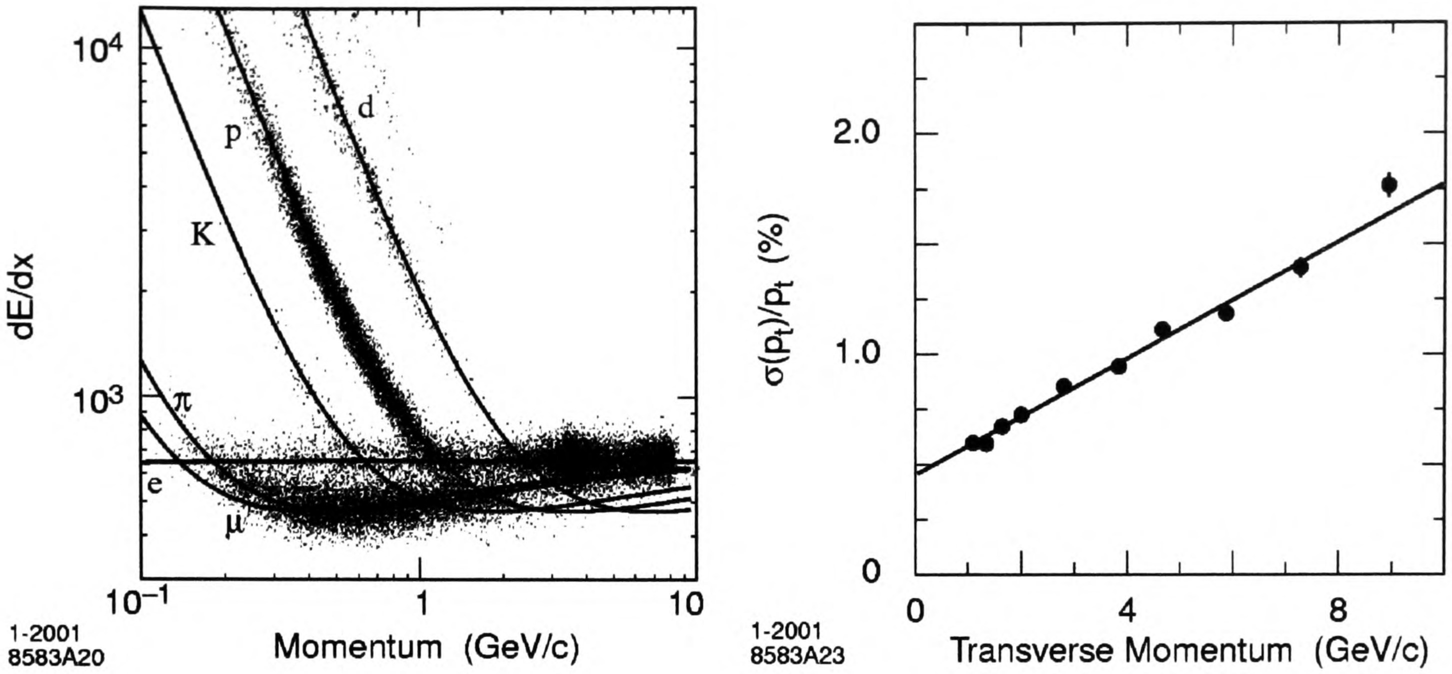

Figure 3.8: Left: $\mathrm{d}E/\mathrm{d}x$ measurements in the DCH as a function of track momentum. Right: transverse momentum resolution as a function of track momentum, determined from cosmic ray muons traversing the DCH and SVT [40].

to distinguish between the final states $B^0 \to \pi^+\pi^-\pi^0$ and $B^0 \to K^+\pi^-\pi^0$ excellent π, K separation is required in the momenta range between 1.7 and 4.2 GeV/c. At the lower end of the momentum spectrum, kaons will need to be correctly identified for tagging purposes. These kaons have momenta that extend up to 2 GeV/c with the majority below 1 GeV/c. The DIRC particle identification system has been designed to provide a $\pi\,K$ separation at the 4σ level or greater within a momentum range between 700 MeV/c and 4.2 GeV/c. For particle identification below 700 MeV/c *BABAR* relies on ionisation loss dE/dx measurements from the SVT and DCH subsystems.

3.7.1 Design of the DIRC

The system chosen in *BABAR* is based on the principle of internal reflection of Cherenkov radiation. When a particle traverses one of the radiator bars with velocity $\beta \geqslant \frac{1}{n}$ Cherenkov radiation is emitted in the form of a cone of light with angle $\cos(\theta_C) = (\beta n)^{-1}$ where n is the refractive index of the radiator's medium. The number of photons emitted for each charged track ranges from 20 to 65 and is a function of the polar angle. The DIRC is composed of 144 radiator bars of rectangular cross-section which

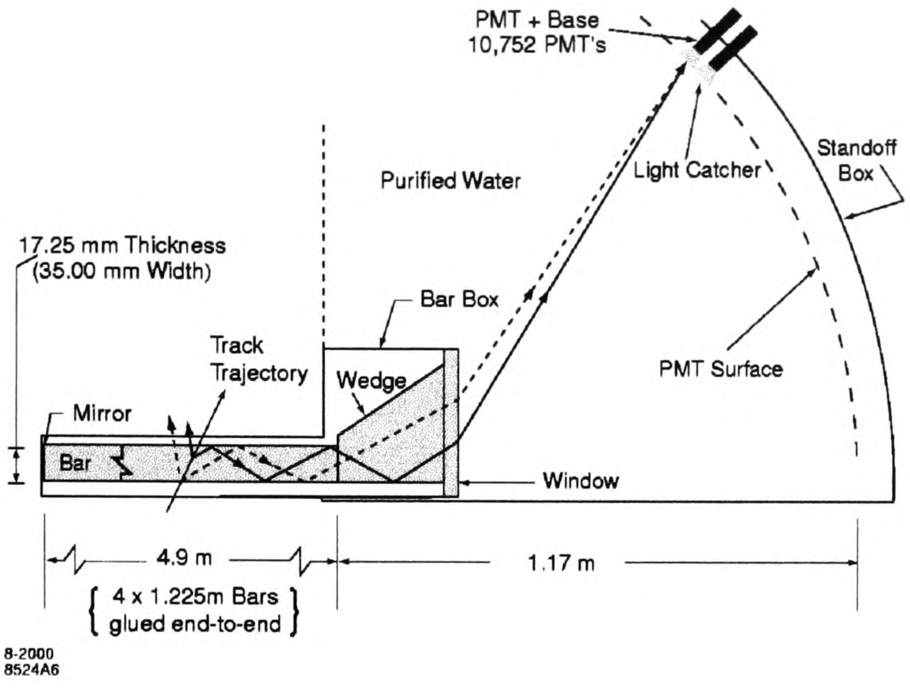

Figure 3.9: Schematic of the DIRC Cherenkov light transport system showing the quartz bars and imaging region [40].

are grouped into 12 boxes arranged around the DCH, covering[2] 94% of the azimuthal angle and providing polar angle coverage between 25.5^o and 147^o .

The radiator material chosen for the DIRC is synthetic fused silica (quartz) which has a high refractive index ($n = 1.473$), a long attenuation length in the UV range($\approx$ 400 nm), a low chromatic dispersion and allows for an excellent optical surface finish ($< 5\AA$). In order to minimise the possibility of photon conversions ($\gamma \rightarrow e^+e^-$) in the DIRC the material placed before the EMC must be minimised. The total DIRC material thickness is $0.20\,X_0$ where $0.15\,X_0$ is from the quartz with a further $0.05\,X_0$ from the aluminium support frame.

A schematic of the DIRC light transport system is show in figure 3.9. The radiated photons are reflected (50-300 reflections) internally in both the forward and backward directions where a typical photon has a propagation time between 10-60 ns. Photons transmitted into the forward direction are reflected by mirrors placed at the end of the quartz bars. The excellent optical properties of the quartz preserve the Cherenkov angle θ_C as the photons are transmitted through the bar into an expansion box filled with $6\,\mathrm{m}^3$ of purified water and allowed to travel for 1.17 m. Water was chosen because

---

[2] The lost acceptance is due to the space between the boxes which is filled with nitrogen

its index of refraction ($n = 1.346$) is close to that of silica thus minimising reflections at the silica/water interface. The resulting Cherenkov ring image is read out by a close-packed array of $10,752$ fast photomultiplier tubes each with a diameter of 2.9 cm.

3.7.2 DIRC performance

The image detected is only a fraction of the original Cherenkov cone. The reconstruction of the Cherenkov angle is performed using a maximum likelihood technique using positional information ($(x, y)_{PMT} \rightarrow (\theta_C, \phi_C)$) and time information ($\Delta t_{\text{arrival}}$). The expected arrival time is calculated from the track time of flight and the photon propagation time for quartz. For each track the likelihood is calculated for each of the different particle types (e, p, π, μ, K).

The difference between the expected and measured arrival time Δt and in particular the choice of the width of the time window provides excellent accelerator and event related background rejection[3].Δt is also useful in reducing the number of quartz reflection ambiguities. These are typically reduced from 16 down to 3. The resolution on Δt is measured to be 1.7 ns which is close to the 1.5 ns resolution of the photomultiplier tubes.

The Cherenkov angle resolution is determined using tracks from di-muon events $e^+e^- \rightarrow \mu^+\mu^-$ with $\sigma(\theta_C) = 2.5\,\text{mrad}$ which is within 10% of the design requirement of 2.2 mrad. The resolution is determined from the relation $\sigma_{\theta_C,\text{track}} = \frac{\sigma_{C,\gamma}}{\sqrt{N_{pe}}}$, where $\sigma_{C,\gamma}$ is the single photon angular resolution which is ≈ 10 mrad and N_{pe} is the number of detected photons. Figure 3.10 shows the Cherenkov angle θ_C as a function of momentum for different particle types.

3.8 The electromagnetic calorimeter (EMC)

The electromagnetic calorimeter provides measurements of the position and energy of electromagnetic showers. It is designed to provide excellent energy and angular resolution over the energy range from 20 MeV up to 12 GeV. The upper bound is required by the need to measure the QED processes $e^+e^- \rightarrow e^+e^-(\gamma)$ and $e^+e^- \rightarrow \gamma\gamma$

---

[3] For ± 300 ns there is $\approx 500 - 1300$ background hits where for ± 8 ns there are $1 - 2$ background hits

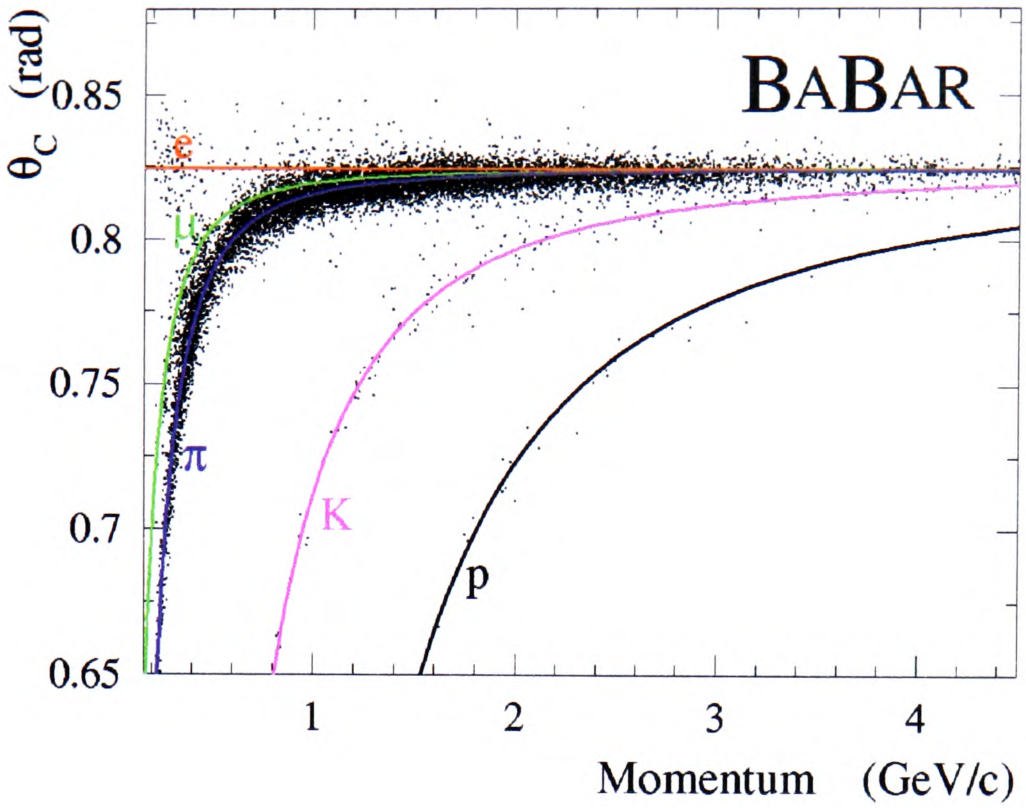

Figure 3.10: The expected Cherenkov angle θ_C as a function of momentum for different particle types. The black dots correspond to data [40].

which are used to calibrate the EMC and also provide luminosity measurements. The large energy range allows for the detection of photons from π^0 and η decays and the reconstruction of B decay channels with photons (radiative penguin modes e.g. $B^0 \rightarrow K^{*0}\gamma$) and π^0 (e.g. $B^0 \rightarrow K^{*0}\pi^0, B^0 \rightarrow K^{*+}\pi^-$) and η particles (e.g. $B^+ \rightarrow K^{*+}\eta$). The EMC is also used in conjunction with the DCH track information to identify electrons.

3.8.1 Design of the EMC

The EMC consists of 6580 caesium iodide CsI(Tl) crystals doped with 1% thallium. These are arranged into a cylindrical barrel of 48 axially symmetric rings each containing 120 crystals and a conical forward endcap with 8 rings each containing 80 to 120 crystals. Figure 3.11 shows a longitudinal view of the EMC.

The calorimeter provides full coverage in the azimuth angle ϕ and extends from 15.8^o to 141.8^o in polar angle θ. The crystals are arranged in a projective geometry in

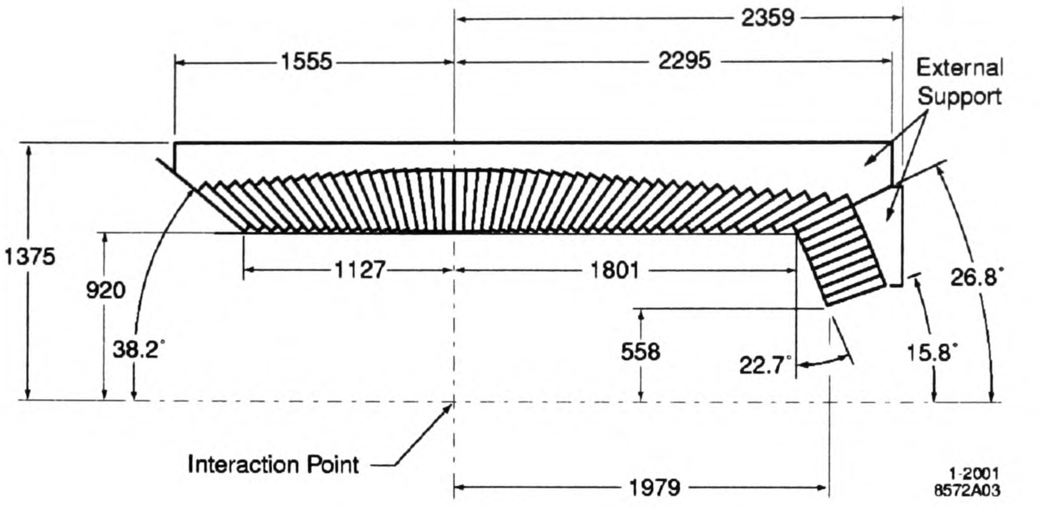

Figure 3.11: Longitudinal view of the electromagnetic calorimeter showing the acceptance and crystal arrangement in the barrel and endcap [40].

θ with the projection angle ranging from 15 mrad in the central barrel to 45 mrad in the endcap. Using a projective layout removes losses in efficiency due to particles striking the dead material between crystals. The total loss of acceptance due to dead material is calculated to be 2.5%. The properties of the CsI(Tl) crystals are described in [40]. The crystals are trapezoidal in cross-section with lengths varying from 29.76 cm (16.1 X_0) to 32.55 cm (17.6 X_0) in the endcap[4]. Each crystal is wrapped in 2 layers of 165 μm tyvek [40] which acts as a reflector of the scintillation light. In addition, a 25 μm layer of aluminium foil provides RF shielding. The scintillation light is readout by two photo-diodes situated on the rear face of the crystals. In principle, the photon detection efficiency of CsI(Tl) is 100% down to a few MeV. However, the minimum expected measurable energy is determined to be 20 MeV which is set by beam and event-related backgrounds.

3.8.2 Reconstruction

A typical electromagnetic shower (cluster) is formed from several adjacent crystals. Pattern recognition algorithms distinguish between single clusters (with one maximum) and composite clusters (with multiple maxima). A cluster is reconstructed from at least one seed crystal with an energy greater than 10 MeV. Other crystals are included if their

---

[4] The extra depth is required due to the effects of the boost on the photon energy spectrum

energy is greater than 1 MeV (3 MeV if they are contiguous neighbours). The energies of secondary maxima are calculated using an iterative algorithm, and their position is determined using a center of gravity method [40]. Charged tracks are associated with the maxima of clusters if the angle and momentum are consistent with the track impact point on the EMC. The correct reconstruction of photons requires a method to distinguish between electromagnetic showers ($e^{\pm}$, γ) and hadronic showers from neutrons and K_L particles interacting in the EMC crystals. Hadronic showers extend over larger number of crystals and have less defined maxima than electromagnetic showers. The main variable used for this purpose is a lateral moment denoted LAT which is defined as [40];

$$\mathrm{LAT} = \frac{\sum_{i=1}^{n} E_i r_i^2}{E_1 R_0^2 + E_2 R_0^2 + \sum_{1=3}^{n} E_i r_i^2} \tag{3.3}$$

where n is the number of crystals in the cluster, E_i is the energy of the i^{th} crystal (The crystals are arranged with decreasing energy, $i = 1$ corresponds to the crystal with maximum energy), r_i is the radial coordinate of the center of i^{th} crystal, R_0 is the average distance between two crystals. The value of the lateral moment variable ranges from 0 to 1.

3.8.3 EMC performance

Energy and angular resolution

The energy resolution of the EMC is determined from a number of different processes which together span the full energy range of the EMC. The results are shown in figure 3.12.

- At low energy the resolution is measured directly using a 6.13 MeV radioactive photon source. This gives a low energy absolute calibration point yielding $\sigma_E/E = 5.0 \pm 0.8\%$ at 6.13 MeV.

- At high energy, the resolution is derived from Bhabha scattering ($e^+e^- \rightarrow e^+e^-$) where the energy of the detected shower can be predicted from the polar angle of the $e^{\pm}$. The measured resolution is $\sigma_E/E = 1.90 \pm 0.07\%$ at 7.5 GeV.

- In the intermediate range of 500 MeV the energy resolution is derived from $\chi_{c1} \rightarrow J/\Psi\gamma$, $(J/\Psi \rightarrow e^+e^-)$ events and for energies up to 2 GeV the decays $\pi^0 \rightarrow \gamma\gamma$ are used.

The energy dependent resolution of the *BABAR* EMC can be parameterised as:

$$\frac{\sigma_E}{E} = \left(\frac{(2.32 \pm 0.30)\%}{\sqrt[4]{E}\,\mathrm{GeV}} \oplus (1.85 \pm 0.12)\%\right) \tag{3.4}$$

The angular resolution is determined from the analysis of the decays $\pi^0 \rightarrow \gamma\gamma$ and $\eta \rightarrow \gamma\gamma$. The resolution varies from 12 mrad at low energies to 3 mrad at high energies and is parameterised as:

$$\sigma_{\phi,\theta} = \left(\frac{3.87 \pm 0.07}{\sqrt{E}\,\mathrm{GeV}} + 0.00 \pm 0.04\right)\,\mathrm{mrad} \tag{3.5}$$

Electrons can be distinguished from charged hadrons using the ratio of the shower energy to track momentum $\frac{E}{p}$. For electrons $\frac{E}{p} \approx 1$ since they deposit most of their energy within the calorimeter.

3.9 *BABAR* magnet system

The *BABAR* magnet system [42] consists of a 1.5 Tesla field parallel to the z direction of the detector. The primary purpose of the magnet is in the measurement of charged particle momenta. The magnitude of the field is set by requirements on charged particle momentum resolution. The supercondutor material is a Rutherford cable composed of filaments of niobium-titanium (NbTi) co-extruded with aluminium with a total length of 10.3 km designed to operate at a current of 4600 A at a temperature of 4.5 K maintained with liquid helium.

3.10 Instrumented flux return (IFR)

The instrumented flux return is the last detector sub-system and is tasked with the detection of muons and neutral hadrons (e.g. K_L^0). The steel flux return of the *BABAR* magnet is used as a muon filter and neutral hadron absorber, a set of interlaced resistive plate chambers (RPC) are used to detect the streamers from the ionising muons.

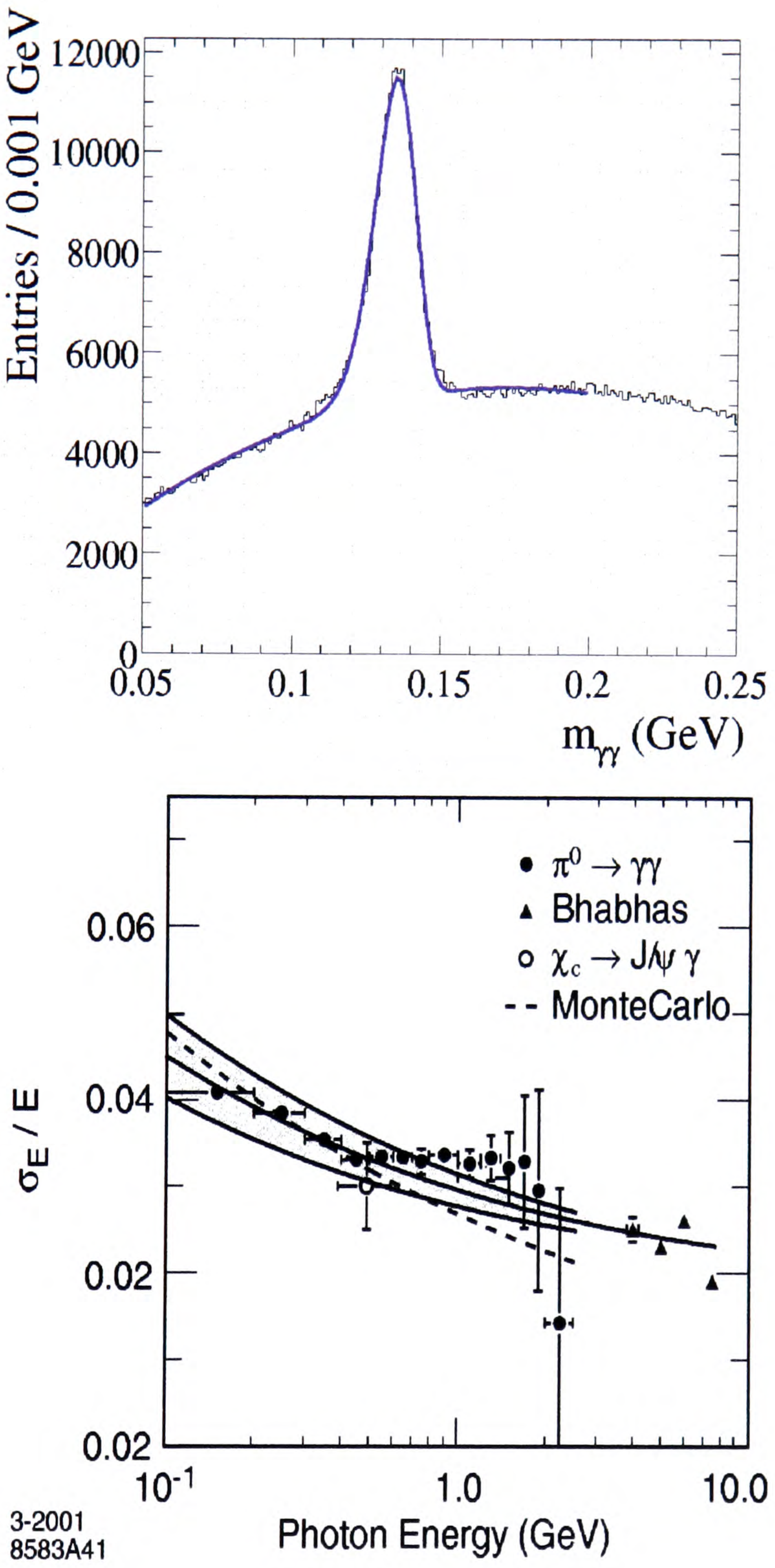

Figure 3.12: Top figure: invariant mass of two photons in $B\bar{B}$ events. The reconstructed π^0 mass is measured to be 135.1 MeV/c^2 and is stable to better the 1% over the full photon energy range. The width is 6.9 MeV/c^2. Bottom figure: the energy resolution for the EMC measured for photons and electrons from different decay modes [40].

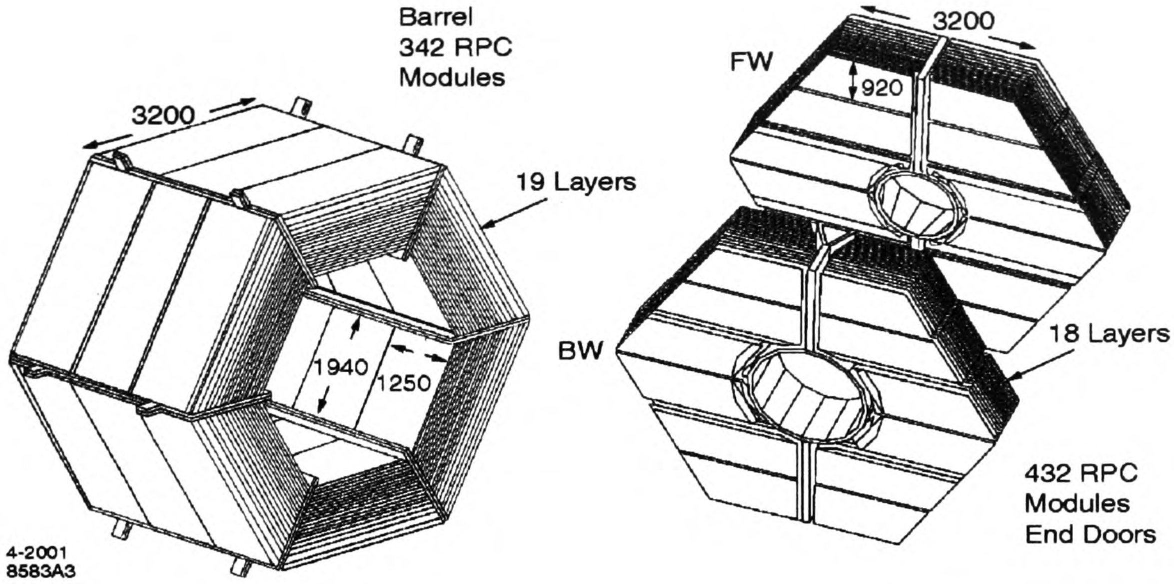

Figure 3.13: Left figure: barrel section of the IFR. Right figure: forward and backward end door sections of the IFR [40].

Figure 3.13 shows the steel flux return of the magnet which consists of a barrel section interlaced with 19 layers of RPCs and two end door sections each interlaced with 18 layers of RPCs.

The steel is segmented into 18 plates, increasing in thickness from 2 cm at the inner layers to 10 cm for the outermost plates. The segmentation was chosen based on Monte Carlo studies of muon penetration and charged and neutral hadron interactions. In addition to the RPCs which are interlaced with the layers of steel, there are two layers of RPCs installed around the EMC which are used to detect particles exiting the EMC (These particles may not have the energy to penetrate the first layer of steel in the IFR).

The RPCs provide readout in both z and ϕ and provide fast response times on the order of 1-2 ns. The position resolution depends on the steel segmentation of the readout though a value of a few mm is achievable. Muons and neutral hadrons are identified with complementary information given by the other sub-systems. Muon identification requires tracking, dE/dx and DIRC θ_C measurements. Neutral hadron identification, particularly K_L^0 identification requires measurements from the EMC as the K_L^0 can shower in the calorimeter allowing matching of the clusters in the EMC to those measured in the IFR.

Chapter 4

Analysis methods & event selections for $B^0 \to K^{*+}\pi^-$, $B^0 \to K^{*0}\pi^0$

In this chapter we describe the aspects of the analyses common to the neutral B decay modes $B^0 \to K^{*+}\pi^-$ and $B^0 \to K^{*0}\pi^0$ into the final state $B^0 \to K^+\pi^-\pi^0$. In section 4.1 we define the data samples and Monte Carlo samples used for the analyses. Section 4.2 and section 4.3 describe the selection of charged tracks and the reconstruction of the neutral π^0. The reconstruction of B^0 mesons is described in section 4.4. In section 4.5 we describe the reconstruction of the $K^*(892)$ meson. Further event selections are discussed in section 4.6 where we discuss the rejection of combinatorial backgrounds. In section 4.7 we introduce the variables used to reject the dominant continuum $q\bar{q}$ background. The maximum likelihood fit method is introduced in section 4.8 which provides an overview of the technique and how it is employed in the analyses.

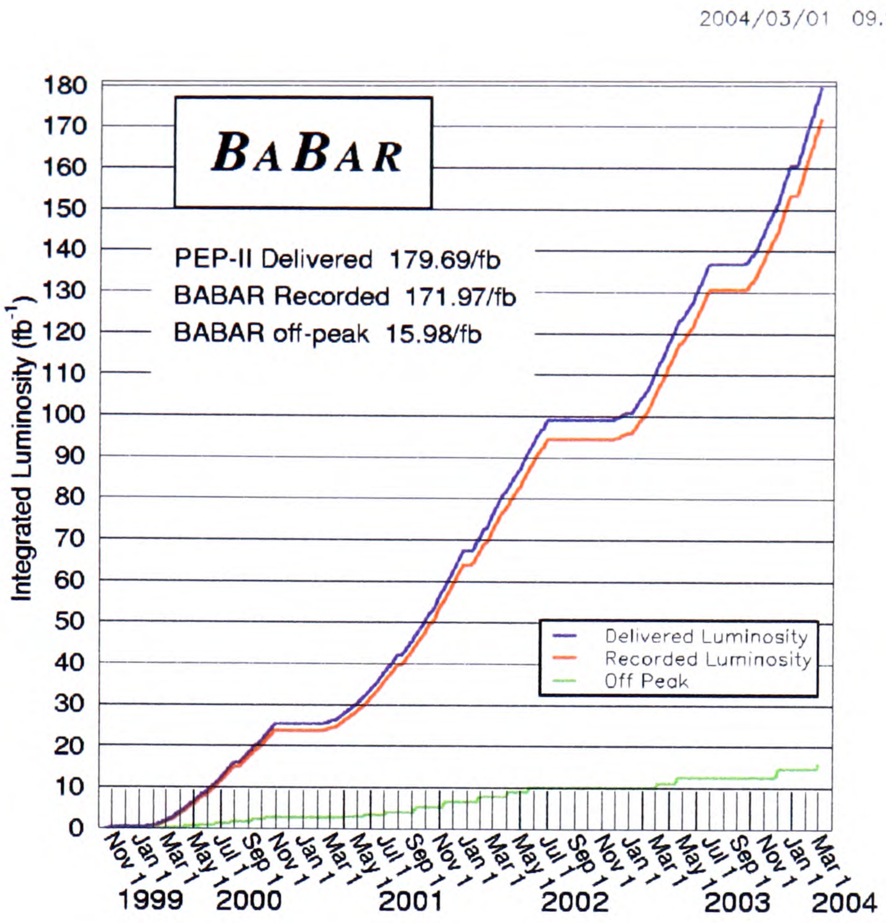

2004/03/01 09.20

Figure 4.1: Integrated luminosity from 22 October 1999 to 1 March 2004.

4.1 Data samples

4.1.1 Data on-peak and off-peak

The data in the analyses presented in this thesis were taken from 22$^{\text{nd}}$ October 1999 to 28$^{\text{nd}}$ October 2000 (Run 1) and from 12$^{\text{th}}$ February 2001 to 30$^{\text{th}}$ June 2002 (Run 2). Run 3 took data between the 8$^{\text{th}}$ December 2002 and 30$^{\text{th}}$ June 2003. We are currently in Run 4 which commenced data taking on 1$^{\text{st}}$ September 2003. The data from Run 3 and Run 4 are not included in the analyses presented here. Figure 4.1 shows the total integrated luminosity from 1999 up to 1st March 2004 where *BABAR* has recorded in excess of 170 fb^{-1}.

90% of the data are recorded at the $\Upsilon(4S)$ and 10% of the data are taken 40 MeV below the $\Upsilon(4S)$ (off-peak data) which provides a sample of continuum events $e^+e^- \to q\bar{q}$, $q = u, d, s, c$ for background studies. In table 4.1 we give the production cross-sections [16] for $e^+e^- \to q\bar{q}$, $q = u, d, s, c, b$ at the center of mass energy 10.58 GeV/c^2.

	cross-section σ(nb) ($\Upsilon(4S)$)
$e^+e^- \to \Upsilon(4S) \to B^0\bar{B}^0 \,\&\, B^+B^-$	1.09
$e^+e^- \to q\bar{q}$	Total = 3.39
$c\bar{c}$	1.30
$s\bar{s}$	0.35
$d\bar{d}$	0.35
$u\bar{u}$	1.39
$e^+e^- \to l^+l^-$	Total = 42.1
$\tau^+\tau^-$	0.94
$\mu^+\mu^-$	1.16
e^+e^-	40

Table 4.1: Production cross-sections [16] for $e^+e^- \to \Upsilon(4S) \to B^0\bar{B}^0 \,\&\, B^+B^-$, $e^+e^- \to q\bar{q}$, l^+l^- at the $\Upsilon(4S)$ center of mass energy 10.58 GeV/c^2.

We also give the $e^+e^- \to l^+l^-$, $l = \nu, e, \mu$ cross-sections[1].

4.1.2 Monte Carlo simulations

Monte Carlo simulations are required for the determination of selection efficiencies, modeling of fit variables and analysis validation. Monte Carlo simulation in *BABAR* uses the JETSET [43] and EvtGen [44] programs. The EvtGen generator is used for the decay of B mesons to exclusive final states, while the JetSet generator is used for inclusive B decays and continuum events. The full *BABAR* detector simulation is performed using the GEANT simulation program [45].

The analyses presented here use the following data samples and simulated Monte Carlo:

- Generic $B^0\bar{B}^0$: 74,065,700 events corresponding to 68.6 fb^{-1}.
- Generic B^+B^-: 77,700,000 events corresponding to 71.9 fb^{-1}.

---

[1] The e^+e^- cross-section is limited due to the acceptance of the detector.

- Charmless cocktail: 10,472,000 events.
- $e^+e^- \to q\bar{q}$: u, d, s: 219,243,000 events, $c\bar{c}$: 135,515,900 events.
- $B^0 \to K^{*+}\pi^-$, $K^{*+} \to K^+\pi^0$: 51,000 events.
- $B^0 \to K^{*0}\pi^0$, $K^{*0} \to K^+\pi^-$: 110,000 events.
- On-peak data: 81.878 fb^{-1}: corresponding to 88,837 million $B\bar{B}$ events.
- Off-peak data: 9.578 fb^{-1}:

4.2 Selection of the charged π and K mesons

Tracks are reconstructed from raw digital hits recorded in the silicon vertex tracker (SVT) and drift chamber (DCH) sub-detectors as discussed in chapter 3. Track finding and fitting uses pattern recognition algorithms and Kalman filter techniques [41] discussed earlier in section 3.6.2. These reconstruction algorithms are not perfect and backgrounds arise in the form of random combinatorial tracks. These background combinatorial tracks are formed by combining hits due to different tracks. There are also tracks which do not originate from the interaction point (IP) *e.g.* beam background particles traversing the detector. These particles also leave hits in the detector which subsequently increases the level of the combinatoric background. To reduce track backgrounds the following selection criteria is applied to the reconstructed tracks. These criteria provide a sufficient quality of track for the analyses presented here.

- Minimum transverse track momentum in lab frame of 100 MeV/c^2,
- Maximum track momentum in center of mass system frame of 10 GeV/c,
- Minimum number of 12 hits in the DCH sub-detector,[3]
- Maximum distance of closest approach (DOCA) to the IP of 10 cm along the $\pm z$ axis,

---

[2] Tracks with $p_t < 100$ MeV/c are only reconstructed in the SVT

[3] This requirement implicitly imposes a restriction on the acceptance region.

- Maximum DOCA to the IP of 1.5 cm perpendicular to the z axis.

Figure 4.2 shows a comparison of data and simulated Monte Carlo for tracks satisfying the above criteria.

Different particle types are selected using a maximum likelihood technique described in detail in section 4.8. A likelihood function is constructed for each possible particle hypothesis e, μ, p, K, π, using information from the SVT, DCH and Cherenkov radiation (DIRC) detectors. The SVT and DCH detectors measure the loss of energy due to ionisation ($\mathrm{d}E/\mathrm{d}x$) and the DIRC contributes two components to the likelihood function for each particle hypothesis. The first is the Cherenkov angle θ_C and second is the probability of observing the detected number of photons $P(N_\gamma)$. The kaon and pion selection for the analysis of the final state $B^0 \to K^+\pi^-\pi^0$ uses the SVT and DCH information for momenta up to 0.7 GeV/c and DIRC information for momenta greater than 0.6 GeV/c. The kaon selection efficiency is shown in figure 4.3 as a function of track momentum. In section 5.9.4 we make a correction for the differences between the Monte Carlo and data.

4.3 Selection of the π^0

The neutral pion π^0 decays almost exclusively to two photons with $\mathcal{BR}(\pi^0 \to \gamma\gamma) = 98.798\%$. It has a mass of of 134.97 MeV/c^2 where both values are obtained from the 2002 Particle Data Book (PDG) [15]. We reconstruct π^0 candidates by forming pairwise combinations of photons identified by the *BABAR* electromagnetic calorimeter (EMC). To reduce any combinatoric backgrounds and remove very low energy photons from PEP-II backgrounds each reconstructed π^0 candidate must satisfy the following criteria:

- Minimum photon energy E_γ of 30 MeV for both photons,
- $0.1 < LAT < 0.8$,
- $110\,\mathrm{MeV/c^2} < M_{\gamma\gamma} < 160\,\mathrm{MeV/c^2}$.
- Minimum π^0 energy E_{π^0} of 200 MeV,

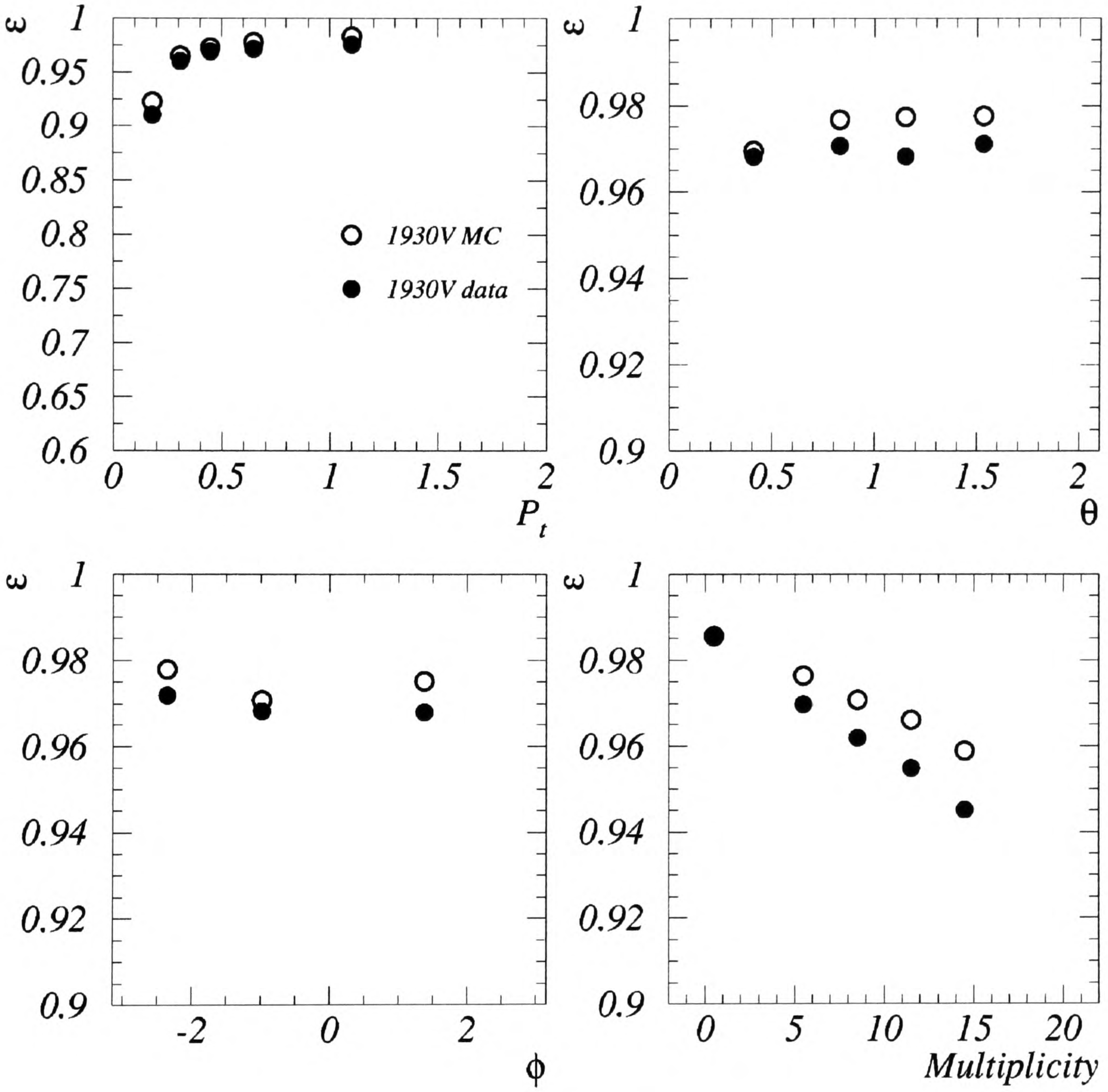

Figure 4.2: Comparison of efficiencies ω for data (drift chamber high voltage 1930V) and Monte Carlo track parameters taken from [46]. The track parameters are; the track transverse momentum, polar and azimuthal track angles θ, ϕ and the multiplicity of tracks per event.

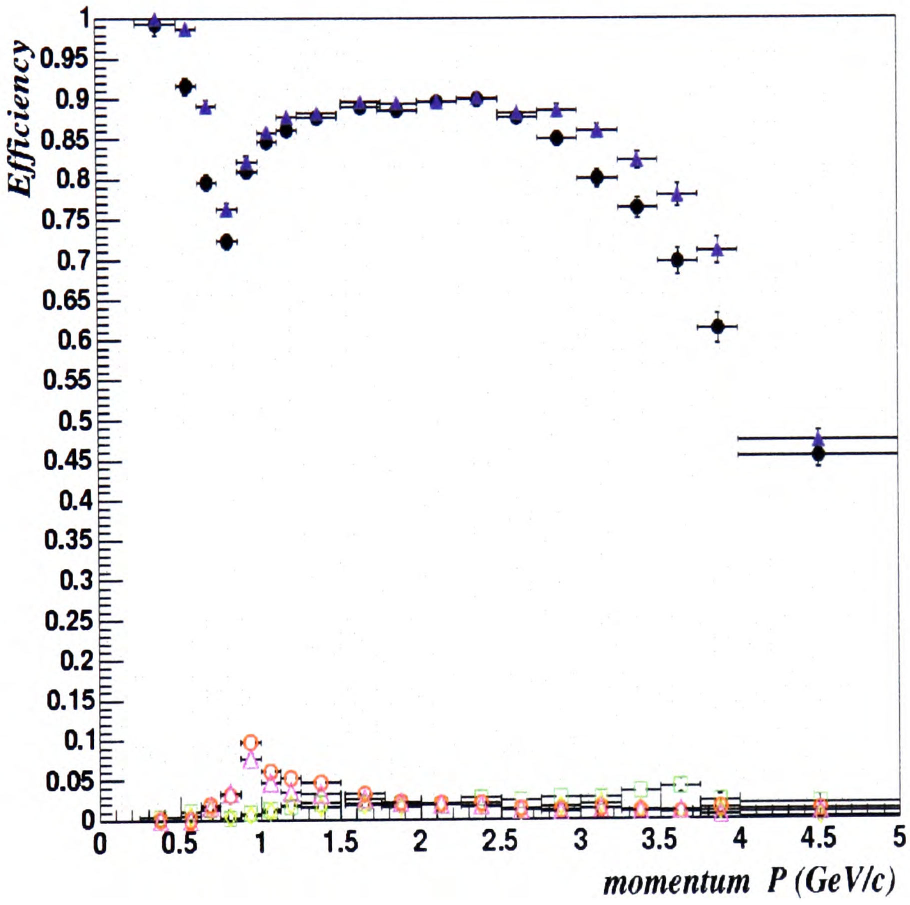

Figure 4.3: Efficiencies comparisons for the kaon identification selector. Black full circles are $D^{*+} \to D^0\pi^+$, $D^0 \to K^-\pi^+$ control sample data. Blue full triangles are Monte Carlo D^{*+} control sample. Red open circles are mis-identified protons from $\Lambda \to p\pi$ decays in data. Purple open triangles are mis-identified protons from Monte Carlo $\Lambda \to p\pi$ decays. The yellow open diamonds are misidentified charged pions from the D^{*+} control sample data and the open green squares are mis-identified pions from the Monte Carlo D^{*+} sample.

where LAT is the lateral shower moment defined in section 3.8.2. Figure 4.4 shows the distribution of the invariant mass of the two photons for all reconstructed π^0 candidates satisfying the initial π^0 selection in both $B^0 \to K^{*0}\pi^0$ and $B^0 \to K^{*+}\pi^-$ signal Monte Carlo. The variation in the π^0 widths is due to the difference in energies of the π^0 for each analysis[4].

The abundance of combinatoric π^0 candidates in the $B^0 \to K^{*+}\pi^-$ mode is due to the lower energy spectrum of its π^0. At lower energies, a larger number of photons are available to form random π^0 candidates. Figure 4.5 shows the lab-frame momentum of the reconstructed π^0 candidates for both $B^0 \to K^{*+}\pi^-$ and $B^0 \to K^{*0}\pi^0$ Monte Carlo.

4.4 Neutral B meson reconstruction

The reconstruction of the B candidate with final state $h^+h^-h^0$ consists of two charged tracks ($h^\pm$) and a neutral candidate (h^0) satisfying the selections described in sections 4.2 and 4.3. In reconstructing the B it is necessary to introduce the following important variables ΔE and m_{ES}.

- The variable ΔE is defined by:

  $$\Delta E = E_B^* - \sqrt{s}/2 . \tag{4.1}$$

  where E_B^* is the energy of the reconstructed B candidate in the center of mass frame and s is the center of mass energy of the $e^+ e^-$ system.

  For modes which contain neutral particles (π^0, γ) the resolution on ΔE is typically $20 - 30\,\mathrm{MeV}$ whereas for modes with only charged particles the ΔE resolution is $10 - 15\,\mathrm{MeV}$. This difference is attributable to the energy resolution for photons in the electromagnetic calorimeter.

- The beam energy substituted mass m_{ES} is defined by:

---

[4] Higher energy neutral pions have a larger width. The mass of the π^0 also varies as a function of energy [47]

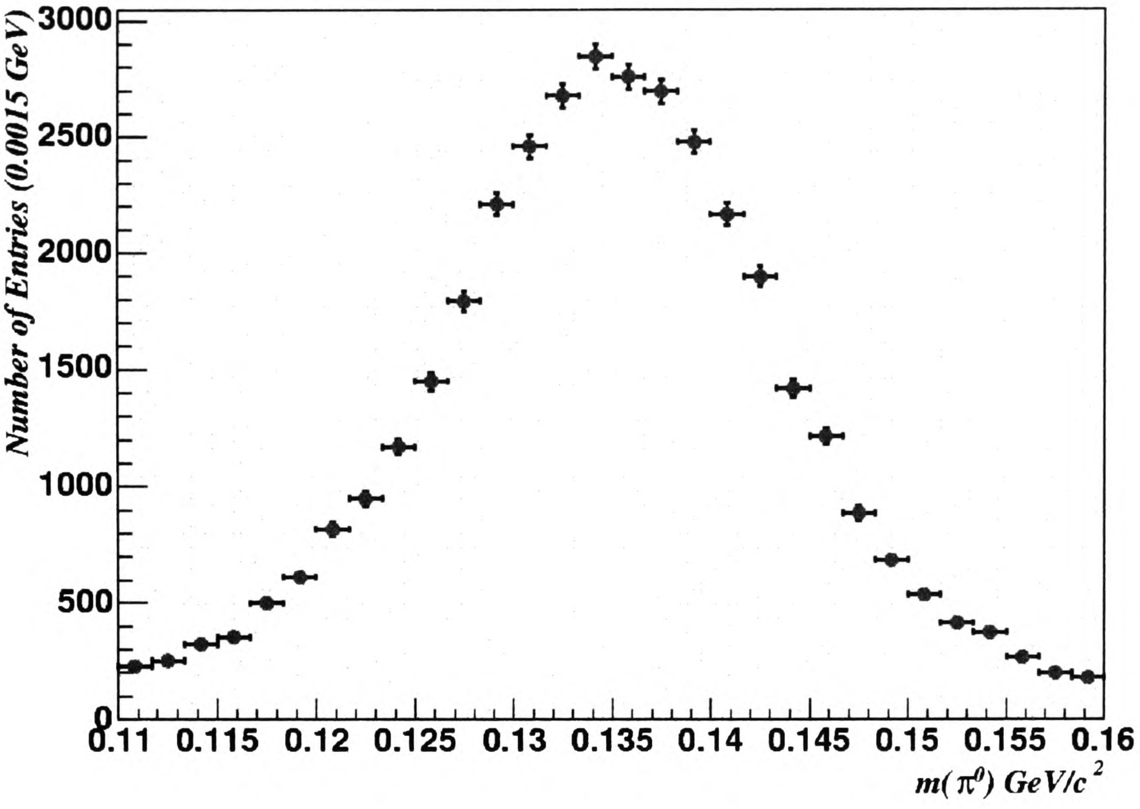

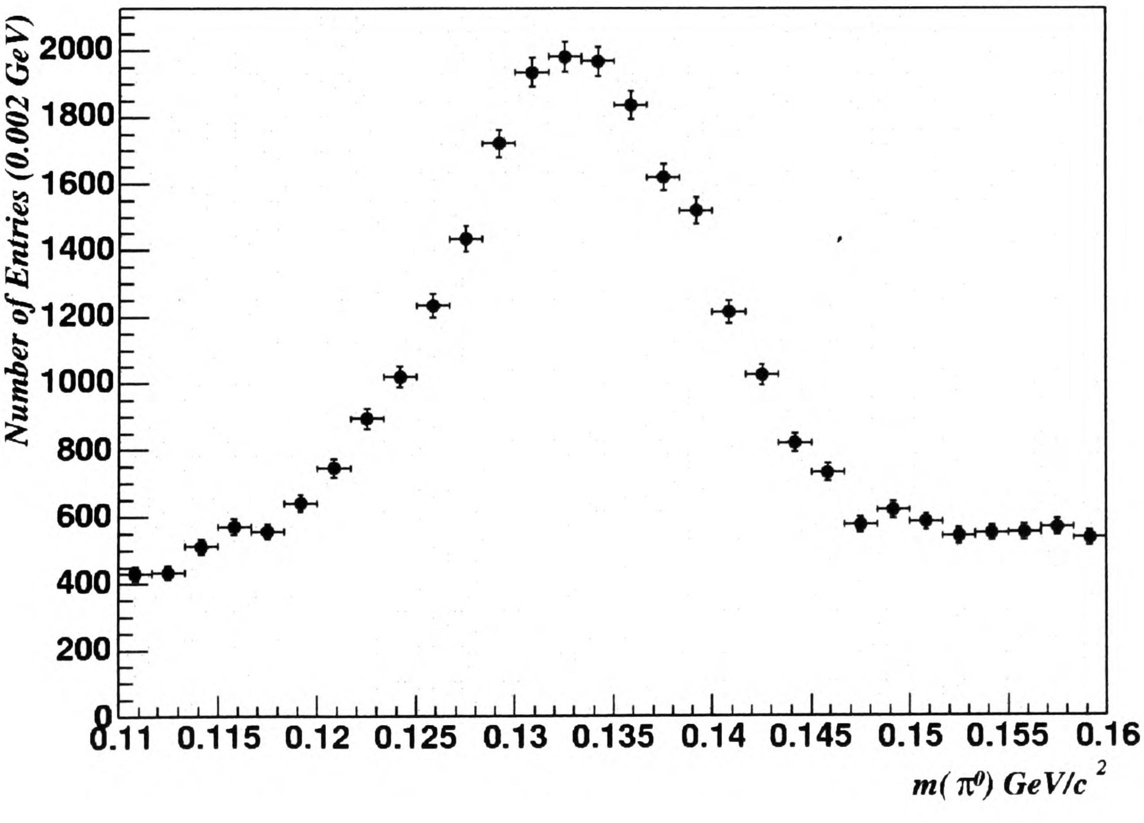

Figure 4.4: Invariant mass of the two photons for all π^0 candidates satisfying the initial criteria in section 4.3 Top figure: Monte Carlo $B^0 \to K^{*0}\pi^0$. Bottom figure: Monte Carlo $B^0 \to K^{*+}\pi^-$.

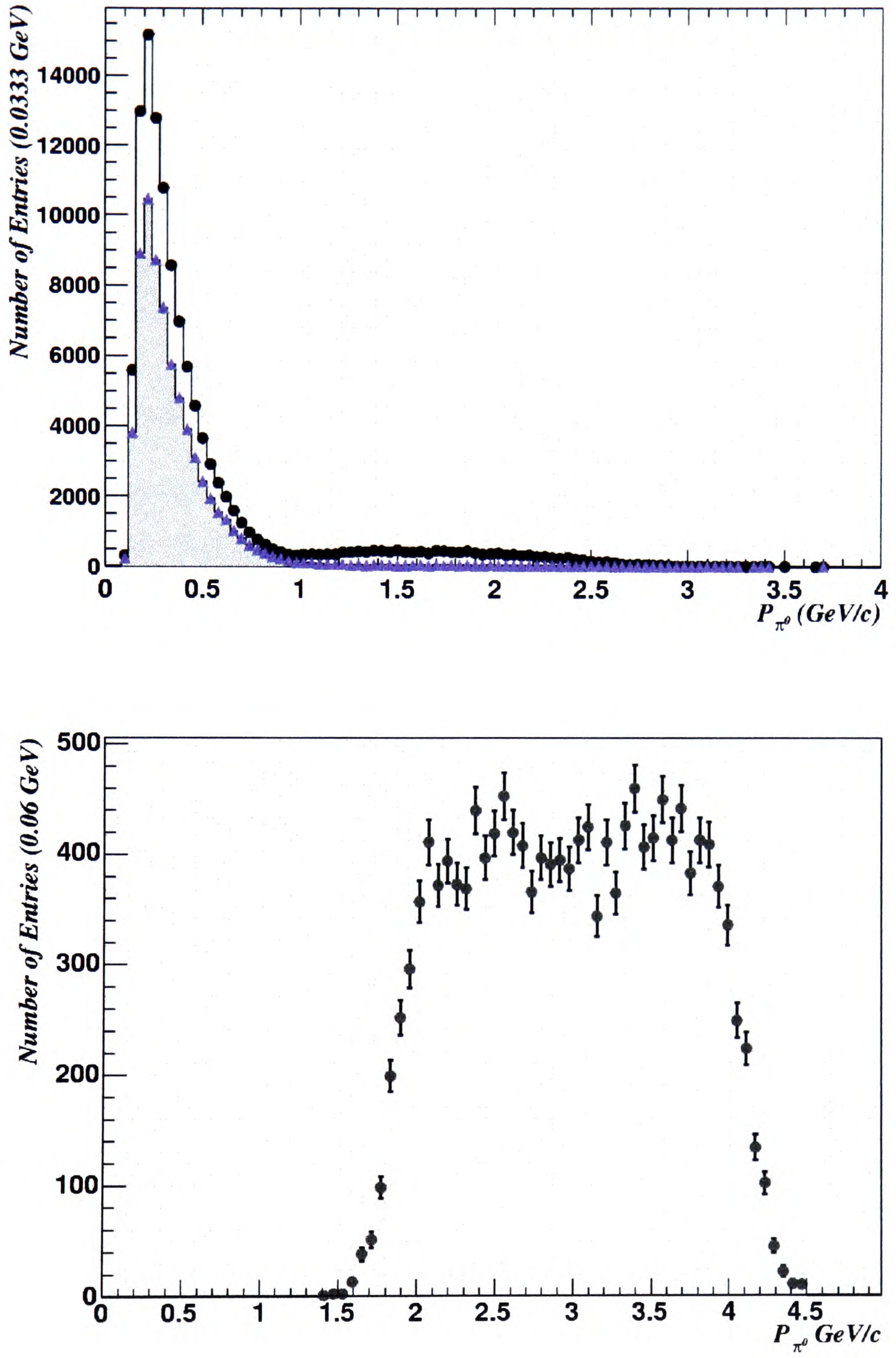

Figure 4.5: Lab-frame momentum spectrum of reconstructed π^0 candidates (black circles) in $B^0 \to K^{*+}\pi^-$ Monte Carlo. The blue triangles are combinatoric random π^0 candidates. Momentum spectrum of reconstructed π^0 candidates (black circles) in $B^0 \to K^{*0}\pi^0$ Monte Carlo.

$$m_{ES} = \sqrt{(s/2 + p_i.p_B)^2/E_i^2 - p_B^2}, \tag{4.2}$$

where E_i and p_i are respectively the energy and momentum vector of the e^+e^- pair in the lab frame, and p_B is the momentum vector of the reconstructed B candidate also evaluated in the lab frame. For signal, m_{ES} is centered at the mass of the B meson ($m_B = 5.279\,\mathrm{GeV/c^2}$) with a resolution of $2.8\mathrm{MeV/c^2}$ dominated by beam energy fluctuations.

4.4.1 Preselection of events

Due to the large size of the *BABAR* data set it is useful to run a loose analysis on the entire data set to subselect events with similar characteristics to the mode under study. The ***pre-selection*** criteria used to subselect these events is given the name *BCCPi03body* where we require:

- Each event contains > 3 tracks satisfying the selections of section 4.2.
- π^0 candidate satisfying the selections of section 4.3.
- $|\Delta E| < 0.45\,\mathrm{GeV}$ and $|m_{ES} - m_B| < 0.1\,\mathrm{GeV}/c^2$.
- Correct charge $\sum_{i=1}^{2} Q_i = 0$.

The result is a more manageable data set on which to perform a more detailed analysis. The pre-selection efficiency for the *BCCPi03body* criteria is found to be $\approx$ 2.1% for data. For Monte Carlo, the pre-selection efficiencies are taken relative to the number of generated events.

4.4.2 Further m_{ES} & ΔE selections

For the analyses presented here we choose a final m_{ES} selection region of $5.20 < m_{ES} < 5.29\,\mathrm{GeV/c^2}$. The final ΔE selection region is defined to be $|\Delta E| < 150\,\mathrm{MeV}$ which reduces backgrounds from other B decays *e.g.* four-body decays, where three of the four tracks from the B decay are reconstructed as a signal candidate. These backgrounds typically have a value of ΔE which is shifted by at least the mass of the missing particle.

Figure 4.6 and figure 4.7 show the distributions of ΔE versus m_{ES} for Monte Carlo $B^0 \to K^{*+}\pi^-$, $B^0 \to K^{*0}\pi^0$ and $q\bar{q}$ continuum background.

4.5 Reconstruction of the $K^*(892)$ meson

The $K^{*+}(892)$ vector resonance has a mass of 891.66 MeV/c^2 and a width of 50.8 MeV/c^2 from the PDG [15]. It decays $\approx$ 100% via $K^{*+} \to K^+\pi^0$ or $K^{*+} \to K^0\pi^+$ with relative probabilities 1/3 and 2/3 respectively[5]. In considering the final state $K^+\pi^-\pi^0$, only the $K^{*+} \to K^+\pi^0$ channel is reconstructed using kaons and neutral pions selected as previously described.

The $K^{*0}(892)$ vector resonance has a mass of 896.10 MeV/c^2 and a width of 50.4 MeV/c^2 [15]. The possible decay modes are $K^{*0} \to K^+\pi^-$ or $K^{*0} \to K^0\pi^0$ with relative probabilities 2/3 and 1/3 respectively. In considering the final state $K^+\pi^-\pi^0$, only the $K^{*0} \to K^+\pi^-$ channel is reconstructed.

As the K^* is a vector particle $J = 1$, whereas both the kaon and the pion are pseudo-scalar particles $J = 0$, conservation of total angular momentum requires that the kaon and pion system be created in a P-wave, L=1, orbital angular momentum state. The effects of the relative angular momentum can be seen by considering the distribution of the helicity angle. We denote the helicity angle by $\theta_H^{K^*}$, defined as the angle between the K^* daughter pion flight direction in the K^* rest frame and the flight direction of the K^* in the lab-frame. For the K^* resonance, the angle $\theta_H^{K^*}$ follows a $\cos^2(\theta_H^{K^*})$ distribution. Shown in figure 4.8 are the lab-frame momentum distributions of the K^{*+} daughters for $B^0 \to K^{*+}\pi^-$ against $\cos(\theta_H^{K^{*+}})$. We see that if the π^0 has low (high) momentum then the corresponding kaon momentum will be high (low).

Figure 4.9 shows the reconstructed invariant mass of K^* candidates against $\cos(\theta_H^{K^*})$ for both $B^0 \to K^{*+}\pi^-$ and $B^0 \to K^{*0}\pi^0$ signal Monte Carlo. A selection region of $0.80 \le m(K^*) \le 1.0$ GeV/c^2 is chosen to select K^* meson candidates and reduce the number of mis-reconstructed K^* candidates.

---

[5] These are determined from isospin considerations and the corresponding Clebsch-Gordan coefficients.

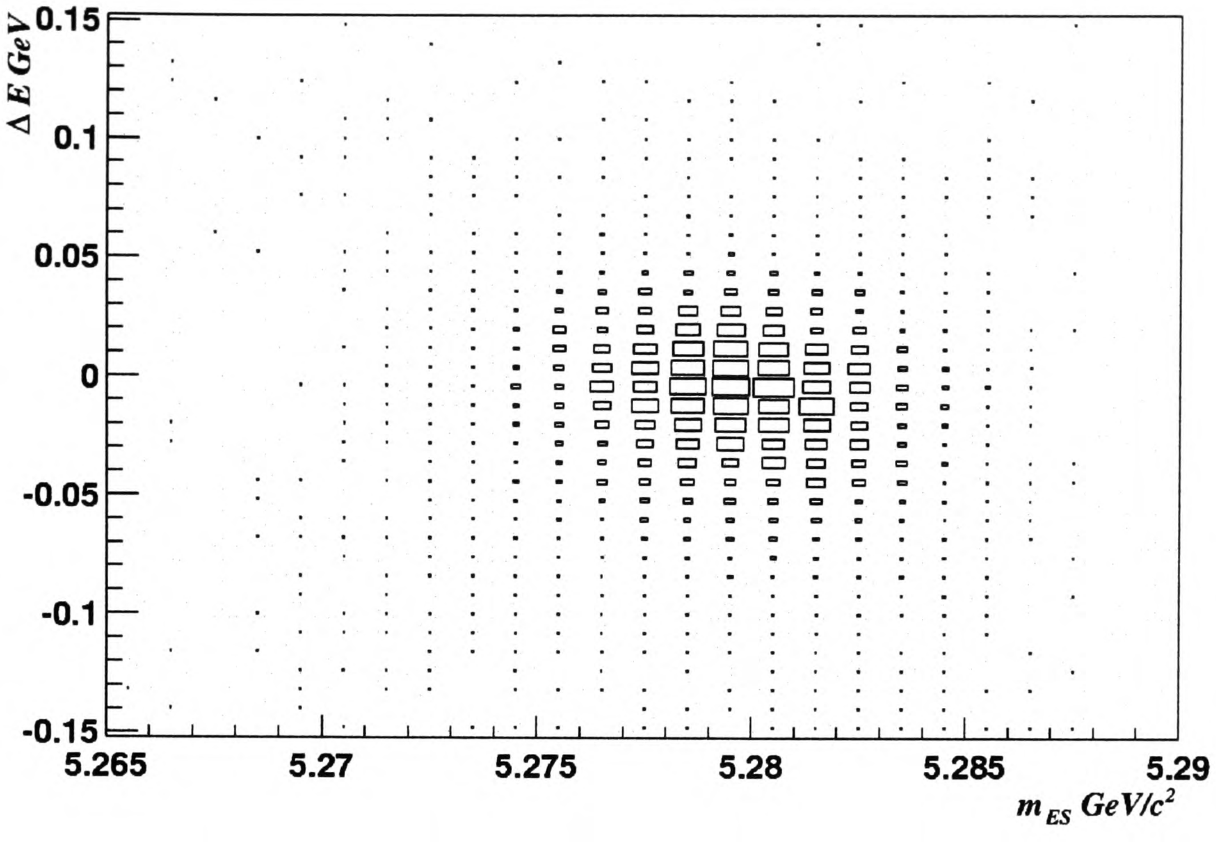

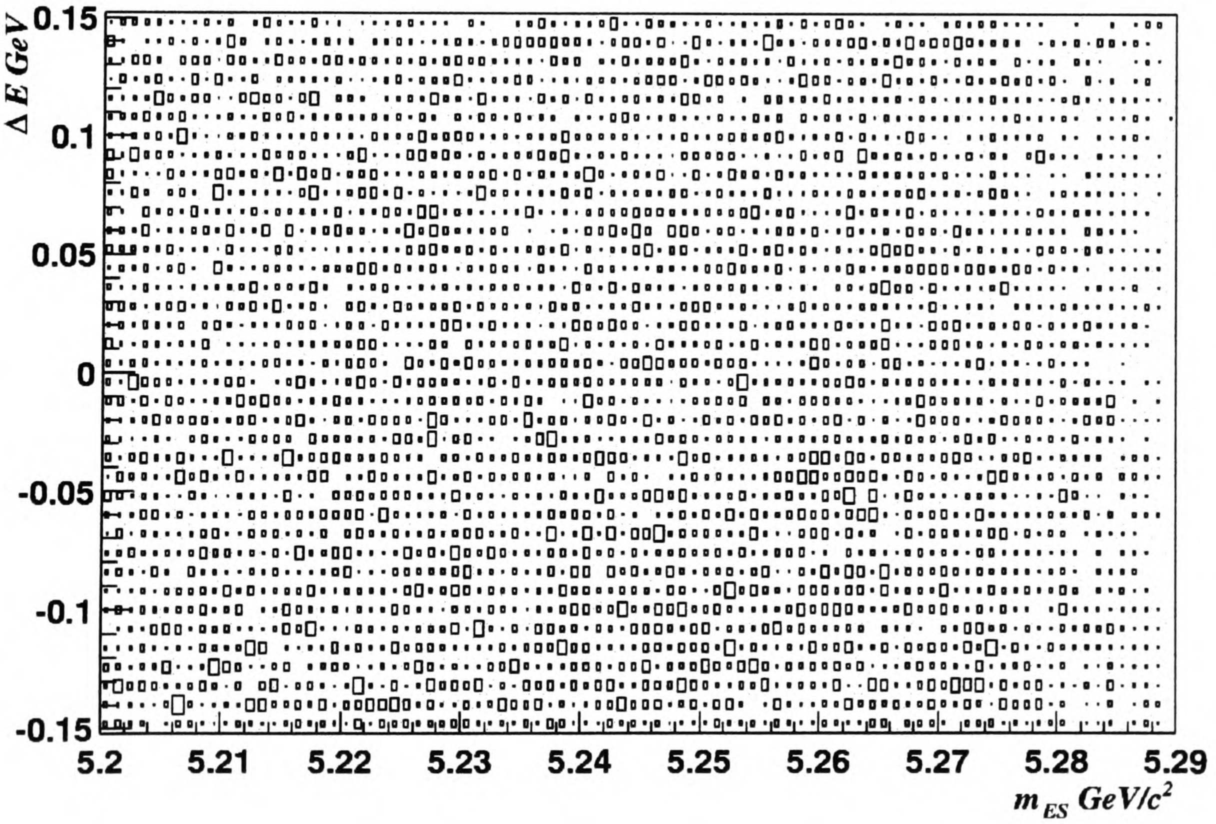

Figure 4.6: Top figure: Reconstructed signal $B^0 \to K^{*+}\pi^-$ Monte Carlo in m_{ES} versus ΔE. Bottom figure: m_{ES} versus ΔE for Monte Carlo continuum $q\bar{q}$, $q = u, d, s, c$ background.

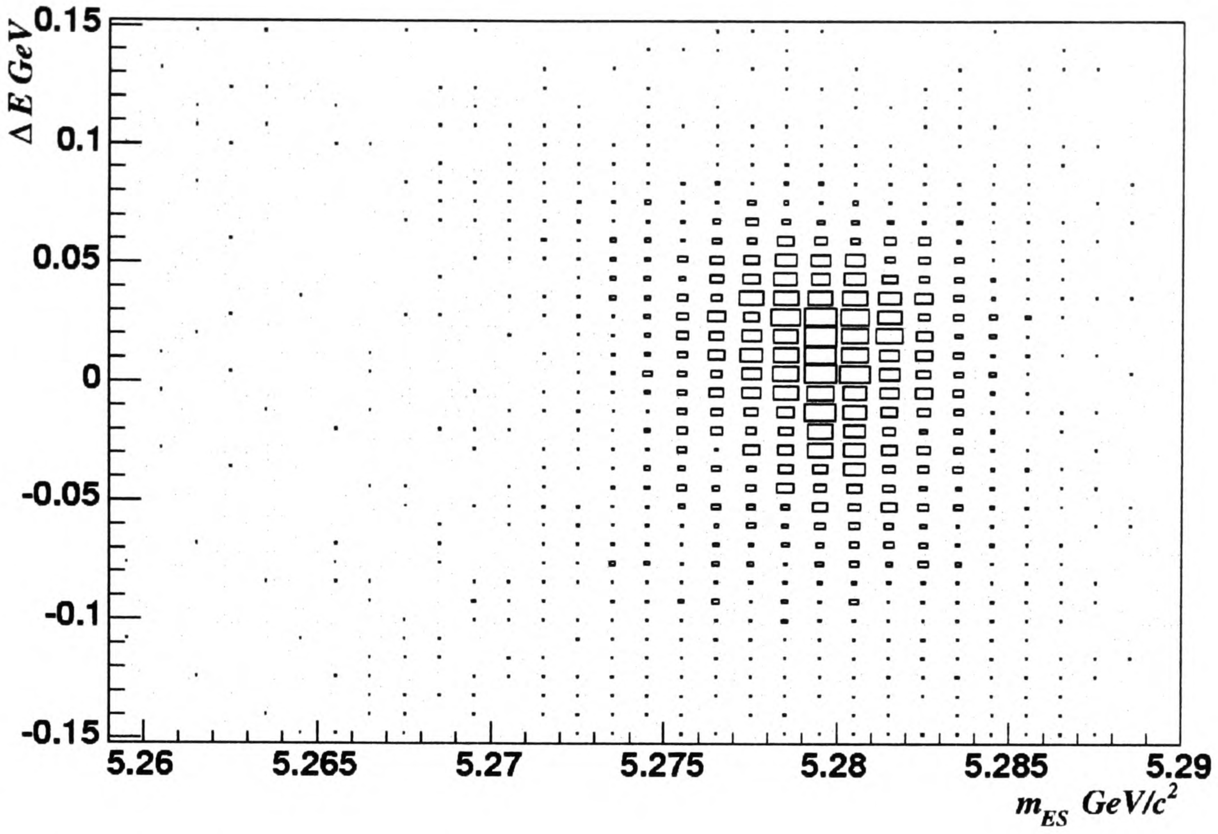

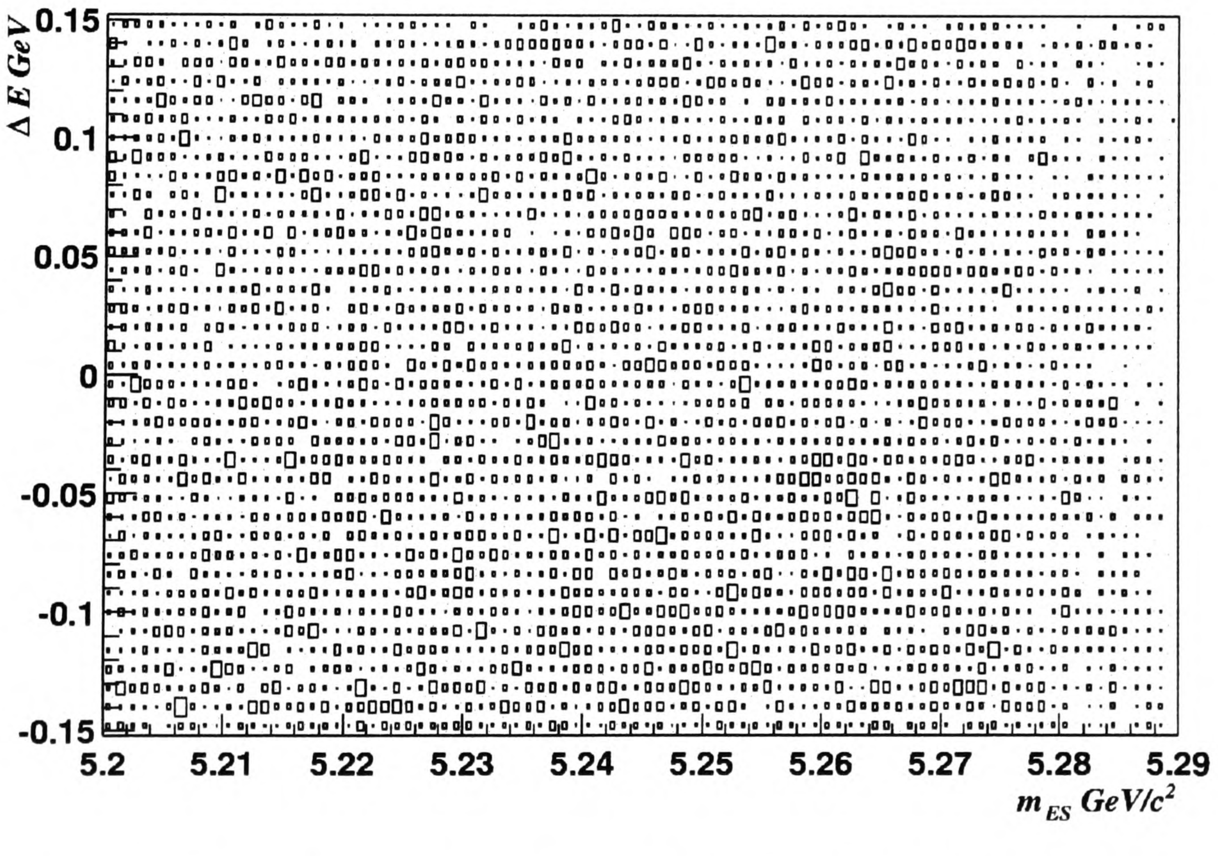

Figure 4.7: Top figure: Reconstructed signal $B^0 \to K^{*0}\pi^0$ Monte Carlo in m_{ES} versus ΔE. Bottom figure: m_{ES} versus ΔE for Monte Carlo continuum $q\bar{q}$, $q = u, d, s, c$ background.

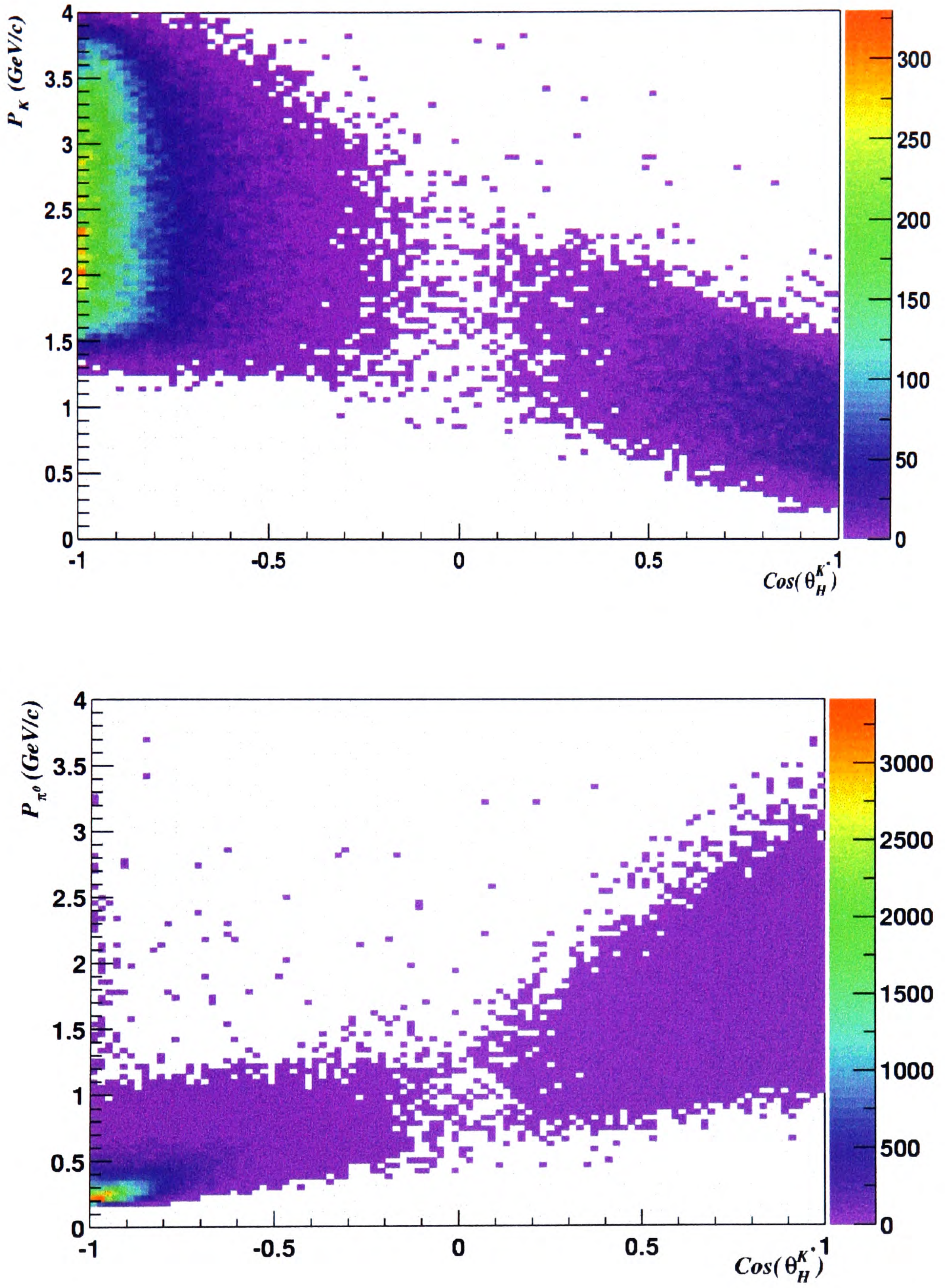

Figure 4.8: The momentum distributions of the charged kaon and the neutral π^0 candidates for the reconstructed K^{*+} against $\cos(\theta_H^{K^{*+}})$ in $B^0 \rightarrow K^{*+}\pi^-$ signal Monte Carlo. The plots shown contain all K^{*+} candidates with no mass cut. Thus, the large number of candidates where $\cos(\theta_H^{K^{*+}}) = -1$ is due to the abundance of low momentum π^0 candidates which combine with a fast kaon.

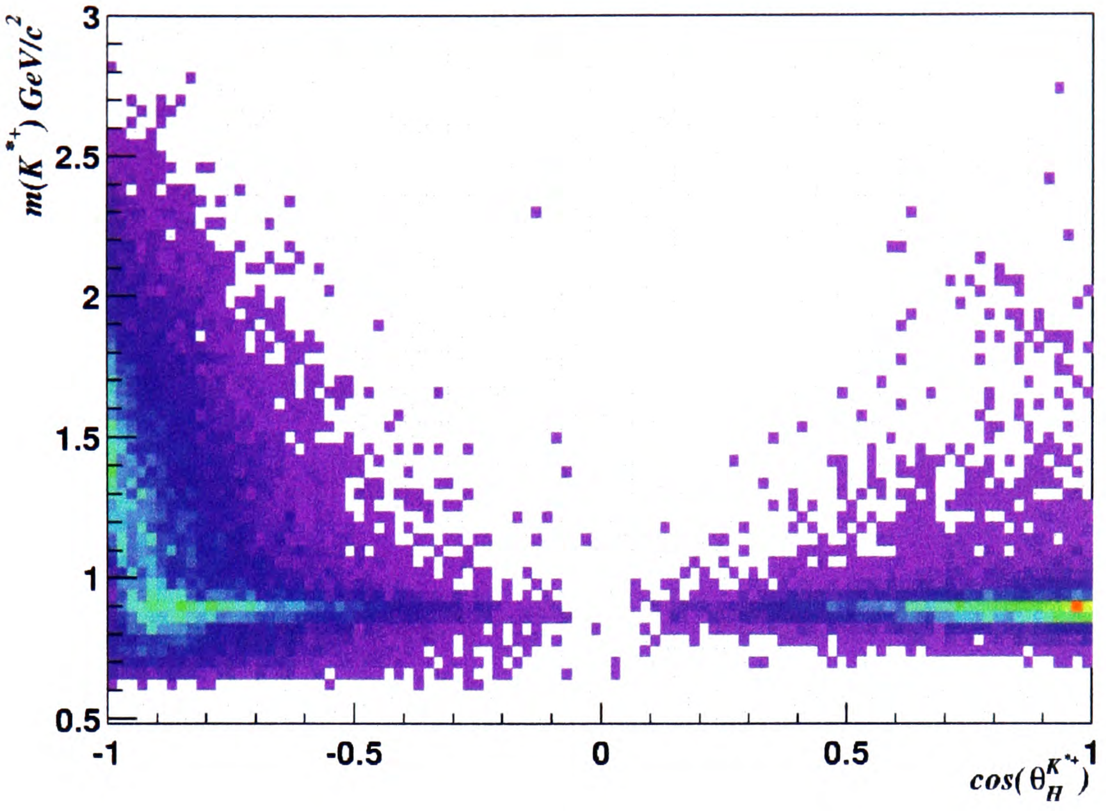

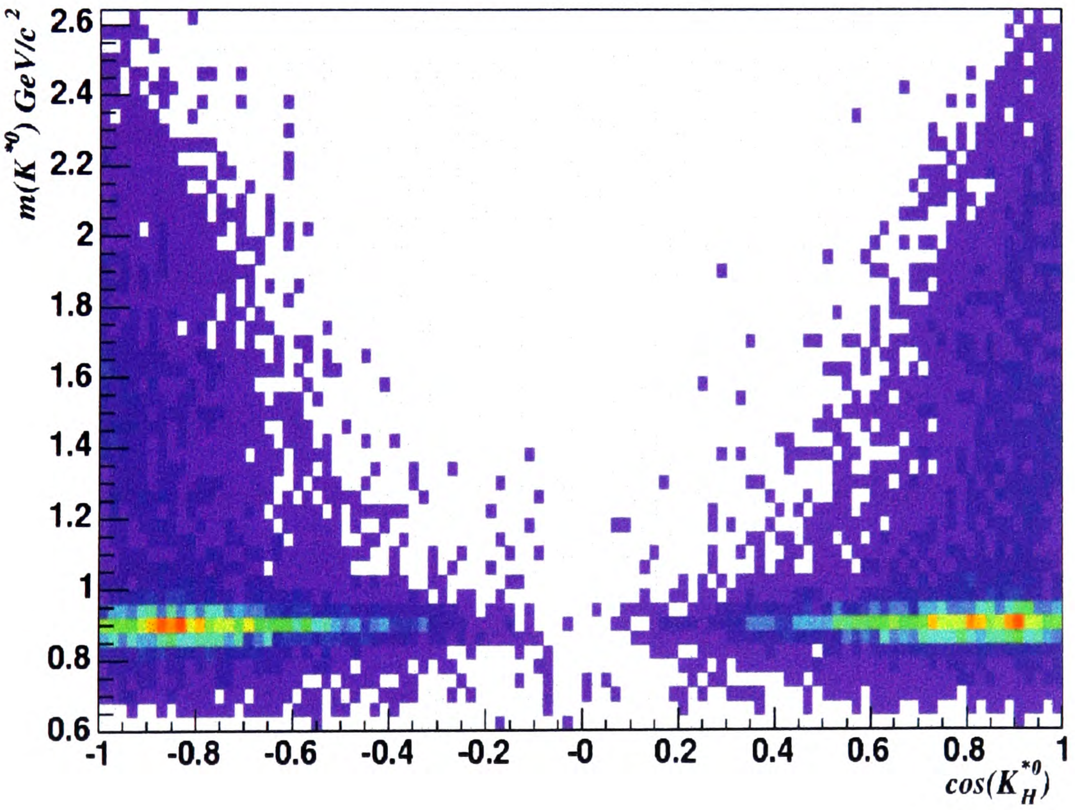

Figure 4.9: Top figure: $B^0 \to K^{*+}\pi^-$ Monte Carlo showing the invariant mass $m(K^+\pi^0)$ against the reconstructed helicity of the $K^+\pi^0$ combination. Bottom figure: $B^0 \to K^{*0}\pi^0$ Monte Carlo showing the invariant mass $m(K^+\pi^-)$ against the reconstructed helicity of the $K^+\pi^-$ combination.

4.6 Combinatoric backgrounds

For each of the analyses, further cuts on E_γ are made to reduce different backgrounds. In $B^0 \to K^{*+}\pi^-$ the large combinatoric component from multiple π^0 candidates presents the problem. For $B^0 \to K^{*0}\pi^0$ the problem background is from $B^0 \to K^{*0}\gamma$ decays.

4.6.1 $B^0 \to K^{*+}\pi^-$ combinatoric backgrounds

Combinatorial backgrounds arise from $B^0 \to K^{*+}\pi^-$ events due to multiple low energy π^0 candidates. For photons with energy E_γ below 100 MeV the reconstructed $m(\pi^0)$ distribution consists predominantly of fake π^0 candidates where at least one of the photons is not from a real π^0. This is shown[6] in figure 4.10 (top) where we see that these low energy photons combine with a photon of energy around $E_\gamma \approx 200\,\mathrm{MeV}$. The higher energy photon is combined multiple times with a random low energy background photon resulting in an abundance of fake π^0 candidates.

This combinatoric background component can be reduced by the selection of those π^0 candidates with photon energies $E_\gamma > 90$ MeV, see figure 4.10 (bottom). The value of $E_\gamma > 90\,\mathrm{MeV}$ is chosen by optimising $S^2/(S+B)$ where S is signal and B is the background. Here S is Monte Carlo $B^0 \to K^{*+}\pi^-$ and B is $q\bar{q}$ continuum Monte Carlo. In the case of continuum and other B decays the removal of low energy photons also helps to reduce the levels of combinatoric background.

A tighter selection range of $120\,\mathrm{MeV/c^2} < M_{\gamma\gamma} < 150\,\mathrm{MeV/c^2}$ is made on the reconstructed mass of the π^0 which also removes combinatorial π^0 candidates.

4.6.2 $B^0 \to K^{*0}\pi^0$ combinatoric backgrounds

For the $B^0 \to K^{*0}\pi^0$ analysis, harder cuts are required on the E_γ selection in order to reduce the level of background originating from $B^0 \to K^{*0}\gamma$, $K^{*0} \to K^+\pi^-$. The mode $B^0 \to K^{*0}\gamma$ enters as a background[7] when the high energy photon combines with

---

[6] The asymmetry in the photon distributions is not physically significant and is an artifact of the reconstruction method.

[7] Higher kaon resonance decays $B^0 \to K^{*0}(1410, 1430, 1610, ..)\gamma$ are also suppressed for identical reasons.

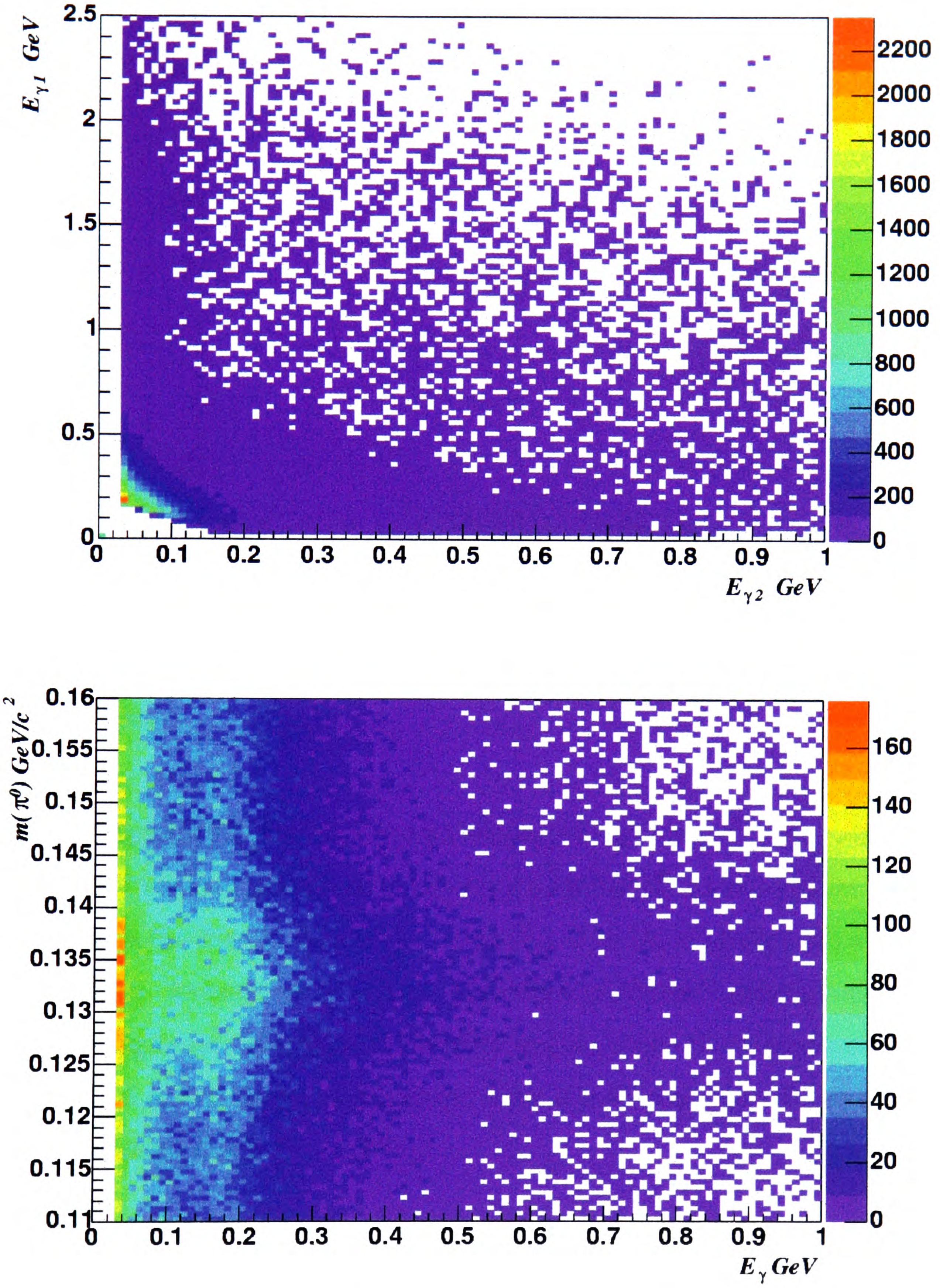

Figure 4.10: Monte Carlo $B^0 \to K^{*+}\pi^-$ with π^0 candidates satisfying the initial criteria in section 4.3. Top figure: Distribution of both photon energies from the reconstructed π^0 candidates. Bottom figure: Distribution of reconstructed π^0 mass against the energies of the both photons used to reconstruct the π^0.

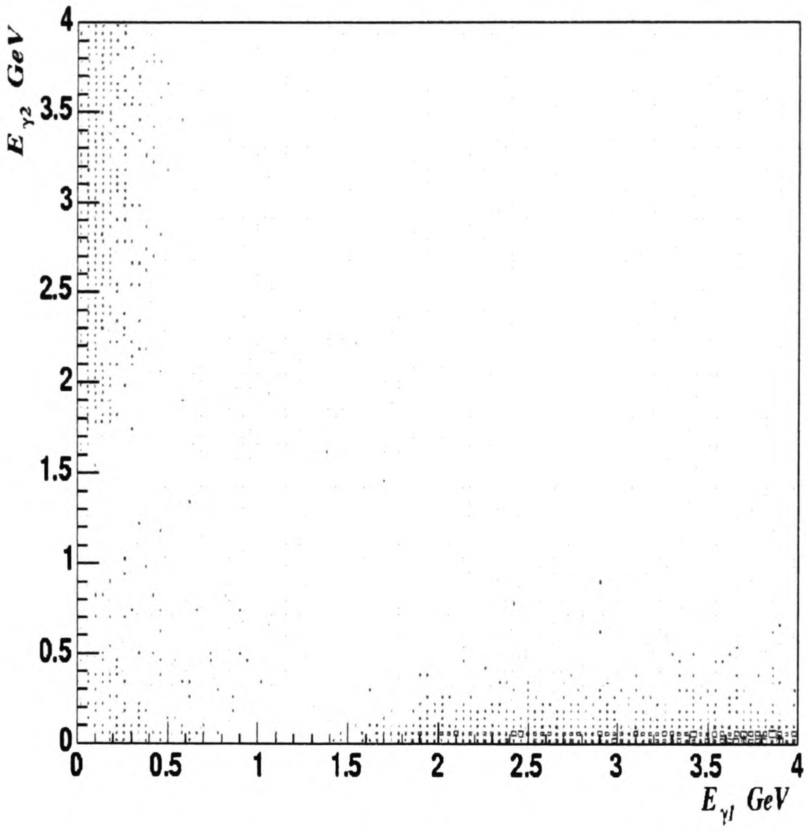

Figure 4.11: 2-D distribution of the photon energies of the reconstructed π^0 for $B^0 \to K^{*0}\gamma$ Monte Carlo.

another low energy photon from the event, reconstructing a fake π^0. This contamination from $B^0 \to K^{*0}\gamma$ can be suppressed by requiring a tighter cut on the photon energy E_γ. Figure 4.11 shows the distribution of E_{γ_1} versus E_{γ_2} from the reconstructed π^0 in Monte Carlo $B^0 \to K^{*0}\gamma$. As can clearly be seen, a selection of 150 MeV greatly suppresses the $B^0 \to K^{*0}\gamma$ background. The value of 150 MeV is determined by optimising $S^2/(S+B)$ where S is signal and B is the background. Here S is Monte Carlo $B^0 \to K^{*0}\pi^0$ and this time B is Monte Carlo $B^0 \to K^{*0}\gamma$.

4.7 Continuum backgrounds

The main background in rare 3 body B decay analyses arises from continuum events, $e^+e^- \to q\bar{q}$, $q = u, d, s, c$, where quark fragmentation occurs and hadronic jets are produced. These events have a larger probability to occur than $e^+e^- \to b\bar{b}$ events. The $q\bar{q}$ events are produced with very distinctive jet-like event topologies contrasted with $B\bar{B}$ events whose event topology is spherically isotropic. This difference in event topology can be exploited to remove the $q\bar{q}$ events while retaining much of the $B\bar{B}$ decay signal. In the following section we describe the sphericity variable and multivariate linear discriminant analysis method used to discriminate against the continuum $q\bar{q}$ background.

4.7.1 Event topology variables

The term event topology describes the distribution of the momenta of all charged and neutral particles reconstructed in an event. Continuum $q\bar{q}$ events are characterised by two correlated (back-to-back) jets of particles whereas in a $B\bar{B}$ event the distribution of the B decay particles is spherically isotropic due to the B mesons being produced almost at rest.

The sphericity tensor $S^{\alpha\beta}$ is given from [16] as:

$$S^{\alpha\beta} = \frac{\sum_i p_i^\alpha p_i^\beta}{\sum_i \vec{p}_i^2} \tag{4.3}$$

where $\alpha, \beta = 1, 2, 3$ correspond to the x, y, z components of momentum and the sum is over any combination of charged and neutral candidates in the event. A useful event subset is the 'Rest-Of-Event' (R.O.E) which is defined as all charged and neutral candidates in the event except those used to reconstruct the B candidate. From equation 4.3 the sphericity is defined as:

$$S = \frac{3}{2}(\lambda_2 + \lambda_3), \tag{4.4}$$

where λ_2 and λ_3 are the two largest eigenvalues of the sphericity tensor $S^{\alpha\beta}$. The sphericity axis is defined as the direction of the eigenvector corresponding to the largest eigenvalue of $S^{\alpha\beta}$.

Discrimination of the $q\bar{q}$ background is obtained by exploiting the angle θ^B_{sph} between the sphericity axis of the rest of the event and the direction of the reconstructed B. The cosine of the sphericity angle $\cos(\theta^B_{\mathrm{sph}})$, has a flat distribution for true $B\bar{B}$ pair events and is peaked at ±1 for jet-like continuum events due to the high correlation between the directions of the jets. Figure 4.12 shows the distribution of $\cos(\theta^B_{\mathrm{sph}})$ for continuum $q\bar{q}$, $q = u, d, s, c$ Monte Carlo, off-peak data, on-peak data and $B\bar{B}$ Monte

Carlo. To reduce background from $q\bar{q}$ continuum a selection on $\cos(\theta^B_{\mathrm{sph}})$ is made. The selection is chosen which maximises the signal significance over background using the ratio:

$$\frac{S^2}{S+B}. \tag{4.5}$$

where S denotes signal and B denotes background. The number of signal and background events are scaled to correspond to a luminosity of $81 fb^{-1}$ and a branching fraction of 1×10^{-6} is assumed for signal. The values are found to be $|\cos(\theta^B_{\mathrm{sph}})| < 0.7$ for $B^0 \to K^{*+}\pi^-$ and $|\cos(\theta^B_{\mathrm{sph}})| < 0.8$ for $B^0 \to K^{*0}\pi^0$. The difference in selection values for each mode is a result of the many more combinations per event for the $B^0 \to K^{*+}\pi^-$ mode. With these selections for $B^0 \to K^{*+}\pi^-$ we remove 90% of the continuum background while retaining 72.8% of the signal. For $B^0 \to K^{*0}\pi^0$ we remove 82.4% of the continuum background and retain 85.2% of the signal.

4.7.2 Multivariate linear discriminant analysis

Further discrimination of the $q\bar{q}$ background can be obtained using a multivariate linear discriminant method [48]. A discriminant variable $\mathcal{F}$ is formed from a linear sum of a set of n weighted event variables as:

$$\mathcal{F} = \sum_{i=1}^{n} \alpha_i x_i , \tag{4.6}$$

where each x_i is an event variable, and α_i is the chosen weight for that variable. The idea is find the set of weights α_i which maximise the separation between the signal and $q\bar{q}$ background classes by utilising all the information contained in the n variables.

The weights are determined by maximising the separation function $J(\vec{\alpha})$ given by:

$$J(\vec{\alpha}) = \frac{(\bar{\mathcal{F}}_S - \bar{\mathcal{F}}_B)^2}{\sigma_S^2 - \sigma_B^2} , \tag{4.7}$$

where $\bar{\mathcal{F}}$ and σ^2 are the expectation value and variance of the linear discrimination variable, S represents signal and B represents background. The signal distributions of the weighted selection variables are obtained from signal Monte Carlo, while the

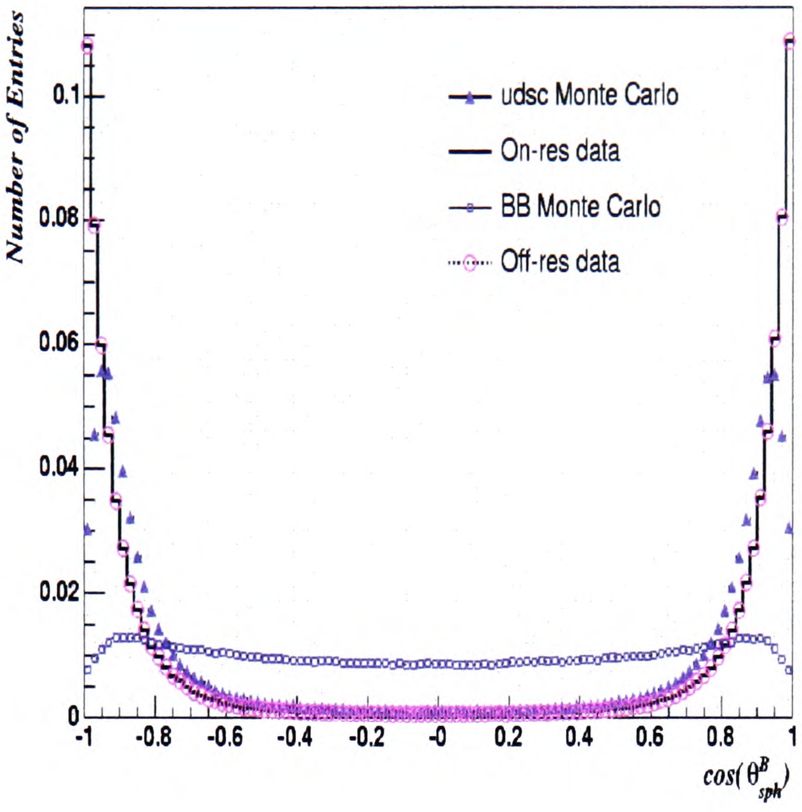

Figure 4.12: Cosine of the angle between the sphericity axes of the reconstructed B meson and the rest-of-event(ROE). Continuum $q\bar{q}$, $q = u, d, s, c$ Monte Carlo, off-peak data, on-peak data and $B\bar{B}$ Monte Carlo. The data distributions will also include events from e^+e^-, $\mu^+\mu^-$ and $\tau^+\tau^-$ events. These will also peak at the extremes $|\cos(\theta^B_{\text{sph}})| = 1$.

background distributions may be obtained from off-peak data, or continuum Monte Carlo.

The maximum separation is achieved by differentiation:

$$\frac{\partial J(\vec{\alpha})}{\partial \alpha} = 0, \tag{4.8}$$

The resulting matrix equation can be inverted to obtain the unique solution,

$$\alpha_i = \sum_{j=1}^{n} (V^B_{ij} + V^S_{ij})^{-1} (\mu^B_j - \mu^S_j), \tag{4.9}$$

where V_{ij} are the covariance matrices of the set of event variables and μ_j is the mean of the j^{th} variable.

The linear discriminant used in the analyses presented here consists of eleven weighted variables in the laboratory frame of reference. This particular discriminant was first used by the CLEO experiment [49] and contains the following event topology variables:

- The cosine of the angle between the thrust axis of the B meson and the beam axis,
- The cosine of the angle between the decay axis of the B meson and the beam axis, where the decay axis is the direction of flight of the B meson,
- The summed energy of the rest of the event that is contained within each of nine concentric energy cones about the thrust axis of the B meson.

In the analyses presented here the α_i weights for $\mathcal{F}$ have been optimised to provide maximum separation between signal and background for the analysis of the charmless hadronic ωh modes, where h is a kaon or pion. However, the discriminant still provides additional discrimination against continuum backgrounds after the selections on the $\cos(\theta^{B}_{\mathrm{sph}})$ variable.

4.8 The multivariate likelihood fit method

Further information on the multivariate maximum likelihood method may be found in [50]. Section 4.8.1 introduces the maximum likelihood method for parameter estimation. The methods used to determine the variance of maximum likelihood estimators are described in section 4.8.2. In section 4.8.3 the extended maximum likelihood method is introduced which is used to determine the signal yields for the analyses.

4.8.1 Parameter estimation

Given that the discriminating variables $\vec{x}$ are distributed according to the probability density functions (PDFs) $P(\vec{\alpha},\vec{x})$, where $\vec{\alpha}$ are parameters, not necessarily all known. If we measure the variables $\vec{x}$ N times and obtain the values $\vec{x}_j$ then the probability density for all the measurements, given that they are independent, is the likelihood function:

$$\mathcal{L}(\vec{\alpha}) = \prod_{j=1}^{N} P(\vec{\alpha}, \vec{x}_j). \tag{4.10}$$

The function $\mathcal{L}$ obtains its maximum value when the chosen functional forms and parameters of the PDFs correctly describe the distributions of the measured variables. If the functional form for P is fixed, then the values of $\vec{\alpha}$ which maximise $\mathcal{L}$ form a set of **estimators** for the parameters $\vec{\alpha}$. These estimators denoted $\hat{\alpha}$ are known as *Maximum Likelihood Estimators.* For computational purposes it is convenient to maximise the quantity $-\log\mathcal{L} = \sum_{j=1}^{N} \log P(\vec{\alpha}, \vec{x}_j)$ which converts the product into a sum.

4.8.2 Variance of maximum likelihood estimators

Given estimates for a set of parameters which have been determined from a maximum likelihood(M.L.) fit we would like to assign some measure of the statistical uncertainty on these estimates. Here we provide the most commonly used methods to determine the variance of M.L. estimators.

A lower bound on the variance of a maximum likelihood estimator can be obtained using the form of the Rao-Cramer-Frechet inequality given in [50]. In the large sample limit we may obtain the covariance matrix for a set of M.L. estimators α_i as:

$$V_{ij}^{-1} = -\frac{\partial^2(-\log\mathcal{L})}{\partial\alpha_i\alpha_j}. \tag{4.11}$$

Another common method to determine the variance of an M.L. estimator is to Taylor expand around the maximum of $-\log(\mathcal{L})$ which gives in the case of one estimator α:

$$\log\mathcal{L}(\alpha) = \log\mathcal{L}(\hat{\alpha}) + \left[\frac{\partial\log\mathcal{L}}{\partial\alpha}\right]_{\alpha=\hat{\alpha}}(\delta\alpha) + \frac{1}{2!}\left[\frac{\partial^2\log\mathcal{L}}{\partial\alpha^2}\right]_{\alpha=\hat{\alpha}}(\delta\alpha)^2 + \cdots. \tag{4.12}$$

$\log\mathcal{L}(\hat{\alpha}) = \log\mathcal{L}_{\max}$ and by definition $[\frac{\partial\log\mathcal{L}}{\partial\alpha}]_{\alpha=\hat{\alpha}} = 0$ thus ignoring higher terms, the distribution of $\log\mathcal{L}$ is approximately parabolic and is Gaussian distributed around $\hat{\alpha}$. The error on the estimator is obtained using:

$$-\log\mathcal{L}(\hat{\alpha} \pm \hat{\sigma}_{\hat{\alpha}}) = \log\mathcal{L}_{\max} - \frac{1}{2}, \tag{4.13}$$

where $\hat{\sigma}_{\hat{\alpha}} = (\alpha - \hat{\alpha})^2/\hat{\sigma}^2{}_{\hat{\alpha}}$.

4.8.3 Extended maximum likelihood

The above discussion is sufficient for determining the parameters in the distributions of our discriminating variables. In order to determine the total normalisation from the fit we must extend the likelihood function of section 4.10. The normalisation of the fit or total fit yield may be written as $N = \sum_i N_i$ where each N_i represents signal or background categories distributed according to Poisson distributions [50] with mean ν. The *extended likelihood function* [50] is given by:

$$\mathcal{L}(\nu, \vec{\alpha}) = \frac{\nu^N}{N!} e^{-\nu} \prod_{j=1}^{N} P(\vec{\alpha}, \vec{x}_j) = \frac{e^{-\nu}}{N!} \prod_{j=1}^{N} \nu P(\vec{\alpha}, \vec{x}_j). \tag{4.14}$$

Rewriting $\nu = \sum_i n_i$ where n_i are the expected number of events for each category k then we can write,

$$\mathcal{L} = \exp\left(-\sum_{i=1}^{M} n_i\right) \prod_{j=1}^{N} \left(\sum_{k=1}^{M} n_k P_k(\vec{\alpha}, \vec{x}_j)\right). \tag{4.15}$$

This extended likelihood function is used to determine the signal yield $N_{\rm sig}$.

For each analysis, the variables ΔE, m_{ES}, $\mathcal{F}$, $m(K^*)$ and $\cos(\theta_H^{K^*})$ form the set of discriminating variables to be used in constructing the maximum likelihood function. For each event i we define:

$$\mathcal{P}_i = N_{K^*\pi} \mathcal{P}^{K^*\pi} + \sum_{B_j} N_{B_j} \mathcal{P}^{B_j} \tag{4.16}$$

where $N_{K^*\pi}$ is the number of reconstructed $B^0 \to K^{*+}\pi^-$ or $B^0 \to K^{*0}\pi^0$ and N_{B_j} represents the number of each reconstructed background category. The term $\mathcal{P} = P(\Delta E) \times P(m_{ES}) \times P(m(K^*)) \times P(\cos(\theta_H^{K^*})) \times P(\mathcal{F})$ for each event category.

Chapter 5

Branching fraction analysis of $B^0 \to K^{*+}\pi^-$

5.1 Introduction

In this chapter we describe the analysis of the neutral B decay mode $B^0 \to K^{*+}\pi^-, K^{*+} \to K^+\pi^0$. The principal goal of the analysis is to measure a $B^0 \to K^{*+}\pi^-$ signal yield and hence determine the branching fraction $\mathcal{BR}(B^0 \to K^{*+}\pi^-)$. The measurement of the number of $B^0 \to K^{*+}\pi^-$ events is determined using an extended maximum likelihood fit. For this analysis, we use a 5 dimensional probability distribution which includes the variables, ΔE, m_{ES}, $m(K^*)$, $\cos(\theta_{\mathrm{H}}^{K^*})$, $\mathcal{F}$. In section 5.2 we discuss the correlations in the proposed fit variables. The selection efficiencies are given in section 5.3. In section 5.4 we describe the parameterisation of the fit variables. The backgrounds arising from other B meson decays are discussed in section 5.5. In section 5.6 the procedures used to validate the fit are described. We present the results of the fit in section 5.8 and the analysis of the systematic errors is discussed in section 5.9. We end with the measurement of the branching fraction which is given in section 5.10.

The analysis studies the following different event types using the samples of Monte Carlo and data described in section 4.1.

- $B^0 \to K^{*+}\pi^-$ events.

- Continuum background from $e^+e^- \to q\bar{q}$, $q = u, d, s, c$.
- $B\bar{B}$ background from other B decay modes.

5.2 Correlations in fit variables

In order to use the maximum likelihood technique the variables used in constructing the likelihood function must be independent for each event type. This section serves to determine whether the proposed variables to be used in the fit are sufficiently independent of one another. We start by examining the correlation matrix and identify pairs of variables where the correlation[1] is greater than 10%. Pairs of variables which fail this criterium are studied separately in greater depth. The correlation matrix for continuum $q\bar{q}$ is given in table 5.1 estimated using a large statistics sample of continuum Monte Carlo. The results show no significant correlation between each pair of variables.

	ΔE	$\cos(\theta_H^{K^{*+}})$	$m(K^{*+})$	m_{ES}	$\mathcal{F}$
ΔE	1				
$\cos(\theta_H^{K^{*+}})$	-0.006	1			
$m(K^{*+})$	0.001	-0.007	1		
m_{ES}	-0.012	0.017	0.012	1	
$\mathcal{F}$	-0.031	0.042	0.011	0.015	1

Table 5.1: Correlation matrix for the maximum likelihood fit variables for the $q\bar{q}$ background.

Table 5.2 gives the correlation matrix estimated from $B^0 \to K^{*+}\pi^-$ Monte Carlo. We see that the main correlations in signal $B^0 \to K^{*+}\pi^-$ occur in the following pairs of variables, $\{\cos(\theta_H^{K^{*+}}), \Delta E\}$ and $\{\cos(\theta_H^{K^{*+}}), m_{ES}\}$ which we now study. The principal aim will be to determine the source of the correlations and remove them.

---

[1] Any pairs of variables with correlation coefficient $\rho < 10\%$ are considered to be independent

	ΔE	$\cos(\theta_H^{K^{*+}})$	$m(K^{*+})$	m_{ES}	$\mathcal{F}$
ΔE	1				
$\cos(\theta_H^{K^{*+}})$	**-0.118**	1			
$m(K^{*+})$	0.057	-0.044	1		
m_{ES}	-0.024	**0.190**	-0.036	1	
$\mathcal{F}$	-0.031	-0.027	-0.005	-0.059	1

Table 5.2: Signal $B^0 \to K^{*+}\pi^-$ Monte Carlo correlation matrix.

5.2.1 Correlations in $\cos(\theta_H^{K^{*+}})$ and ΔE

From figure 4.8 we have seen that positive $\cos(\theta_H^{K^{*+}})$ is predominantly associated with the K^{*+} having a fast π^0 and a slow K^+ whereas negative $\cos(\theta_H^{K^{*+}})$ is associated with the K^{*+} having a slow π^0 and a fast K^+.

In figure 5.1 we show $\cos(\theta_H^{K^{*+}})$ against ΔE and in figure 5.2 we show the distribution of ΔE for both positive and negative ranges of $\cos(\theta_H^{K^{*+}})$. We can parameterise the general shape of the ΔE distribution using an asymmetric Gaussian on a linear polynomial background. In table 5.3 we give the variation in the parameters of ΔE as a function of $\cos(\theta_H^{K^{*+}})$. The parameters σ_C^L, σ_C^R are respectively the left and right sided widths of the asymmetric Gaussian. μ_C is the mean of the Gaussian distribution, c_1 is the first order coefficient of the polynomial background and Frac_C is the contribution of the Gaussian component relative to the polynomial component. The use of an asymmetric Gaussian is required in order to model the broadening of ΔE when the π^0 has high momentum. This broadening which is evident in the variation of σ_C^L is attributable to the energy resolution of the EMC in reconstructing high energy π^0 particles. For $\cos(\theta_H^{K^{*+}}) < 0$ we see that the ΔE distribution is well described using a symmetric Gaussian with a width of 0.0267 GeV on a uniform background. This uniform background in the range $-1.0 \leqslant \cos(\theta_H^{K^{*+}}) \leqslant -0.7$ is solely due to low energy combinatoric π^0 candidates in the reconstruction of $K^{*+} \to K^+\pi^0$. By requiring $\cos(\theta_H^{K^{*+}}) > -0.7$ we see that we can remove these candidates and minimise the variation in the ΔE parameters. Neglecting the variation in σ_C^L will result in our model over-estimating the

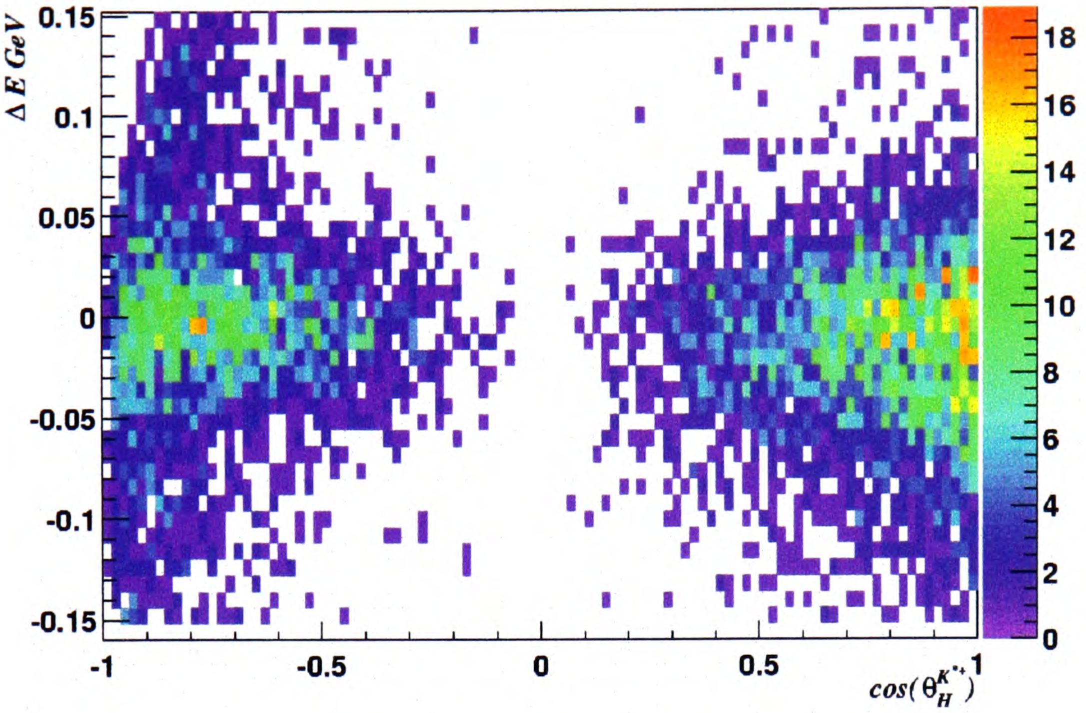

Figure 5.1: 2-D distribution of $\cos(\theta_H^{K^{*+}})$ against ΔE in signal $B^0 \to K^{*+}\pi^-$ Monte Carlo. All the B candidates are reconstructed as in the previous chapter 4 along with the tightened E_γ cut.

probability of an event with $\Delta E < 0$ and $\cos(\theta_H^{K^{*+}}) < 0$ to be signal. Therefore, we include the variation in σ_C^L within the model definition of ΔE.

5.2.2 Correlations in $\cos(\theta_H^{K^{*+}})$ and m_{ES}

Figure 5.3 shows the distribution of the energy substituted mass m_{ES} against $\cos(\theta_H^{K^{*+}})$ in signal Monte Carlo. The region $-1.0 \leqslant \cos(\theta_H^{K^{*+}}) \leqslant -0.5$ contains the badly reconstructed signal which manifests itself as a large tail in the distribution of m_{ES}. The distribution of m_{ES} is parameterised using the Crystal Ball function given by:

$$f_{CB}(m_{ES};\mu,\sigma,\alpha,n) = \frac{1}{N}\begin{cases} \frac{(n/\alpha)^n \exp(-\alpha^2/2)}{((\mu-m_{ES})/(\sigma+n/\alpha-\alpha))^n}, & m_{ES} \leq \mu-\alpha\sigma \\ \exp(-\frac{(m_{ES}-\mu)^2}{2\sigma^2}), & m_{ES} > \mu-\alpha\sigma \end{cases} \tag{5.1}$$

where μ is the mean of the distribution, σ is the width and the parameters α and n describe the tail. The shape of the Crystal Ball function is not affected by the value of the n parameter unless the tail component is large i.e. (the range $-1.0 \leq \cos(\theta_H^{K^{*+}}) \leq$

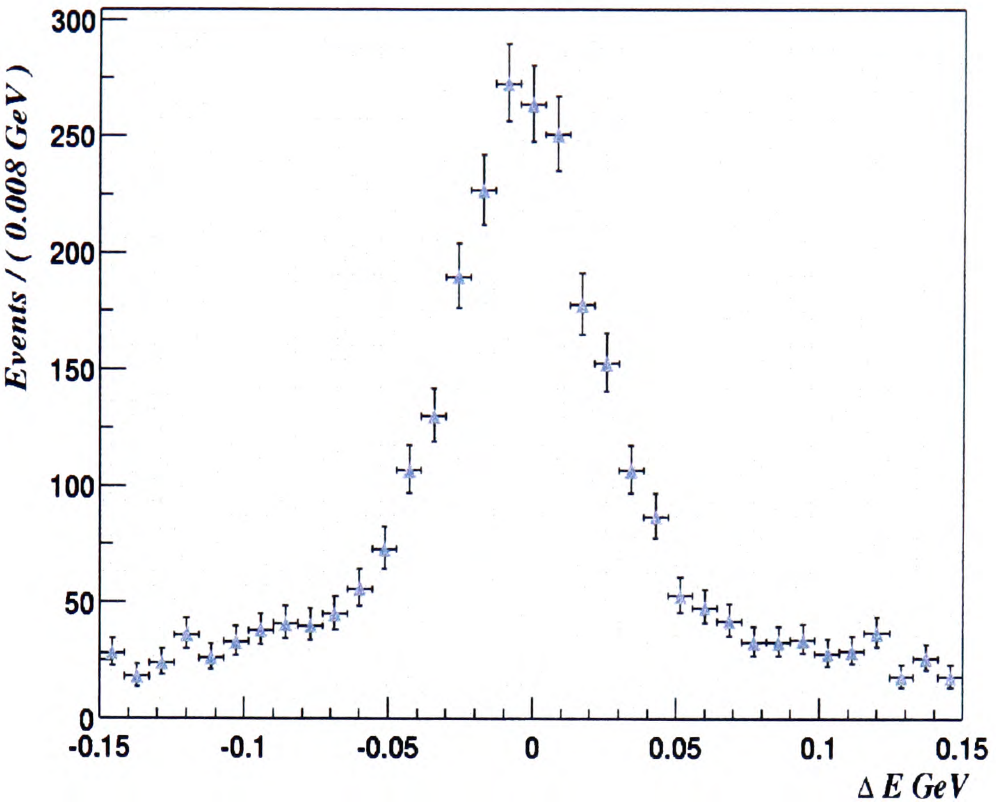

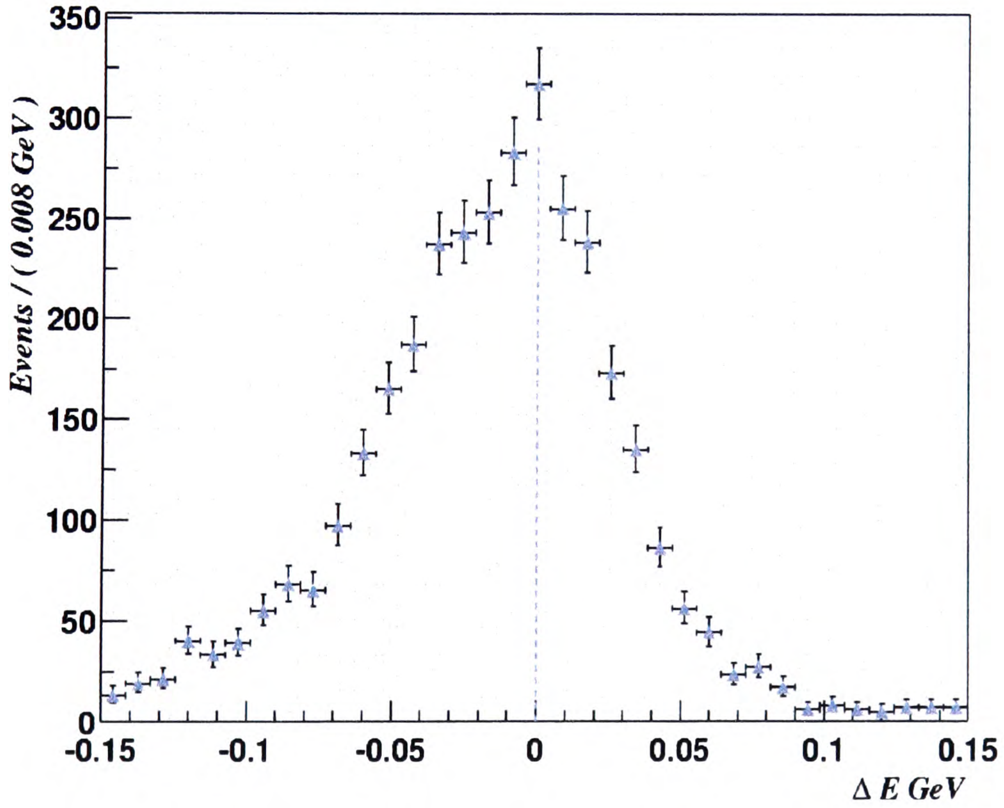

Figure 5.2: Signal $B^0 \to K^{*+}\pi^0$ Monte Carlo with all selection cuts applied. Top figure: ΔE distribution for $\cos(\theta_H^{K^{*+}}) < 0$. Bottom figure: ΔE distribution for $\cos(\theta_H^{K^{*+}}) > 0$.

ΔE	$-1.0 \leq \cos(\theta_H^{K^{*+}}) \leq -0.5$	$-0.5 \leq \cos(\theta_H^{K^{*+}}) \leq 0.0$
μ_C	-0.0033 ± 0.0024	-0.0060 ± 0.0035
σ_C^L	0.0258 ± 0.0021	0.0263 ± 0.0025
σ_C^R	0.0267 ± 0.0021	0.0263 ± 0.0024
c_1	-0.5065 ± 0.4180	-3.2030 ± 1.6083
Frac_C	0.5833 ± 0.0174	0.8799 ± 0.0228

ΔE	$0.0 \leq \cos(\theta_H^{K^{*+}}) \leq 0.6$	$0.6 \leq \cos(\theta_H^{K^{*+}}) \leq 1.0$
μ_C	-0.0027 ± 0.0040	-0.0027 ± 0.0023
σ_C^L	0.0402 ± 0.0033	0.0460 ± 0.0024
σ_C^R	0.0263 ± 0.0028	0.0309 ± 0.0016
c_1	-3.4826 ± 1.4050	-3.4802 ± 0.8559
Frac_C	0.8866 ± 0.0236	0.8661 ± 0.0203

Table 5.3: The variation in ΔE Parameters for an asymmetric Gaussian and first order polynomial as a function of $\cos(\theta_H^{K^{*+}})$.

$\cos(\theta_H^{K^{*+}})$	μ (GeV/c^2)	σ (MeV/c^2)	α	n
$[-1.0, -0.5]$	5.280 ± 0.001	2.80 ± 0.20	0.733 ± 0.035	4.766 ± 0.588
$[-0.5, 0.0]$	5.280 ± 0.001	2.80 ± 0.20	1.701 ± 0.181	10.0
$[0.0, 0.5]$	5.280 ± 0.001	2.80 ± 0.20	1.779 ± 0.109	10.0
$[0.5, 1.0]$	5.280 ± 0.001	2.80 ± 0.20	1.609 ± 0.107	10.0

Table 5.4: The fitted Crystal Ball parameters for m_{ES} showing the invariance of the parameters as a function of $\cos(\theta_H^{K^{*+}})$.

-0.5). When the tail is small then we fix the value of n to 10. Table 5.4 shows the variation of the m_{ES} parameters as a function of $\cos(\theta_H^{K^{*+}})$. We see that only the parameters describing the tail are dependent on $\cos(\theta_H^{K^{*+}})$. To eliminate this dependence as well as the correlations in $\cos(\theta_H^{K^{*+}})$ and ΔE we apply the selection criterium $-0.7 < \cos(\theta_H^{K^{*+}}) < 1.0$. After this selection the correlation coefficient between m_{ES} and $\cos(\theta_H^{K^{*+}})$ becomes -0.03.

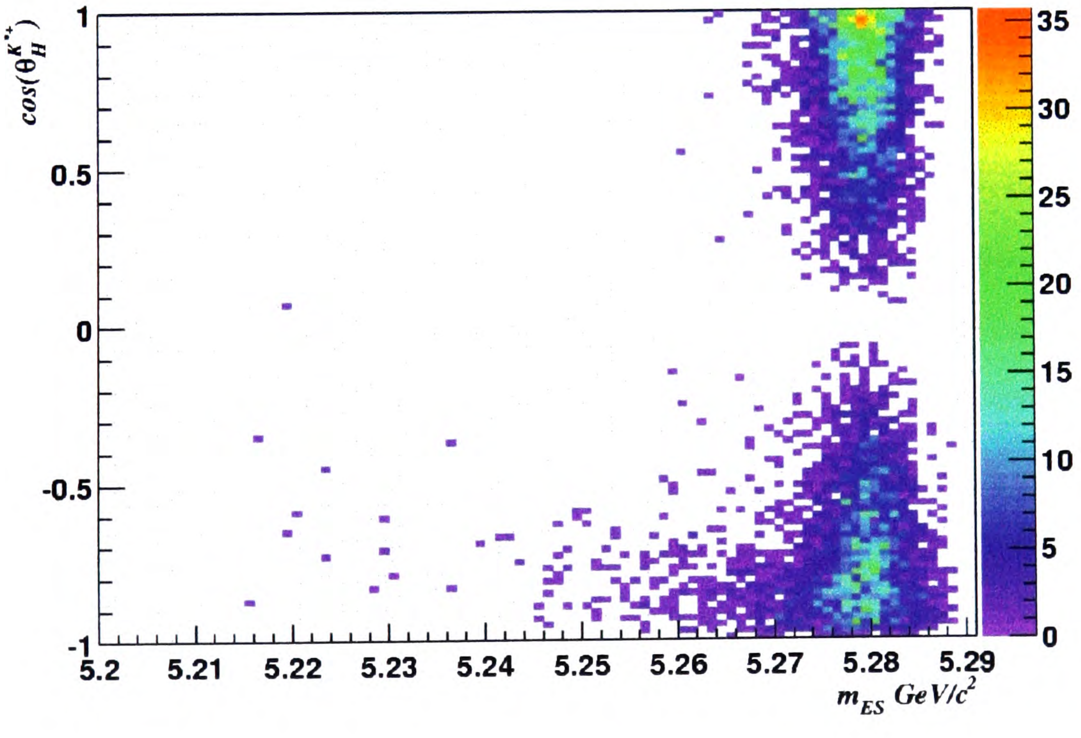

Figure 5.3: Signal $B^0 \rightarrow K^{*+}\pi^-$ Monte Carlo. 2-D distribution of $\cos(\theta_H^{K^{*+}})$ against m_{ES}.

5.3 Selection efficiencies for $B^0 \to K^{*+}\pi^-$

In the previous sections we have discussed those additional selections which reduce the number of combinatoric candidates per event and remove correlations from our fit variables. In table 5.5 we give all candidate and event selection efficiencies for signal $B^0 \to K^{*+}\pi^-$ Monte Carlo with each efficiency given relative to the previous selection. From the selections on E_γ and in $\cos(\theta_{\rm H}^{K^{*+}})$ we see the striking effect in reducing the number of candidates. However, even after all selections are applied there are still events which contain multiple candidates per event. This number is small where we find that only 2.4% of events contain multiple candidates. We choose to select a single candidate per event using random selection. This has the benefit that it does not introduce any bias into the selection criteria. We find that the total event selection efficiency for $B^0 \to K^{*+}\pi^-$ is $12.07 \pm 0.15\%$.

In table 5.6 we show the event selection efficiencies for $81.878\, fb^{-1}$ on-peak data, $9.578\, fb^{-1}$ off-peak data, $1043\, fb^{-1}$ *udsc* continuum Monte Carlo and $140.5\, fb^{-1}$ combined $B\bar{B}$ Monte Carlo (signal $B^0 \to K^{*+}\pi^-$ signal events removed). Each efficiency is given relative to the previous selection.

Since the off-peak data consists mainly of continuum $q\bar{q}$ events we would expect the continuum $q\bar{q}$ Monte Carlo efficiency to be similar to the off-peak data efficiency. However, We find that there is a factor of 2 difference between these two efficiencies. From figure 4.12 we see that in the sphericity variable $\cos(\theta_{\rm sph}^{B})$ the continuum $q\bar{q}$ Monte Carlo does not describe data well in the extremes of the $\cos(\theta_{\rm sph}^{B})$ distribution. Looking at table 5.6 we see that for all other selection variables the off-peak data and Monte Carlo continuum efficiencies are similar. We may thus conclude that the factor of two difference in efficiency is due to the differences in the $\cos(\theta_{\rm sph}^{B})$ distribution.

We find that 2053 on-peak events and 250 off-peak events remain after all selections have been applied.

Pre-selected number of $K^{*+}\pi^-$ candidates	151864	-
Pre-selected number of $K^{*+}\pi^-$ events	-	29733
Eff(%) $B^0 \to K^{*+}\pi^-$	Candidates	Events
$\lvert\cos(\theta^B_{\mathrm{sph}})\rvert < 0.7$	66.9	72.8
Neutral selection		
$E_\gamma > 90.0\,\mathrm{MeV}$	42.6	83.0
$0.12 < m(\pi^0) < 0.15\,\mathrm{GeV/c^2}$	68.5	89.3
Charged track selection		
πK PID	75.2	78.2
K^{*+} resonance		
$0.8 < m(K^{*+}) < 1.0\,\mathrm{GeV/c^2}$	45.1	67.8
$-0.7 < \cos(\theta_H^{K^{*+}}) < 1.0$	67.9	76.5
B candidate		
$\lvert\Delta E\rvert < 150\,\mathrm{MeV}$	92.5	94.6
$5.2 < m_{ES} < 5.29\,\mathrm{GeV/c^2}$	99.9	100
Total	4.15	12.07

Table 5.5: Selection efficiencies in $\epsilon(\%)$ for $B^0 \to K^{*+}\pi^-$ Monte Carlo, First column: Candidate selection efficiencies for all reconstructed B candidates. Second column: Per event selection efficiencies.

Eff(%)	ϵ(onpeak)	ϵ(offpeak)	ϵ(udsc M.C.)	$\epsilon(B\bar{B})$
Data pre-selection	2.1	2.1	-	-
M.C. pre-selection	-	-	2.1	0.2
$\lvert\cos(\theta^B_{\mathrm{sph}})\rvert < 0.7$	10.0	8.5	16.8	64.9
Neutral selection				
$E_\gamma > 90.0\,\mathrm{MeV}$	74.8	71.5	71.5	66.1
$0.12 < m(\pi^0) < 0.15\,\mathrm{GeV/c^2}$	81.9	78.7	79.2	80.1
Charged track selection				
πK PID	27.3	25.7	26.5	25.7
K^{*+} resonance				
$0.8 < m(K^{*+}) < 1.0\,\mathrm{GeV/c^2}$	7.6	6.4	6.5	2.4
$-0.7 < \cos(\theta_H^{K^{*+}}) < 1.0$	74.8	86.3	80.9	57.1
B candidate				
$\lvert\Delta E\rvert < 150\,\mathrm{MeV}$	37.4	36.2	34.7	22.9
$5.2 < m_{ES} < 5.29\,\mathrm{GeV/c^2}$	88.6	86.1	89.4	92.2
Total	6.6×10^{-6}	4.4×10^{-6}	8.6×10^{-6}	0.7×10^{-6}

Table 5.6: Selection efficiencies for on-peak data, off-peak data, $140.5\,fb^{-1}$ $B\bar{B}$ Monte Carlo and $1043\,fb^{-1}$ udsc Monte Carlo.

5.4 Parameterisation of signal & continuum background

The parameterisations of the PDFs for the fit variables are determined from $B^0 \rightarrow K^{*+}\pi^-$ Monte Carlo and continuum $q\bar{q}$ Monte Carlo. Figure 5.4 and figure 5.5 show the distributions of each fit variable. Also shown are the results of an unbinned maximum likelihood fit used to determine the initial parameterisations of the fit variables. The primary goal is to establish the shapes of the probability density functions. The goodness of fit quality of the parameterisations is determined later in section 5.6.1.

- m_{ES}: The shape for the energy substituted mass m_{ES} is parameterised with the Crystal Ball function defined in section 5.2.2. The m_{ES} continuum background shape is parameterised with the phase space ARGUS [51] function:

  $$f_A(m_{ES}\,; m_0, \xi) = \frac{1}{N} m_{ES} \sqrt{1-(m_{ES}/m_0)^2}\, \exp(\xi(1-(m_{ES}/m_0)^2)), \qquad (5.2)$$

  where m_0 is the endpoint fixed to 5.29 GeV/c^2 and ξ is the ARGUS shape parameter. The value of the shape parameter $\xi(m_{ES})$ is determined from data in the maximum likelihood fit.

- ΔE: The signal shape for ΔE is parameterised using an asymmetric Gaussian on a first order polynomial background. The shape of ΔE in signal is discussed in section 5.2.1. For continuum background the ΔE shape is parameterised with a first order polynomial function.

- Linear discriminant $\mathcal{F}$: The shape for the linear discriminant $\mathcal{F}$ for both signal and continuum is parameterised with a Gaussian distribution.

- $K^{*+}(892)$ mass: The K^{*+} line shape is parameterised using a Breit-Wigner distribution:

  $$BW(x; m, \Gamma) = \frac{1}{N} \frac{1}{(x-m)^2 + (\Gamma/2)^2}. \qquad (5.3)$$

where N is the normalisation factor and the parameters m and Γ are the mass and width of the K^* resonance. The continuum background is described with a combination of a Breit-Wigner and first order polynomial background.

- $\cos(\theta_H^{K^{*+}})$: The shape of $\cos(\theta_H^{K^{*+}})$ for both signal and continuum is parameterised with a 2nd order Chebyshev polynomial function. The Chebyshev polynomials are orthonormal in the range $[-1,1]$ where the first three Chebyshev polynomials are given by:

$$T_0(x) = 1; \quad T_1(x) = x; \quad T_2(x) = 2x^2 - 1. \tag{5.4}$$

The continuum $\cos(\theta_H^{K^{*+}})$ distribution would be expected to be flat. However, the quadratic term is required to model the region $\cos(\theta_H^{K^{*+}}) < -0.5$ which contains a greater number of candidates constructed with low energy π^0's.

5.5 $B\bar{B}$ backgrounds in $B^0 \to K^{*+}\pi^-$

Backgrounds arise from other B decays with similar characteristics to the signal mode under study. These backgrounds can be difficult to remove because of their similarity to the signal B. Furthermore, even after identifying potential background modes, estimating the level of contamination will depend on the uncertainty of the branching fractions of these modes.

In order to determine the B background modes specific to $B^0 \to K^{*+}\pi^-$, samples of $71.9\, fb^{-1}$ B^+B^- and $68.6\, fb^{-1}$ $B^0\bar{B}^0$ Monte Carlo were generated and reconstructed, using the $B^0 \to K^{*+}\pi^-$ selections described in section 5.3. The samples of $B\bar{B}$ contain properly weighted contributions of charm decay modes ($B \to X_c, X_c = D, D^*, ..$), charmless decay modes and provide the basis for the analysis of B backgrounds. From these samples we are able to estimate the expected level of background and determine the general structure of the B background.

The distributions for ΔE, $\cos(\theta_H^{K^{*+}})$, $m(K^{*+})$, m_{ES}, $\mathcal{F}$ are shown in figure 5.6 for B^+B^- and $B^0\bar{B}^0$ Monte Carlo. All selection cuts in section 5.3 have been applied to the $B\bar{B}$ Monte Carlo. Table 5.7 gives the number of reconstructed $B\bar{B}$ events for the

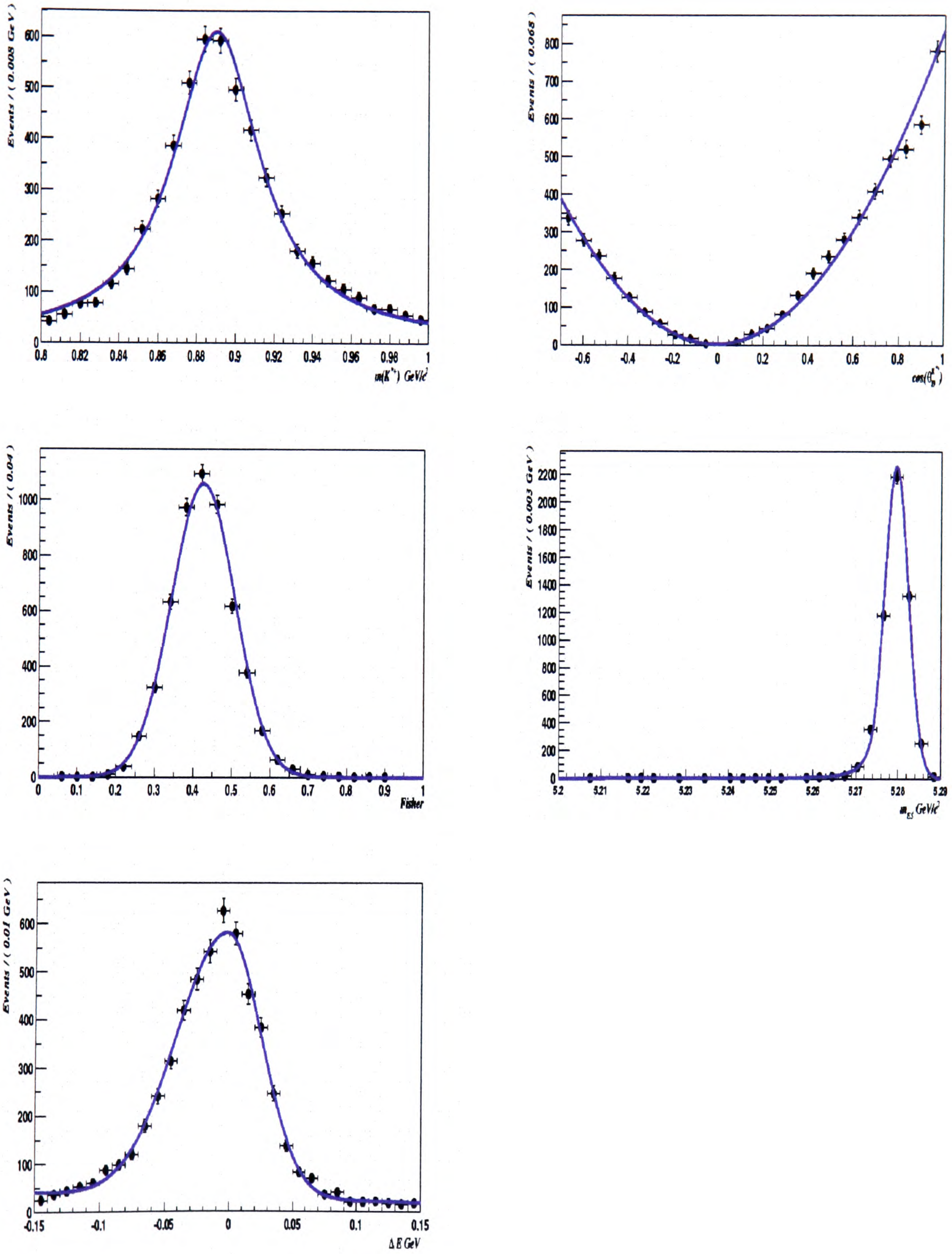

Figure 5.4: Parameterisations of the maximum likelihood fit variables for signal $B^0 \to K^{*+}\pi^-$ Monte Carlo.

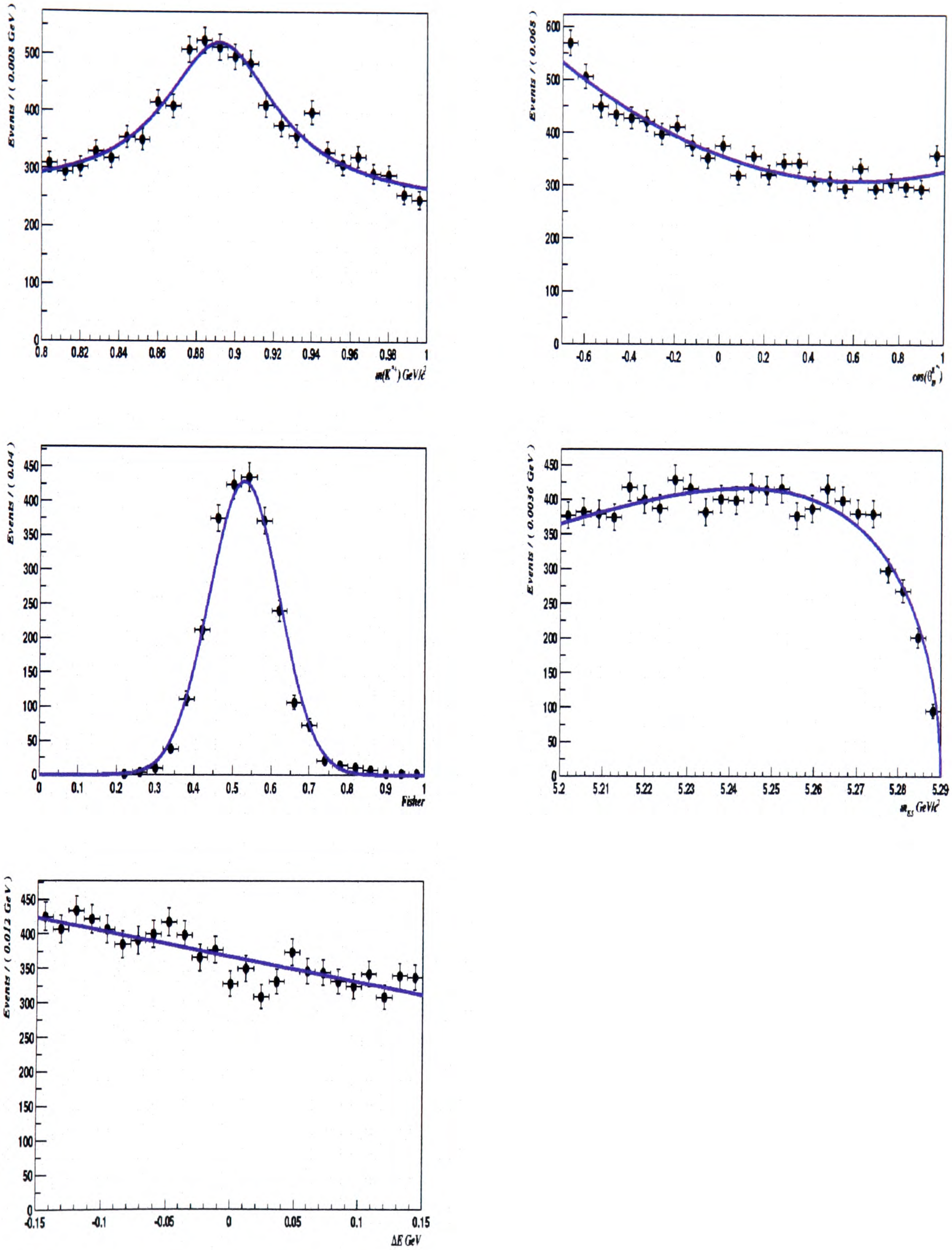

Figure 5.5: Parameterisations of the maximum likelihood fit variables for Monte Carlo continuum $q\bar{q}$ background in the $B^0 \to K^{*+}\pi^-$ analysis.

Mode	N reco (140.5 fb^{-1})	N expected (81 fb^{-1})
$B\bar{B}$, $5.270 < m_{ES} < 5.288$ GeV/c^2		
B^+B^-	9	5.1
$B^0\bar{B}^0$	12	6.3
$B\bar{B}$, $5.2 < m_{ES} < 5.29$ GeV/c^2		
B^+B^-	70	40.5
$B^0\bar{B}^0$	32	15.3

Table 5.7: Reconstructed $B\bar{B}$ events in 140.5 fb^{-1} and expected number of events in 81 fb^{-1}.

generated $B\bar{B}$ Monte Carlo. From both figure 5.6 and table 5.7 the background from B decays is seen to be structureless and small compared to continuum background where we expect ≈ 2100 events for 81 fb^{-1}.

5.5.1 Charmless B backgrounds

To identify potential backgrounds due to rare B modes, a large sample of events has been generated consisting of a variety of $B\bar{B}$ decay modes where one of the B decays is forced to decay to a mode containing no charm particles (*Charmless Cocktail*). We use the charmless sample as a starting point to investigate the structure of the rare B backgrounds. In particular, we are interested in those modes which have final states similar or identical to the signal mode $B^0 \to K^{*+}\pi^-$, $K^{*+} \to K^+\pi^0$. Such B decay modes could be mis-reconstructed as signal and we must be able to understand at what level they are suppressed or distinguishable from signal. The most powerful discriminating variable used in the likelihood fit is the m_{ES} variable which for signal $B^0 \to K^{*+}\pi^-$ extends from $5.270 < m_{ES} < 5.288$ GeV/c^2. Events which have a value of m_{ES} outside of this range have a very small probability to be reconstructed as signal. Therefore, we ask that in addition to satisfying our selection criteria in section 5.3 events from the charmless cocktail sample also reconstruct in the m_{ES} signal region. Figure 5.7 shows the m_{ES} and ΔE distributions in charmless $B\bar{B}$ Monte Carlo. In table 5.8 we give those B decay modes which are reconstructed in the m_{ES} signal region from the

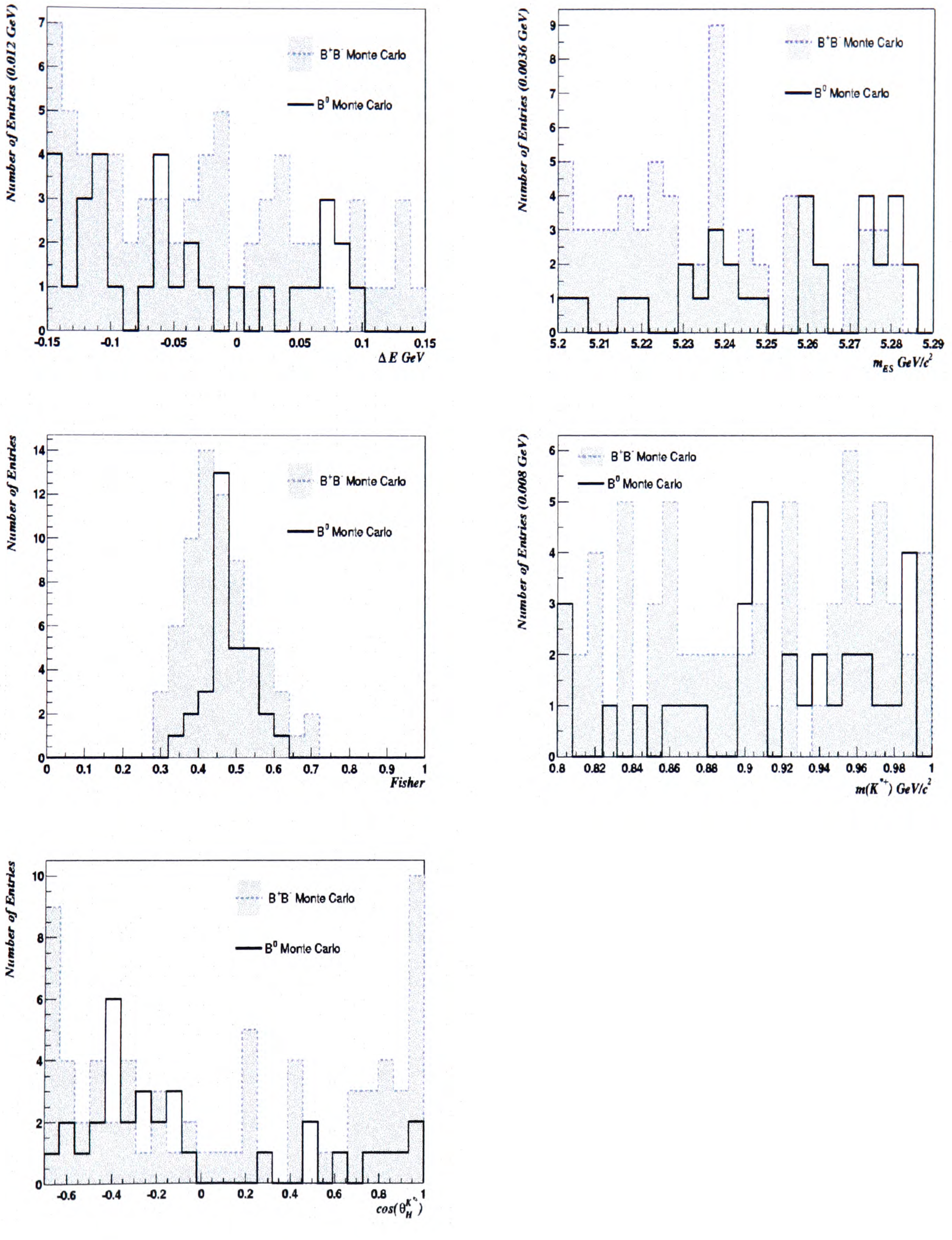

Figure 5.6: The ΔE, $\cos(\theta_H^{K^{*+}})$, $m(K^{*+})$, m_{ES}, $\mathcal{F}$ variables in B^+B^- Monte Carlo and $B^0\bar{B}^0$ Monte Carlo. The distributions are obtained after the event selection in section 5.3.

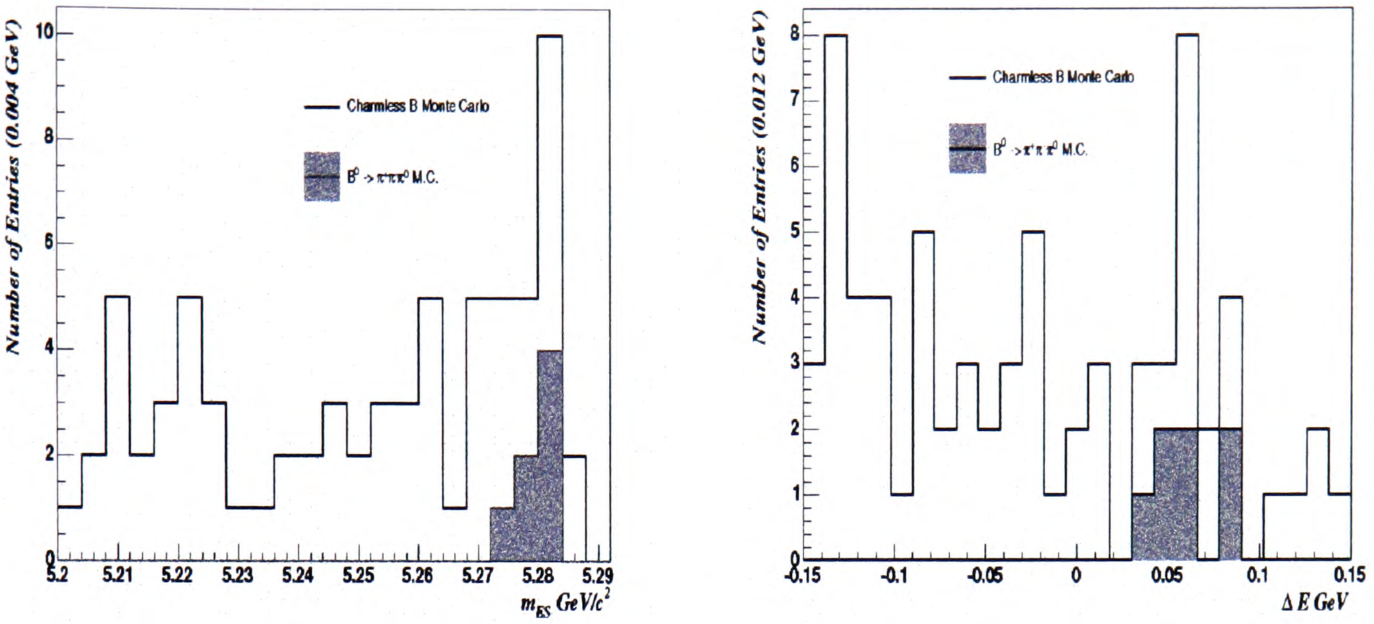

Figure 5.7: m_{ES} and ΔE distributions in charmless $B\bar{B}$ Monte Carlo.

charmless cocktail sample. If the modes have been observed we quote the branching fraction results of the Heavy Flavours Averaging Group [24]. We see that the m_{ES} distribution in the charmless B background has both a combinatoric component and a signal-like Gaussian component which from table 5.8 is dominated by the non-resonant $B^0 \to \pi^+\pi^-\pi^0$ mode.

Given the size of the rare charmless B sample, modes contributing only one event are not expected to enter the signal region for $81\,fb^{-1}$. Instead they are treated as contributions to the combinatorial component of the $B\bar{B}$ background. For the modes where more than one event is observed, a large statistics sample of Monte Carlo is generated to study each mode further. From these larger samples we can better determine the reconstruction efficiencies. From table 5.8 we identify the modes $B^0 \to \pi^+\pi^-\pi^0$, $B^+ \to \rho^+\pi^+\pi^-$ and $B^0 \to K^+\pi^-K^0$ for further study. We may have expected that the charmless four-body modes $B \to \phi K^*$, $B \to \rho K^*, B \to K^*K^*$, $B \to \rho\rho$ would enter as background modes. They are included in the charmless cocktail samples and we see no events from these decays. We find that these modes have final states consisting of four or more particles and are shifted in the ΔE variable by at least the mass of the lost particle, typically a pion. Thus, our ΔE cut of $150\,\mathrm{MeV}/c^2$ will suppress these backgrounds.

Mode	$\mathcal{BR}(10^{-6})$ Generated	$\mathcal{BR}(10^{-6})$ Measured	N reco
Peak charmless $B\bar{B}$, $5.270 < m_{ES} < 5.288$ GeV/c^2			
$B^0 \rightarrow \pi^+\pi^-\pi^0$	30	-	7
$B^0 \rightarrow K^{*0}\pi^+\pi^-$	1.0	-	1
$B^0 \rightarrow \rho^-\pi^+\pi^0$	1.0	-	1
$B^0 \rightarrow K^+\pi^-\omega^0$	1.0	-	1
$B^0 \rightarrow a^{1+}\pi^-$	10	-	1
$B^0 \rightarrow K^{*+}\rho^-$	1.0	-	1
$B^+ \rightarrow \rho^+\pi^+\pi^-$	1.0	-	2
$B^+ \rightarrow K^{*+}\pi^-\pi^+$	1.0	-	1
$B^+ \rightarrow \pi^+\pi^0\omega^0$	1.0	-	1
$B^+ \rightarrow K^{*+}K^+\pi^-$	1.0	-	1
$B^+ \rightarrow K^+K^-\pi^+$	1.0	-	1
$B^0 \rightarrow K^+\pi^-K^0$(N.R.)	1.0	< 2.97	3
$B^0 \rightarrow K^+K^-\pi^0$	1.0	< 19	1
$B^+ \rightarrow K^{*+}\gamma$	40.3	40.3 ± 2.5	1
$B^+ \rightarrow K^+\pi^+\pi^-$	1.0	$< 17 \pm 3.5$	1

Table 5.8: Contributing charmless B background modes for the m_{ES} region $5.270 < m_{ES} < 5.288$ GeV/c^2 determined from charmless $B\bar{B}$ Monte Carlo. The charmless sample corresponds to an integrated luminosity of $\approx 10000\,fb^{-1}$.

The mode $B^0 \to \pi^+\rho^-$ is one of the larger sources of the B background. It contributes when one of the charged pions is mis-identified as a kaon. This background is slightly shifted in ΔE due to the mass difference of the kaon and pion. From table 5.9 we expect $1.43 \pm 0.16 \pm 0.14$ events to enter the fit region.

In reconstructing $B^0 \to K^{*+}\pi^-$, $K^{*+} \to K^+\pi^0$ there are several other modes which can have the same final state. We consider in more detail the modes $B^0 \to K^{*0}\pi^0$, $B^0 \to \rho^-K^+$, $B^0 \to K^+\pi^-\pi^0$ (N.R.), $B^0 \to \bar{D}^0\pi^0$ and the higher kaon resonance decays $B^0 \to K^*(1410, 1430, 1680)\pi$.

When the kaon is fast in $K^{*+} \to K^+\pi^0$, then $B^0 \to \rho^-K^+$ and $B^0 \to K^{*+}\pi^-$ overlap in the Dalitz plane $m^2(K^+\pi^-)$ versus $m^2(K^+\pi^0)$. Since we require that the K^{*+} helicity $\cos(\theta_H^{K^{*+}}) > -0.7$ then most of the contribution from $B^0 \to \rho^-K^+$ will be removed. From table 5.9 we estimate $0.59^{+0.14}_{-0.13} \pm 0.11$ events.

The non-resonant (N.R.) decay $B^0 \to K^+\pi^-\pi^0$ has the same final state as $B^0 \to K^{*+}\pi^-$, $K^{*+} \to K^+\pi^0$. Contamination from non-resonant $B^0 \to K^+\pi^-\pi^0$ events is greatly reduced by the requirement that $0.8 < m(K^{*+}) < 1.0\,\mathrm{GeV/c^2}$. For non-resonant $B^0 \to K^+\pi^-\pi^0$ from table 5.9 we expect $1.64^{+0.79+0.14}_{-0.73-0.11}$

The modes $B^0 \to K^{*0}\pi^0$ and $B^0 \to \bar{D}^0\pi^0$ are rejected by our K^* selection cut $0.8 < m(K^{*+}) < 1.0\,\mathrm{GeV/c^2}$. This occurs because the $m(K^+\pi^-)$ combination in the Dalitz plane is always greater than $1\,\mathrm{GeV}/c^2$.

Higher kaon resonances due to their large widths may also introduce a source of $B\bar{B}$ background. The $B^0 \to K^*\pi$ modes involving higher resonances are identical to the signal channel and are therefore very difficult to remove. We consider the following modes $B^0 \to K^{*+}(1410)\pi^-$, $B^0 \to K_0^{*+}(1430)\pi^-$, $B^0 \to K_2^{*+}(1430)\pi^-$ and $B^0 \to K^{*+}(1680)\pi^-$. In the following analysis we take all K^* parameters and decay channel branching fractions from the 2002 Particle Data Group [15]. If we assume that the higher kaon resonances can be described by Breit Wigner line shapes our selection on $0.8 < m(K^*(892)) < 1.0\,\mathrm{GeV}/c^2$ suppresses a large fraction of any contribution from the higher kaon resonances. The only higher K^* resonances where K^{*+} decays to $K^+\pi^0$ in an $L = 1$ state are those with odd parity. The closest odd-parity K^* resonance to the $K^*(892)$ is the $K^*(1410)$ which has a width of $232\,\mathrm{MeV}/c^2$. The $K^*(1410)$ resonance decays as $K^*(1410) \to K\pi = 6.6 \pm 1.3\%$ while $K^*(1410) \to K^*\pi \approx 40\%$.

This implies that a large fraction of any $K^*(1410)$ background contributes as four-body B background and will be shifted in ΔE. Including isospin only 2.2% of $B \to K^{*+}(1410)\pi^-$ could possibly be reconstructed in the final state $K^+\pi^-\pi^0$. Therefore we would expect to be insensitive to $B \to K^{*+}(1410)\pi^-$ with final state $K^+\pi^-\pi^0$. The next vector resonance above the $K^*(1410)$ is the $K^*(1680)$ resonance. Its width is $322\,\mathrm{MeV}/c^2$ and it decays $K^{*+}(1680) \to K^+\pi^0 = 12.8 \pm 2.5\%$. Again we would not expect much of this background to contribute. The higher kaon resonance $K_0^*(1430)$ is a pseudoscaler particle and has a width of $294\,\mathrm{MeV}/c^2$ where $K_0^{*+}(1430) \to K^+\pi^0 = 31 \pm 10\%$. This mode constitutes the dominant source of background from the higher kaon resonances. Since $K_0^*(1430)$ is a pseudoscaler its helicity distribution is flat. Thus we would expect most of the background from $K^*(1430)$ to be distinguishable from signal since the $K^*(892)$ helicity distribution follows a $\cos^2\theta$ distribution. The $K_2^*(1430)$ which has a much narrower width $\Gamma \approx 100\,\mathrm{MeV}/c^2$, is suppressed primarily by the mass cut on $m(K^{*+}(892))$.

From the analysis above any contamination from the higher kaon resonances is likely to make up a continuum component similar to the non-resonant $B^0 \to K^+\pi^-\pi^0$ channel. An inclusive branching fraction for $B^0 \to K_x^{*+}\pi^-$, $K_x^{*+} \to K^+\pi^0$ has been measured by the BELLE experiment [32]. The notation K_x^* denotes higher kaon resonances in the region $1.1 < m(K^+\pi^0) < 1.6\,\mathrm{GeV}/c^2$. BELLE measures the branching fraction as $\mathcal{BR}(B^0 \to K_x^{*+}\pi^-) = 5.1 \pm 1.5^{+0.6}_{-0.7} \times 10^{-6}$. We may use this result to estimate the number of events from modes involving higher kaon resonance. Using the efficiency for non-resonant $B^0 \to K^+\pi^-\pi^0$ given in table 5.9 we expect $1.47 \pm 0.45^{+0.17}_{-0.20}$ events. Possible interference effects where the higher K^* resonances interfere with the $B^0 \to K^{*+}\pi^-$ amplitude are neglected in this analysis. Interference effects must be determined from a complete analysis in the Dalitz plot, fitting for each amplitude contribution and are beyond the scope of this analysis. Table 5.9 gives the number of expected events for the charmless sources of B background which we have considered. For modes where no events satisfy the selection criteria we give the efficiency determined for one event which provides an upper limit on the efficiency. For modes where only an upper limit on the branching fraction exists we take the central value of the expected number of events and assign a 100% systematic error.

Mode	$\mathcal{BR}(10^{-6})$	Eff (10^{-4})	#Gen	# Exp 81 fb^{-1}
$B^0 \to \rho^+\pi^-$	$22.6 \pm 1.8 \pm 2.2$ [52]	7.31	245K	$1.43 \pm 0.16 \pm 0.14$
$B^0 \to \rho^-K^+$	$7.3^{+1.3}_{-1.2} \pm 1.3$ [52]	9.20	50K	$0.59^{+0.14}_{-0.13} \pm 0.11$
$B^0 \to K^+\pi^-\pi^0$(N.R.)	$5.7^{+2.7+0.5}_{-2.5-0.4}$ [32]	0.32	42K	$1.64^{+0.79+0.14}_{-0.73-0.11}$
$B^0 \to K_x^{*+}\pi^-$	$5.1 \pm 1.5^{+0.6}_{-0.7}$ [32]	0.32	-	$1.47 \pm 0.45^{+0.17}_{-0.20}$
$B^0 \to \pi^+\pi^-\pi^0$(N.R.)	< 30.0 [24]	1.48	27K	0.20 ± 0.20
$B^0 \to \bar{D}^0\pi^0$	11.02 ± 0.5 [15]	< 0.43	23K	0.0
$B^0 \to K^{*0}\pi^0$	< 3.5 [32]	< 0.08	120K	0.0
$B^0 \to K^+\pi^-K_s$(N.R.)	< 2.97 [24]	< 0.20	50K	0.0
$B^+ \to \rho^+\pi^+\pi^-$	1.0	< 0.20	50K	0.0
Total				$5.34 \pm 0.93 \pm 0.36$

Table 5.9: Main expected sources of signal-like crossfeed $B\bar{B}$ backgrounds for the $B^0 \to K^{*+}\pi^-$ analysis. The number of events given corresponds to the full fit region.

5.5.2 Summary of $B\bar{B}$ backgrounds

There are two components for the $B\bar{B}$ background. A combinatoric component where we expect 55 events for a sample of 81 fb^{-1}. This background is expected to be handled by the continuum background PDF models. This is studied in section 5.6.1. In addition, there is a charmless crossfeed component where B events closely resemble the signal mode $B^0 \to K^{*+}\pi^-$. These events will be reconstructed as signal in the maximum likelihood fit. From table 5.9 we expect $5.34 \pm 0.93 \pm 0.36$ events. In section 5.6.1 we perform studies to determine how many of these crossfeed B events are reconstructed as signal using the additional information in the fit. From these studies we can determine the number to subtract from the fitted signal yield. For the remainder of the analysis we reserve the term crossfeed for the charmless background resulting from $B^0 \to K^+\pi^-\pi^0$ (N.R.), higher kaon resonance modes and $B^0 \to \rho^+\pi^-$.

5.6 Validation of fit method

This section discusses the techniques used to validate the maximum likelihood fit method. The primary aim is to verify the signal and background PDF models defined in section 5.4.

We choose to float a number of the background PDF parameters in the maximum likelihood fit. The floating of the background serves two purposes. It eliminates the need to include systematic errors on the background model parameters as they are not determined from Monte Carlo. Secondly, it includes the small $B\bar{B}$ component which is largely combinatorial. Monte Carlo validation studies are performed in section 5.6.1 to determine if the fit is stable while allowing the background to float. We allow the following parameters to float within the maximum likelihood fit:

- **Number of reconstructed events.**

  N_{sig}: Number of reconstructed $B^0 \to K^{*+}\pi^-$.

  $N_{q\bar{q}}$: Number of reconstructed continuum background.

- **Continuum parameters**

  ξ: The m_{ES} ARGUS shape parameter.

  c_1: The linear coefficient of ΔE.

  $\mu(\mathcal{F})$: The mean of the continuum $\mathcal{F}$ distribution.

  $\sigma(\mathcal{F})$: The width of the continuum $\mathcal{F}$ distribution.

  $\mathrm{Frac}_{K^{*+}}$: The fraction of the K^{*+} component.

  $c_1(K^{*+})$: The linear coefficient of the continuum K^{*+} distribution.

  $c_1(\cos(\theta_H^{K^{*+}})$: The linear coefficient of the $\cos(\theta_H^{K^{*+}})$ distribution.

  $c_2(\cos(\theta_H^{K^{*+}})$: The quadratic coefficient of the $\cos(\theta_H^{K^{*+}})$ distribution.

5.6.1 Fit validation method

For each of the yields and background parameters determined in the fit, tests must be performed to determine whether their estimators are unbiased. To this end, we perform a large number of independent experiments where for each experiment a Monte Carlo sample of signal and continuum events is constructed. We use samples of Monte Carlo consisting of events generated from the PDF models defined in section 5.4. Such samples are called 'Toy' Monte Carlo. We also use samples of Monte Carlo where the full detector simulation is employed. The advantage of using 'Full' Monte Carlo is that it includes all the correlations between the fit variables. For each experiment the full extended maximum likelihood fit is performed where we fit the yields and background parameters. The number of generated events N per experiment is randomly selected from a Poisson distribution with mean N. Any potential bias within the fit is studied by forming the 'Pull' distribution defined as:

$$\mathrm{Pull} = \frac{N^j_{\mathrm{Fit}} - N^j_{\mathrm{Gen}}}{\sigma^j_{\mathrm{Fit}}} \tag{5.5}$$

where $N^j_{\mathrm{Fit(Gen)}}$ is the number of events fitted (generated) for each category type j and σ^j_{Fit} is the error on N^j_{Fit} determined from the maximum likelihood fit. If the fit is unbiased then we would expect the pull to be a Gaussian distribution of zero mean and unit width. The signal fit bias is determined as $\frac{\mathrm{Pull}\times\sigma^j_{\mathrm{Fit}}}{N^j_{\mathrm{Gen}}}$. The results of all the following studies are summarised in table 5.10.

5.6.2 Pure toy Monte Carlo studies

The aim of the pure toy studies is to ascertain that we can fit back the correct number of signal and background that we put into the fit. Pure toy Monte Carlo studies consist of 1000 independent experiments where for each experiment a sample of signal and continuum events is generated from the PDFs defined in section 5.4. In generating the continuum events we use the parameters obtained from fully simulated $q\bar{q}$ Monte Carlo. For the signal and background yields we use the values $N_{\mathrm{sig}} = 35$, $N_{\mathrm{bkg}} = 2100$. The pull distribution results are shown in figures 5.8 and 5.9 where we find that the background parameters are bias free. We also conclude that the fit is stable while allowing the background to float. The signal yield N_{sig} has a small bias corresponding to one event which we include in our systematic errors.

5.6.3 Full signal Monte Carlo & toy continuum

In section 5.2 we study the correlations between each of the fit variables where they are found to be small. We now study the effects of any residual correlations between the fit variables which could introduce a bias into the fit. This is achieved by embedding full signal $B^0 \to K^{*+}\pi^-$ Monte Carlo events where the correlations between the fit

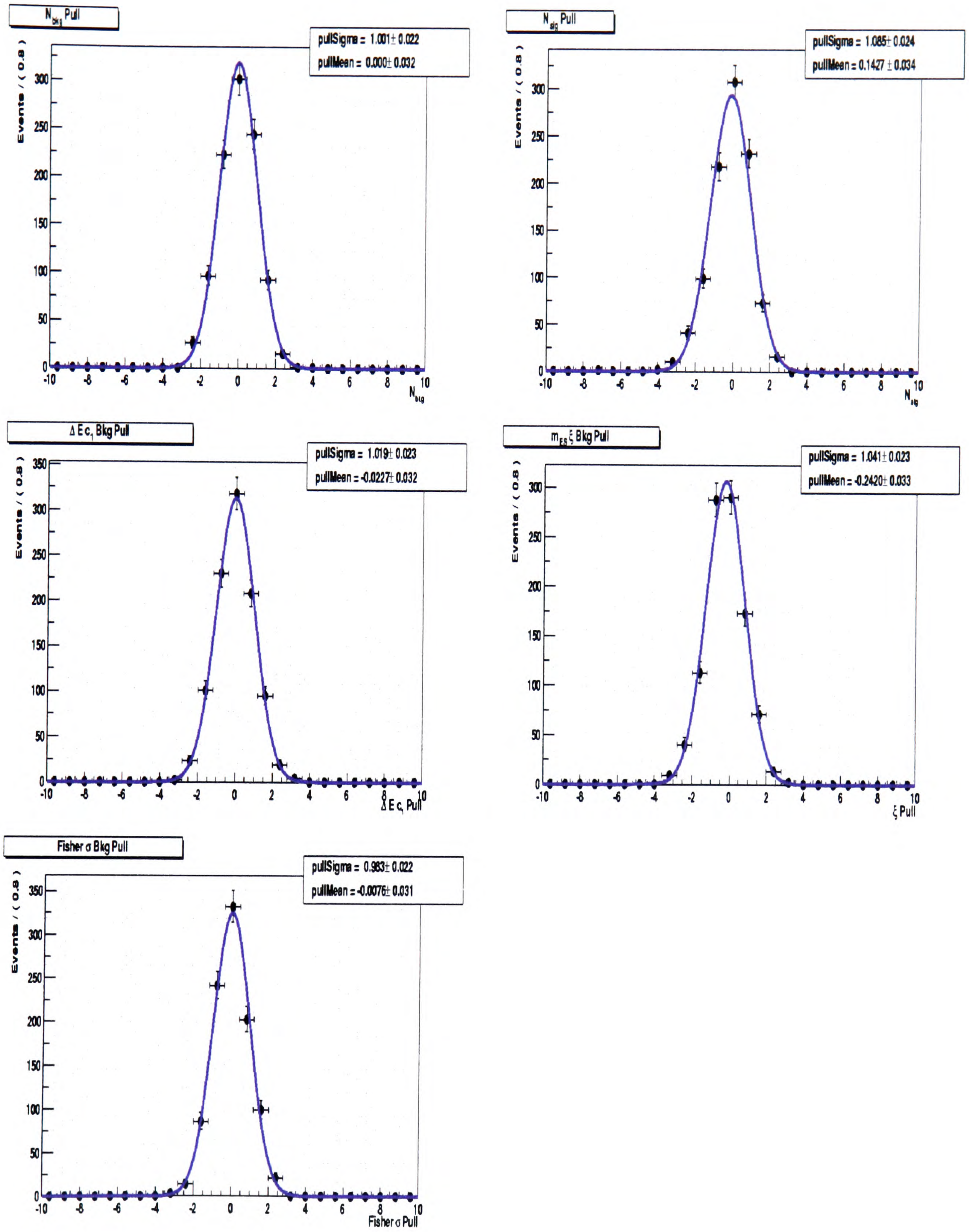

Figure 5.8: Pure toy Monte Carlo results showing the pull distributions of the yields and floated parameters for the $B^0 \to K^{*+}\pi^-$ analysis.

Figure 5.9: Further pure toy Monte Carlo results showing the pull distributions of the yields and floated parameters.

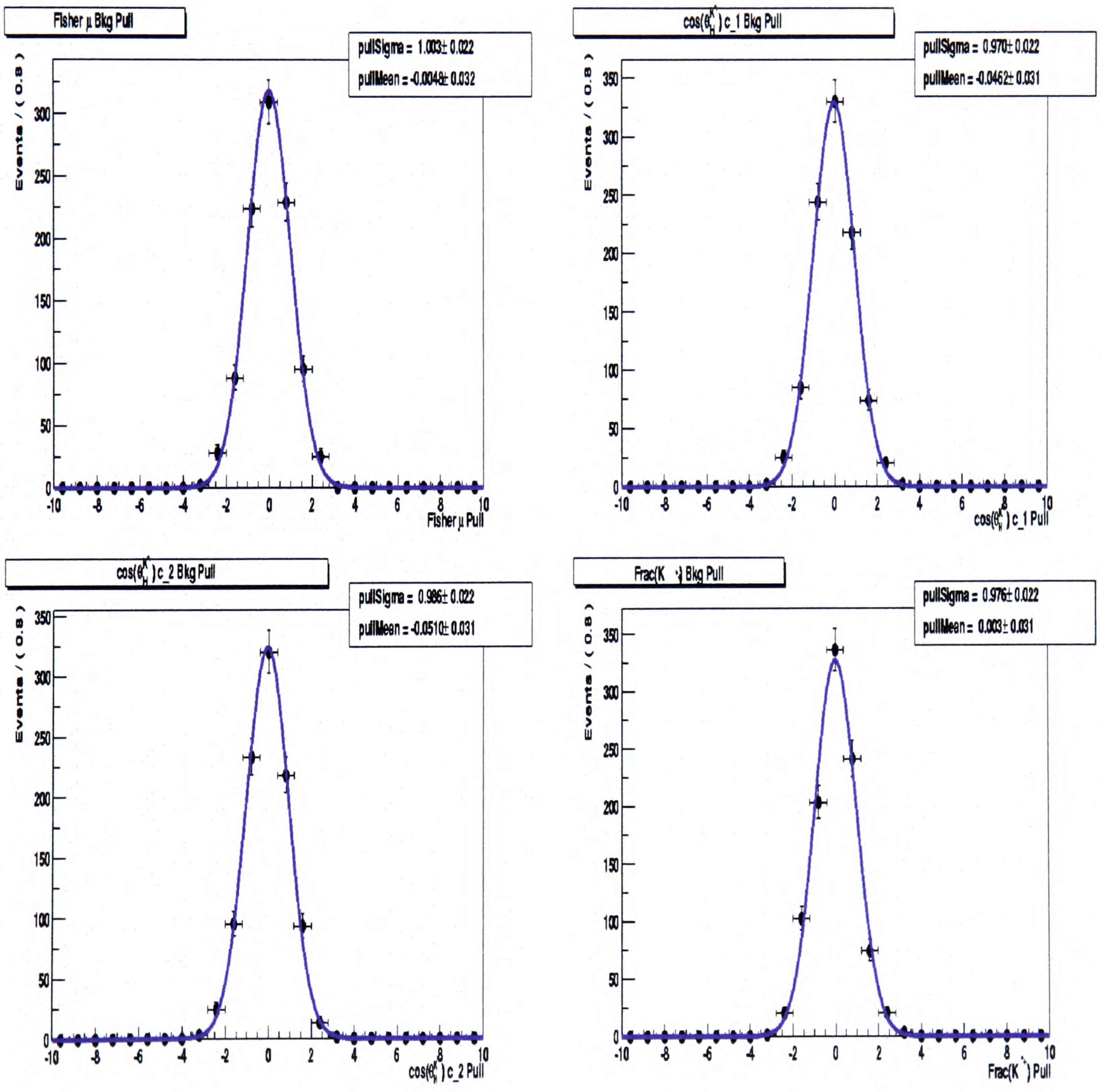

variables are fully simulated, into a sample of toy continuum Monte Carlo events. For each experiment, events are randomly selected from full signal Monte Carlo passing the selection cuts detailed in section 5.3. The signal pull distribution is shown in figure 5.10 (left plot) for 500 experiments with $N_{\text{sig}} = 35$, $N_{\text{bkg}} = 2100$. Comparing the result with that of the pure toy study we conclude that our PDF model sufficiently represents our signal channel.

5.6.4 $B\bar{B}$ Background: combinatoric & crossfeed

The expected background contributions from $B\bar{B}$ are found to consist of a small combinatoric component and a small number of the dominant charmless B modes $B^0 \to K^+\pi^-\pi^0$ and $B^0 \to \rho^+\pi^-$ (section 5.5). To determine how well $B\bar{B}$ is handled we perform a similar study as in section 5.6.3 where 55 full Monte Carlo $B\bar{B}$ events are added to 35 signal and 2045 continuum toy events. We do not include any $B^0 \to K^+\pi^-\pi^0$ or $B^0 \to \rho^+\pi^-$ events. For each experiment, events are randomly selected from a sample of generic $B\bar{B}$ Monte Carlo passing the selection cuts detailed in section 5.3. Figure 5.10 (right plot) shows the signal pull distribution for 500 experiments where we observe no significant difference to the results obtained in section 5.6.3. We may thus conclude that at the level of sensitivity required, most of the $B\bar{B}$ background is handled by the continuum background model described in section 5.4.

We now study the sensitivity of the signal model to the B decay modes $B^0 \to K^+\pi^-\pi^0$ and $B^0 \to \rho^+\pi^-$ which have similar characteristics to the signal mode $B^0 \to K^{*+}\pi^-$. A set of 500 experiments is performed in which 60 events of a particular crossfeed channel is embedded within Monte Carlo samples of toy continuum. We use the larger statistics in order to better determine the error of crossfeed reconstruction. For each crossfeed channel we obtain the fit bias for the number of charmless B background reconstructed as signal. The results are presented for 500 experiments in table 5.10. We find that for $B^0 \to K^+\pi^-\pi^0$ the fit crossfeed reconstruction efficiency is $50 \pm 15\%$ and $17 \pm 12\%$ for $B^0 \to \rho^+\pi^-$. Taking these reconstruction efficiencies into account we would expect a total of $2.12 \pm 0.58_{fit} \pm (0.46 \pm 0.14)_{\mathcal{BR}(B\bar{B})}$ charmless background events to be reconstructed as signal. In deriving this result we take 50% of the expected $\rho^-K^+, K^+\pi^-\pi^0$ and $K_x^{*+}\pi^-$ events and we take 17% of the expected $\pi^+\pi^-\pi^0$

Figure 5.10: Monte Carlo studies showing the $B^0 \to K^{*+}\pi^-$ signal pull distributions for 500 experiments. Left: Embedded signal Monte Carlo and continuum toy events. Right: Embedded signal Monte Carlo, combinatoric $B\bar{B}$ Monte Carlo and continuum toy events.

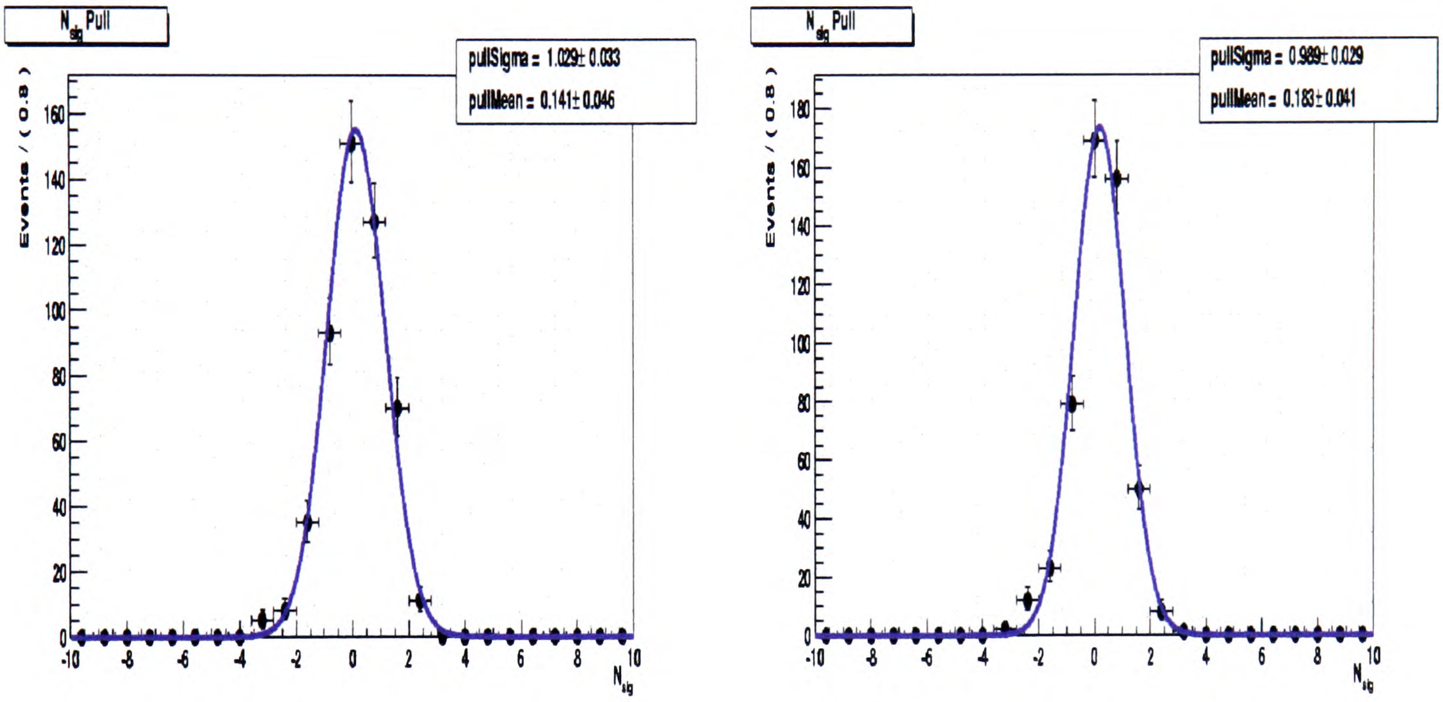

and $\rho^+\pi^-$ events. The first error is the fit efficiency error and the second and third errors are from the errors on the B mode branching fractions.

We do not include a specific component for the crossfeed modes as they are found to be very similar to the signal model. Since we can not float the crossfeed component normalisation, the dominant error on the number of crossfeed events that goes into the fit will depend on the uncertainty on the branching fraction for each background mode. Thus, since the dominant crossfeed components are so similar to the signal mode we choose to subtract the expected number of the crossfeed background from the fitted signal yield.

5.6.5 Comparisons of $-\log\mathcal{L}_{\text{max}}$

Validation of the fit in the form of comparisons of the value of $-\log\mathcal{L}_{\text{max}}$ can also be conducted before the results themselves are determined. To do this the fit is performed on the final data set but only the value of $-\log\mathcal{L}_{\text{max}}$ is observed and not the parameters.

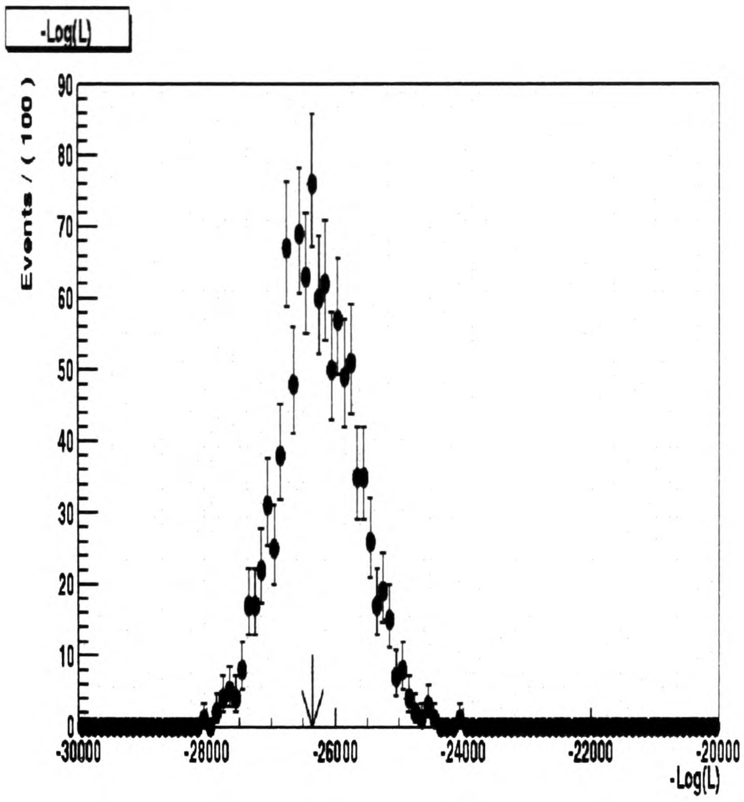

Figure 5.11: Figure showing the distribution of $-\log \mathcal{L}$ and the value obtained from data. The figure indicates that the assumed background model agrees well with data.

The distribution of $-\log \mathcal{L}_{\mathrm{max}}$ from the pure toy Monte Carlo experiments is compared to the value of $-\log \mathcal{L}_{\mathrm{max}}$ obtained on data. Agreement of the values of $-\log \mathcal{L}_{\mathrm{max}}$ provides a good indication that the forms of the background PDFs represent the data well. From figure 5.11 we see that the assumed background model agrees well with the data value of $-\log \mathcal{L}_{\mathrm{max}} = -26368$.

5.7 Comparisons of data and Monte Carlo

To determine how well the continuum $q\bar{q}$ Monte Carlo describes data $q\bar{q}$ events we can make a comparison with off-peak data. However, for off-peak data, there are limited statistics available and we would like to take advantage of the larger statistics in the on-peak sample. In order to make a comparison between on-peak data and continuum Monte Carlo we must select data in a region where $B\bar{B}$ background contamination is minimal and which does not include the signal region. Figure 5.12 shows the distribution of ΔE and m_{ES} in 140.5 fb^{-1} $B\bar{B}$ Monte Carlo. We apply all selections given in section 5.3 with the exception of $|\cos(\theta^{B}_{\mathrm{sph}})|$ and ΔE. For these variables we apply the

N_{total}	$B\bar{B}$ Input	$N_{K^{*+}\pi^-}$ Input	$\mu(N_{\text{sig}})$ fit	$\mu(N_{q\bar{q}})$ fit	μ(Bias)	$\mu(-\log \mathcal{L}_{\text{max}})$
I: Pure toy Monte Carlo.						
2135	0.0	35	36.2 ± 8.4	2098.8 ± 45	0.03	-26250
II: Embedded Monte Carlo signal and toy continuum.						
2135	0.0	35	36.2 ± 8.5	2098.8 ± 45	0.03	-26600
III: Embedded Monte Carlo signal, Monte Carlo $B\bar{B}$ and toy continuum.						
2135	55.0	35	36.6 ± 8.6	2098.4 ± 45	0.04	-26550
IV: $B^0 \to K^+\pi^-\pi^0$ and toy continuum.						
2160	60.0	0.0	30.0 ± 9.0	2130 ± 45	0.53	-
IV: $B^0 \to \rho^+\pi^-$ and toy continuum.						
2160	60.0	0.0	10.0 ± 7.0	2150 ± 45	0.16	-

Table 5.10: Fit results. 500 Experiments each. I: Pure toy, II: Embedded signal Monte Carlo and toy continuum, III: Embedded Monte Carlo signal, $B\bar{B}$ Monte Carlo and toy continuum, IV: Embedded signal-like crossfeed $B\bar{B}$ Monte Carlo and toy continuum.

looser selections $|\cos(\theta^{B}_{\rm sph})| < 0.9$ and $|\Delta E| < 0.4\,\mathrm{GeV}$. The loosening of the $|\cos(\theta^{B}_{\rm sph})|$ selection increases the number of $q\bar{q}$ events and the widening of the $|\Delta E|$ selection allows us to determine where the $B\bar{B}$ background is minimal. We see that the region $-0.4 < \Delta E < -0.2\,\mathrm{GeV}$ contains a large amount of $B\bar{B}$ events. Thus, on-peak data for this range can not be used to make a comparison with continuum Monte Carlo. In the region $0.2 < \Delta E < 0.4\,\mathrm{GeV}$ we find that the number of $B\bar{B}$ events is minimal with $B^0\bar{B}^0 = 10$ events and $B^+B^- = 29$ events. For $81\,fb^{-1}$ the total expected number of $B\bar{B}$ events is 22.3. This number is small compared to the 3961 events in on-peak 'side-band' data.

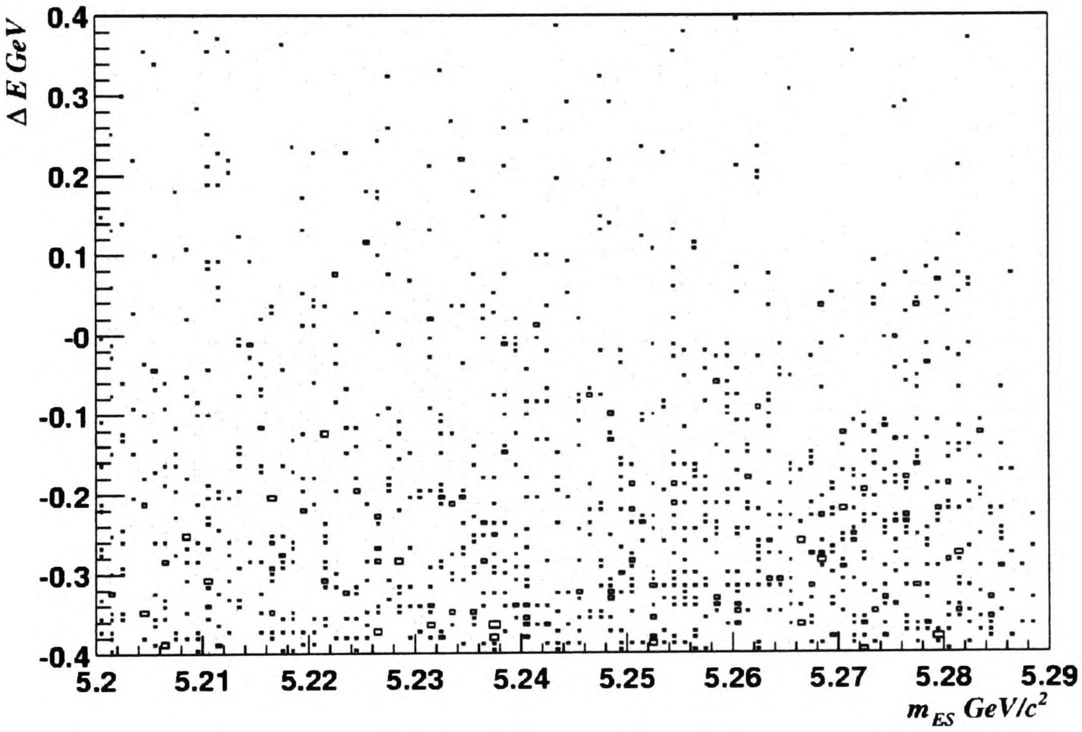

Figure 5.12: $B\bar{B}$ generic Monte Carlo showing the amount of $B\bar{B}$ pollution in the ΔE variable for the $B^0 \to K^{*+}\pi^-$ analysis.

In figure 5.13 we compare off-peak and on-peak data to continuum Monte Carlo in the 'ΔE side-band' region defined as $0.2 < \Delta E < 0.4\,\mathrm{GeV}$. All figures contain events which pass the entire set of selection cuts in section 5.3 apart from the looser restrictions on $\cos(\theta^{B}_{\rm sph})$ and ΔE. We see that Monte Carlo describes the data well and confirms once more that our chosen background shapes (section 5.4) are satisfactory in describing data. Although there are some differences, since the background parameters are determined from the fit this reduces our reliance on the Monte Carlo.

5.8 Fit results

In this section we give the results of the extended maximum likelihood fit to data. As previously described our maximum likelihood function consists of signal and background event categories. For each event category we determine a total PDF consisting of 5 independent fit variables ΔE, m_{ES}, $m(K^*)$, $\cos(\theta_{\mathrm{H}}^{K^*})$, $\mathcal{F}$. The dominant background arises from continuum $q\bar{q}$ events with a small combinatorial background from $B\bar{B}$ events. From the fit we determine the background model parameters and the signal and background yields. In table 5.11 we give the values of all fixed model parameters and also the values of those parameters obtained from the fit. All values of the fixed parameters are the data corrected values and we give the largest error for each parameter. These data corrections are discussed in the systematics section 5.9.5. For those parameters determined from the fit the errors shown are determined using the methods discussed in section 4.8.2.

For the signal $B^0 \to K^{*+}\pi^-$ and background yields we obtain $N_{\mathrm{sig}} = 30.0^{+8.3}_{-7.4}$ and $N_{q\bar{q}} = 2023 \pm 45$. From the fit we determine the correlations for the floating fit parameters and yields which is given in table 5.12 where we find that they are small.

In the Gaussian approximation, the log likelihood distribution is given by $e^{-\chi^2/2}$. The statistical significance on the number of signal events is calculated by taking the difference between the value of $-2\log\mathcal{L}$ obtained in the nominal fit and the value obtained by fixing $N_{\mathrm{sig}} = 0$. The significance of the result is then determined as $\sqrt{-2\log(\mathcal{L}/\mathcal{L}_{\mathrm{S=0}})}$. In figure 5.14 we show the negative log likelihood scan from which a statistical significance of 6.08 is obtained. For the $B^0 \to K^{*+}\pi^-$ analysis we must subtract a crossfeed component from the signal fit yield corresponding to 2.12 events. This reduces our statistical significance from 6.08 to 5.29.

5.8.1 Likelihood ratio & projections

It has become standard to demonstrate the signal excess in each of the fit variables by considering the probability ratio denoted $\mathcal{R}$. The probability ratio is formed by

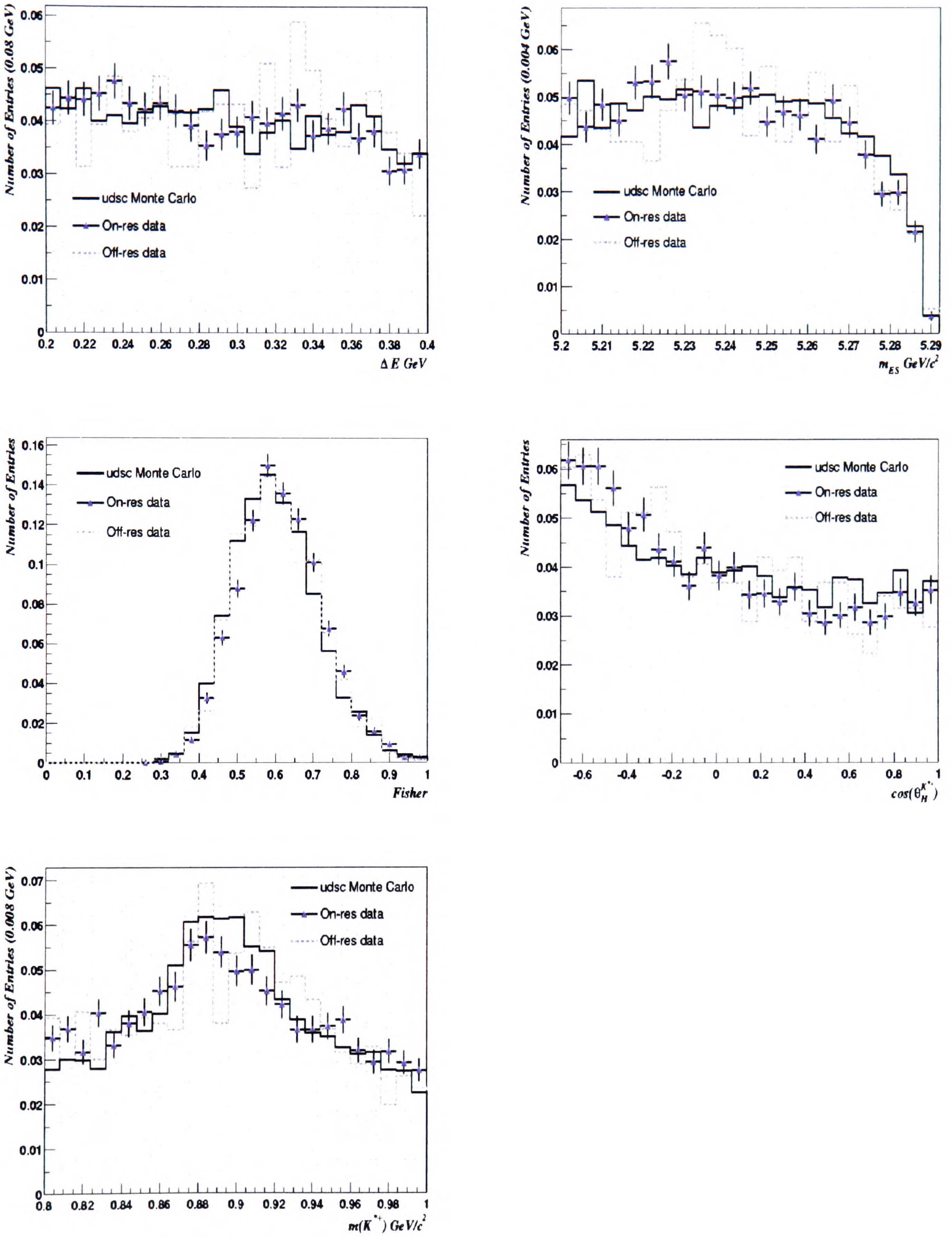

Figure 5.13: udsc Monte Carlo, off-peak and on-peak data comparison for $0.2 < \Delta E < 0.4\,\mathrm{GeV}$. The selection cuts are described in the text of section 5.7.

Parameter	Description	Value
N_{sig}	Number of $B^0 \to K^{*+}\pi^-$	$30.0^{+8.3}_{-7.4}$
$N_{q\bar{q}}$	Number of continuum $q\bar{q}$	2023 ± 45
$B^0 \to K^{*+}\pi^-$ Fit parameters. All parameters fixed.		
$\sigma(m_{ES})$	Resolution of the Crystal Ball for m_{ES} signal MeV/c^2	2.80 ± 0.15
$\mu(m_{ES})$	Mean of the Crystal Ball for m_{ES} signal GeV/c^2	5.280 ± 0.0002
α	m_{ES} C.B parameter	1.715 ± 0.040
n	m_{ES} C.B order parameter	10
$c_1(\Delta E)$	Linear coefficient of ΔE signal	-2.325 ± 0.460
$\mu(\Delta E)$	Mean of Gaussian component of ΔE signal MeV	-3.6 ± 2.5
$\sigma_1(\Delta E)$	Negative ΔE resolution^2 GeV	0.039 ± 0.001
$\sigma_2(\Delta E)$	Positive ΔE resolution GeV	0.027 ± 0.001
$\mathrm{Frac}_{\Delta E}$	Gaussian contribution	0.835 ± 0.010
$\sigma(\mathcal{F})$	Width of Fisher Gaussian	0.437 ± 0.001
$\mu(\mathcal{F})$	Mean of Fisher Gaussian	0.088 ± 0.001
$\Gamma(K^{*+})$	Width of K^{*+} resonance GeV/c^2	0.050 ± 0.005
$\mu(K^{*+})$	Mass of K^{*+} resonance GeV/c^2	0.890 ± 0.002
$c_1(\cos(\theta_H^{K^{*+}}))$	Linear coefficient of the $\cos(\theta_H^{K^{*+}})$ distribution	0.688 ± 0.013
$c_2(\cos(\theta_H^{K^{*+}}))$	Quadratic coefficient of the $\cos(\theta_H^{K^{*+}})$ distribution	0.932 ± 0.005
$q\bar{q}$ background parameters determined from fit.		
ξ	ARGUS $q\bar{q}$ background shape parameter	-21.18 ± 2.53
$c_1(\Delta E)$	ΔE linear coefficient of $q\bar{q}$ background	-0.91 ± 0.25
$\mu(\mathcal{F})$	Mean of background Fisher Gaussian	0.537 ± 0.002
$\sigma(\mathcal{F})$	Left width of background Fisher Gaussian	0.010 ± 0.001
$\sigma(\mathcal{F})$	Right width of background Fisher Gaussian	0.098 ± 0.001
$c_1(K^{*+})$	Linear K^{*+} background component in $q\bar{q}$ background	0.054 ± 0.044
$\mathrm{Frac}_{K^{*+}}$	Contribution of K^{*+} component	0.188 ± 0.016
$c_1(\cos(\theta_H^{K^{*+}}))$	Linear coefficient of the $\cos(\theta_H^{K^{*+}})$ distribution	-0.383 ± 0.036
$c_2(\cos(\theta_H^{K^{*+}}))$	Quadratic coefficient of the $\cos(\theta_H^{K^{*+}})$ distribution	0.223 ± 0.032
$q\bar{q}$ background parameters fixed in fit.		
m_0	Endpoint of ARGUS function	5.29
$\Gamma(K^{*+})$	Width of K^{*+} resonance in background GeV/c^2	0.050 ± 0.005
$\mu(K^{*+})$	Mass of K^{*+} resonance in background GeV/c^2	0.890 ± 0.002

Table 5.11: Values of the fit parameters and signal yield results of the final fit to data.

	$\xi(m_{ES})$	$c_1(\theta_H^{K^{*+}})$	$c_2(\theta_H^{K^{*+}})$	$F_{K^{*+}}$	$c_1(K^{*+})$	$\mu(\mathcal{F})$	$\sigma(\mathcal{F})$	$c_1(\Delta E)$	$N_{q\bar{q}}$	N_{sig}
$\xi(m_{ES})$	1									
$c_1(\theta_H^{K^{*+}})$	-0.009	1								
$c_2(\theta_H^{K^{*+}})$	-0.010	-0.002	1							
$F_{K^{*+}}$	-0.013	0.006	0.004	1						
$c_1(K^{*+})$	0.006	0.001	0.005	0.153	1					
$\mu(\mathcal{F})$	0.011	-0.003	0.001	-0.007	0.000	1				
$\sigma(\mathcal{F})$	0.005	-0.002	0.003	-0.003	0.001	0.005	1			
$c_1(\Delta E)$	0.005	0.001	0.000	-0.001	-0.003	0.003	0.009	1		
$N_{q\bar{q}}$	-0.026	0.003	-0.001	0.009	-0.001	-0.011	-0.001	-0.003	1	
N_{sig}	0.163	-0.029	-0.035	-0.033	0.008	0.060	0.003	0.015	-0.083	1

Table 5.12: Correlation between the yields and floating parameters in the maximum likelihood fit to data.

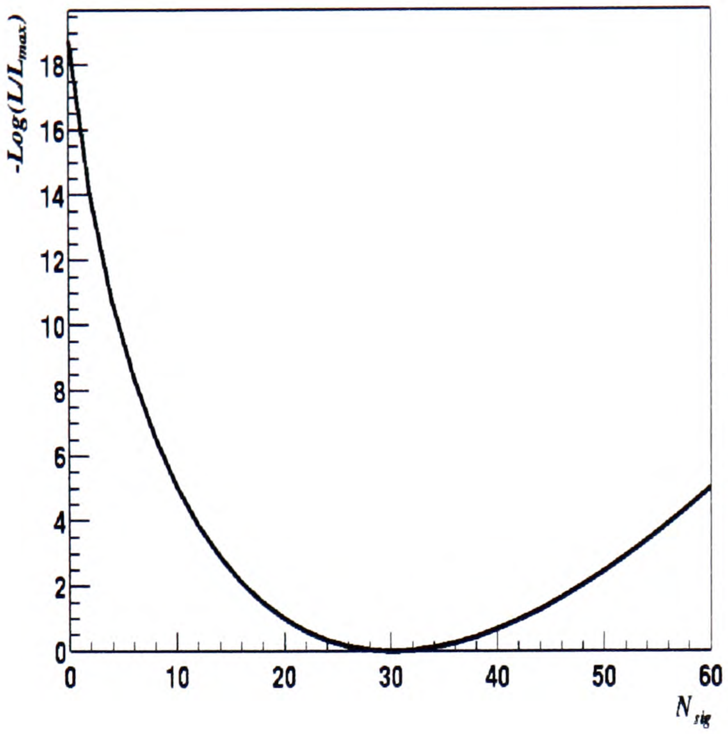

Figure 5.14: $-log(\mathcal{L}/\mathcal{L}_{\max})$ scan for the $B^0 \rightarrow K^{*+}\pi^-$ analysis.

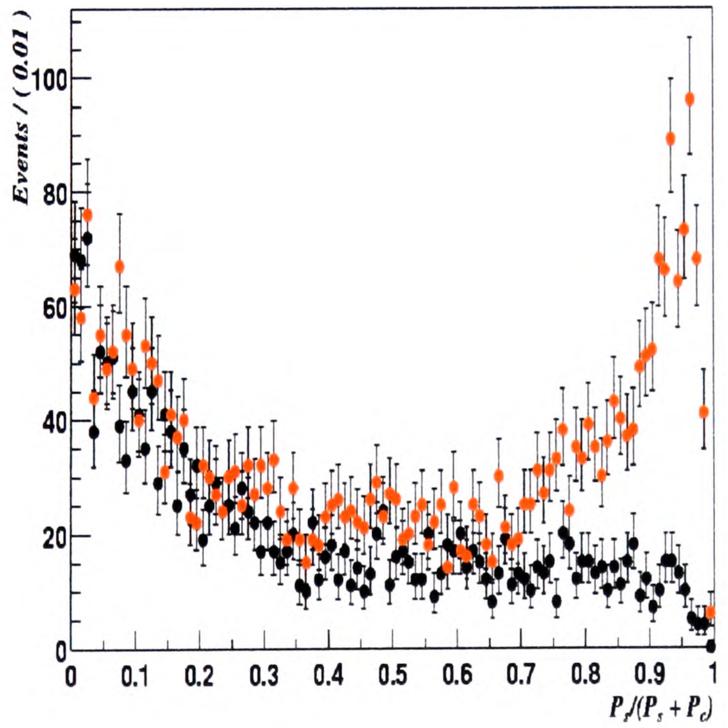

Figure 5.15: Distribution of $\mathcal{R}$ defined in equation 5.6 for data (black) and combined continuum and signal Monte Carlo (red). A cut value of $\mathcal{R} > 0.7$ removes most of the background events.

integrating out the variable which has been chosen as the presentation variable denoted x. The ratio $\mathcal{R}(\vec{z})$ is given by:

$$\mathcal{R}(\vec{z}) = \frac{\int \mathcal{P}^{K^*\pi}(x;\vec{z})dx}{\int(\mathcal{P}^{q\bar{q}}(x;\vec{z}) + \mathcal{P}^{K^*\pi}(x;\vec{z}))dx} \tag{5.6}$$

where $\vec{z}$ corresponds to the other fit variables not including the chosen presentation variable and $\mathcal{P}$ is the combined probability density function described in section 4.8.3. Figure 5.15 shows the distribution (black dots) of $\mathcal{R}$ for data where m_{ES} has been integrated out. Also shown, (red dots) is the $\mathcal{R}$ distribution for a combined sample of 2450 continuum Monte Carlo and 1000 signal Monte Carlo $B^0 \to K^{*+}\pi^-$. The continuum $q\bar{q}$ events occur predominantly at $\mathcal{R} = 0$ whereas signal events occur predominantly at $\mathcal{R} = 1.0$. By considering events where $\mathcal{R} > 0.7$ the majority of $q\bar{q}$ can be suppressed. Projection plots for each of the fit variables, m_{ES}, ΔE, $\mathcal{F}$, $m(K^{*+})$, $\cos(\theta_H^{K^{*+}})$ are determined by integrating over all non-presentation variables after removing those events which fail the $\mathcal{R}$ cut:

$$P(x) = \frac{\int \mathcal{P}(x;\vec{z})d\vec{z}}{\int \mathcal{P}(x;\vec{z})dxd\vec{z}}, \tag{5.7}$$

where x is the projection variable (presentation variable) and $\vec{z}$ is the set of remaining variables which are integrated over. The resulting projection distributions are shown in figure 5.16 where the signal $B^0 \to K^{*+}\pi^-$ events can clearly be seen, particularly in the m_{ES} distribution.

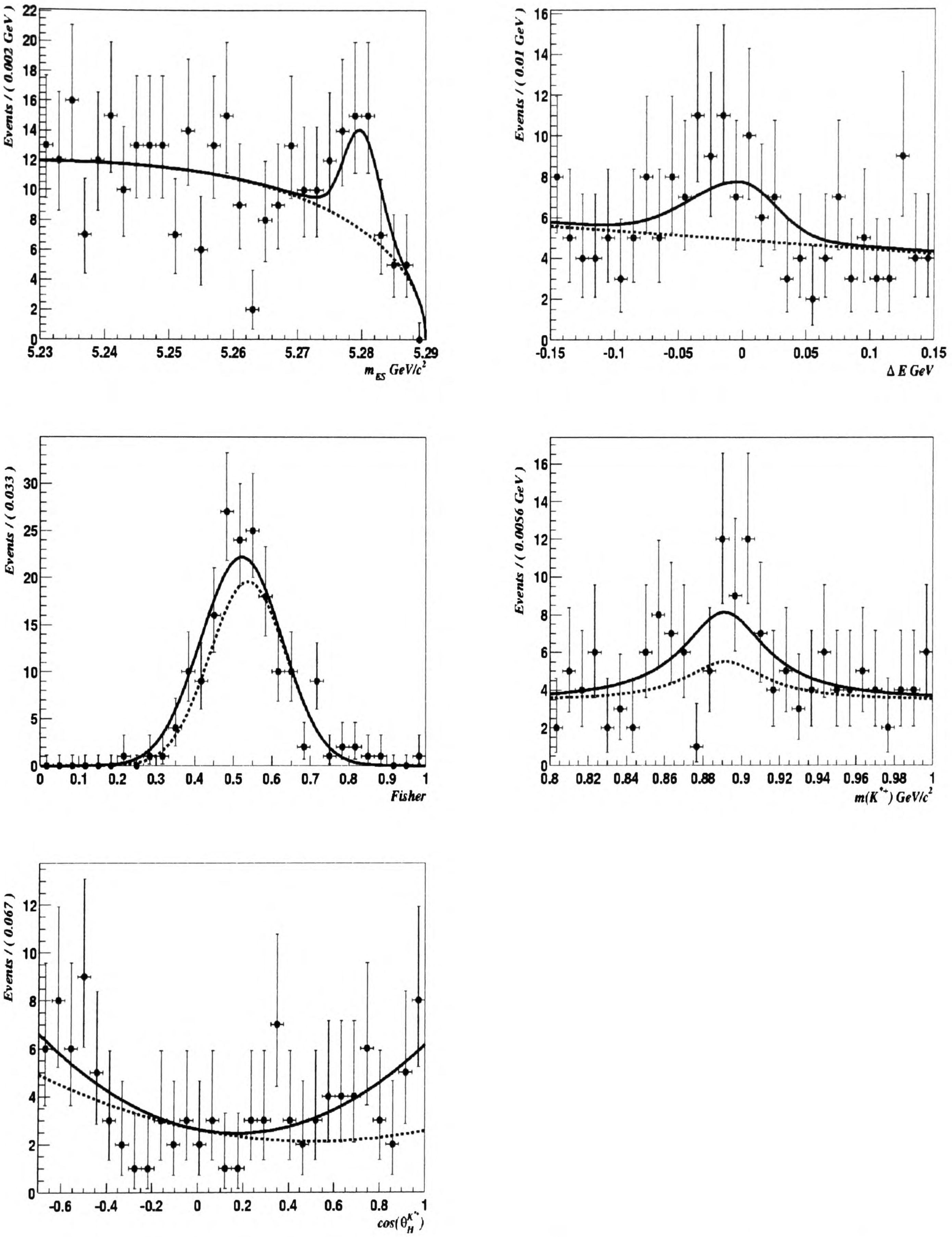

Figure 5.16: Projection plots for the analysis of $B^0 \to K^{*+}\pi^-$ made using the method discussed in section 5.8.1 for data. The projected variables are respectively m_{ES}, ΔE, $\mathcal{F}$, $m(K^{*+})$, $\cos(\theta_H^{K^{*+}})$. The projections shown are: background and signal PDFs (solid line) and background only PDFs (dashed line).

5.9 Systematic errors

This section introduces the main sources of systematic errors for the analysis of $B^0 \to K^{*+}\pi^-$, $K^{*+} \to K^+\pi^0$. Systematic errors arise predominantly from the differences between data and Monte Carlo simulations.

5.9.1 Efficiency systematics

Since Monte Carlo does not accurately model data, the signal efficiency obtained from Monte Carlo must be corrected to account for any differences. For the final state $B^0 \to K^+\pi^-\pi^0$ it is necessary to consider the differences that arise in track reconstruction, particle identification and π^0 reconstruction. In each instance, control samples taken from data are formed which contain large samples of tracks, kaons, and both charged and neutral pions. The specific modes used for control samples vary and are discussed in the following sections. By generating the corresponding Monte Carlo samples, the differences between the two samples can be established. This results in correction recipes which are then used to correct the Monte Carlo signal efficiencies. Typically these corrections are applied as scaling factors (r_i) to the original signal Monte Carlo efficiency(ϵ_{MC}). The total efficiency is then determined as:

$$\epsilon = \epsilon_{\mathrm{MC}} \prod_i r_i. \tag{5.8}$$

For each method used to derive a correction (r_i) there will be an associated systematic error. These are added in quadrature to give the total systematic error on the corrected signal efficiency $\sigma^{\epsilon}_{\mathrm{sys}}$. The following sections describe both the corrections and systematic errors arising due to efficiency corrections.

5.9.2 π^0 corrections

The π^0 efficiency correction to the Monte Carlo is obtained from tagged τ decay modes in $e^+e^- \to \tau^+\tau^-$, where $\tau^- \to e^-\bar{\nu}_e\nu_\tau$ and $\tau^+ \to h^+N\pi^0\nu_\tau$, $h = K,\pi$, $N = 1,2$. The correction is determined using a number of different methods. To correct the π^0 shape in Monte Carlo a photon energy rescaling (0.75%) and energy dependent photon resolution correction (1-3%) must be applied. In order to match the π^0 reconstruction efficiency to data, we must apply an electromagnetic shower killing. The killing factor is obtained by taking the ratio of reconstructed events for data over Monte Carlo. This is done for both the $2\pi^0$ and $1\pi^0$ final states. Figure 5.17 shows both data and uncorrected Monte Carlo for the E_γ and $m(\pi^0)$ distributions after the thrust cut $|\cos(\theta^B_{\mathrm{sph}})| < 0.7$. We see that the main difference in the distributions is that the Monte Carlo slightly underestimates the π^0 width which is corrected for using the photon resolution and energy rescaling corrections. These corrections remove any differences in efficiency for the E_γ and $m(\pi^0)$ selection cuts due to data Monte Carlo differences. We find that the π^0 efficiency correction factor is 0.995. The systematic error on the π^0 correction is 5% per π^0 which includes the following contributions:

- Uncertainty on $\mathcal{BR}(\tau \to h\pi^0\nu)$ $\mathcal{BR}(\tau \to h\pi^0\pi^0\nu)$ (1.6%).
- The difference in the efficiency with and without applying a 2% (photon smearing) resolution correction.
- π^0 reconstruction in hadronic decay channels (1%).
- A (3%) effect when the photons used to reconstruct the neutral pion are from different electromagnetic shower clusters in the EMC.

For further information on the neutral correction method see the references [53] [47].

5.9.3 Tracking efficiency corrections

Track selection corrections are applied to the Monte Carlo which are determined using the methods described in [46]. The principal idea is to use control samples such as $D^{*+} \to D^0\pi^+$, $D^0 \to K^-\pi^+$ and determine the track reconstruction efficiencies for both data and Monte Carlo. The procedure for applying the corrections to Monte Carlo is given in [54], where the tracks satisfy the reconstruction criteria given in section 4.2. For our track selections we apply a flat 0.8% correction per event track which results in a total efficiency correction of 1.6%. The tracking systematic error is determined in [54] to be 3.5% per track.

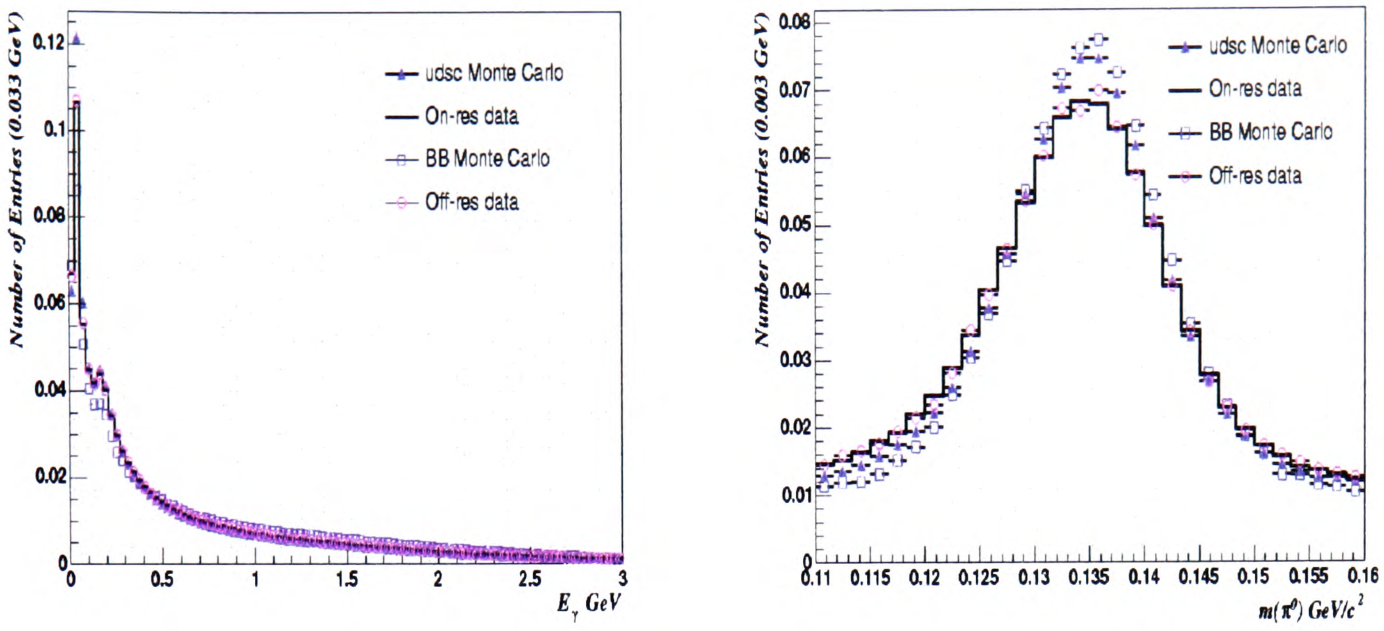

Figure 5.17: $m(\pi^0)$ and E_γ for continuum $q\bar{q}$, ($q = u, d, s, c$) Monte Carlo, off-peak data, on-peak data and $B\bar{B}$ Monte Carlo.

	Data $\epsilon(K)$	Monte Carlo $\epsilon(K)$	Correction
$K^\pm/\pi^\pm$ ID	0.833 ± 0.009	0.812 ± 0.007	0.975 ± 0.013

Table 5.13: K, π selection efficiencies from $D^{*+} \to D^0\pi^+$, $D^0 \to K^-\pi^+$, averaged over $0.250 < |\vec{p}| < 4.0\,\mathrm{GeV/c}$, Run I and Run II data.

5.9.4 Kaon selection efficiency corrections

The selection efficiency(fig. 4.3) for charged kaons and pions is determined as a function of track momentum on data using the control sample $D^{*+} \to D^0\pi^+$, $D^0 \to K^-\pi^+$. These events are selected very cleanly due to the small width of the $D^{*+} - D^0$ difference. The charged tracks satisfy the same criteria set out in section 4.2. In table 5.13 we give the kaon selection efficiencies for data and Monte Carlo for the control sample $D^{*+} \to D^0\pi^+$, $D^0 \to K^-\pi^+$. The correction to Monte Carlo is determined by forming the ratio of the kaon selection efficiencies for data and Monte Carlo. The full procedure is defined in [55].

Applying all systematic correction factors to the uncorrected Monte Carlo signal efficiency we obtain, using equation 5.8, $\epsilon = (11.30 \pm 0.14)\%$, where the error given is statistical.

5.9.5 Model PDF systematics

Systematic errors arise in modeling the probability density functions of the fit variables due to differences between data and Monte Carlo. To study these differences and obtain corrections to the signal PDFs high statistic control modes are chosen which have similar final states and kinematics. For the $K^+\pi^-\pi^0$ final state the modes $B^0 \to \bar{D}^0\pi^0, \bar{D}^0 \to K^+\pi^-$ and $B^+ \to \bar{D}^0\pi^+, \bar{D}^0 \to K^+\pi^-\pi^0$ are possible candidates for control samples. $B^0 \to \bar{D}^0\pi^0$ has the same final state as $B^0 \to K^{*+}\pi^-$ while $B^+ \to \bar{D}^0\pi^+$ has the advantage of having a slower neutral pion. Thus for $B^0 \to K^{*+}\pi^-$ we use the $B^+ \to \bar{D}^0\pi^+$, $\bar{D}^0 \to K^+\pi^-\pi^0$ control sample. The floated $q\bar{q}$ model parameters are determined from data and do not have a systematic error. The resulting prescription for correcting the signal Monte Carlo m_{ES} and ΔE parameters is taken from reference [56].

- $\mu(m_{ES})$ is fixed to 5.280 GeV/c^2 with an error of 0.2 MeV/c^2 determined from $B^0 \to \bar{D}^0\pi^0, \bar{D}^0 \to K^+\pi^-\pi^0$
- $\sigma(m_{ES})$ is fixed to the Monte Carlo value with an error of 0.15 MeV/c^2 determined from $B^0 \to \bar{D}^0\pi^0$, $\bar{D}^0 \to K^+\pi^-\pi^0$
- For Monte Carlo $\mu(\Delta E)$ is shifted by -5.0 MeV and an error of 2.5 MeV is assigned which is determined from $B^+ \to \bar{D}^0\pi^+$, $\bar{D}^0 \to K^+\pi^-\pi^0$
- For $\sigma(\Delta E)$ the Monte Carlo is scaled up by 5% and an error of 5% is assigned from $B^+ \to \bar{D}^0\pi^+$, $\bar{D}^0 \to K^+\pi^-\pi^0$

For the linear discriminant $\mathcal{F}$, we determine corrections to the Gaussian parameters from the control sample $B^+ \to \bar{D}^0\pi^+$, $\bar{D}^0 \to K^+\pi^-\pi^0$. No difference is found within the available statistics.

For both signal and background the $K^{*+}(892)$ line shape is fixed to the PDG value given in section 4.5. In order to test the sensitivity of the fit we vary the Breit-Wigner width within 10% of the $K^*(892)$ PDG value. We observe no significant deviation on the signal yield.

For the $\cos(\theta_H^{K^{*+}})$ distribution we take the difference between the fitted helicity parameters and the expected $\cos^2(\theta_H^{K^{*+}})$ distribution as a systematic error. The error is smaller than the statistical errors on the fitted helicity parameters.

5.9.6 Maximum likelihood fit yield error

The statistical and systematic uncertainties on the M.L. signal yields due to the modelling of the PDFs are determined by varying each model parameter within 1σ of their fitted values while performing the full extended likelihood fit. The dominant errors are the systematic uncertainties discussed in the last section. The resulting change in the nominal yields as determined from the extended likelihood fit is used as the systematic uncertainty due to the parameterisations of the probability density functions. The results are shown in table 5.14, for each discriminating fit variable. To derive the total systematic error we add in quadrature the signal yield N_{sig} variations due to each fit variable. We thus obtain a total systematic error of 0.6 events which is 2% of the nominal fitted yield.

Var	m_{ES}		ΔE		$\cos(\theta_H^{K^{*+}})$		$m(K^{*+})$		$\mathcal{F}$	
$\pm\sigma$	+	-	+	-	+	-	+	-	+	-
$\Delta(N_{\text{sig}})$	−0.103	−0.248	−0.046	−0.315	0.038	−0.324	−0.231	−0.133	−0.041	−0.318
$\Delta(N_{q\bar{q}})$	0.214	0.145	0.141	0.229	−0.002	0.286	0.232	0.136	0.183	0.182
Background										
$\Delta(N_{\text{sig}})$	-	-	-	-	-	-	−0.183	0.203	-	-
$\Delta(N_{q\bar{q}})$	-	-	-	-	-	-	−0.173	0.149	-	-

Table 5.14: Change in nominal fitted yields due to the uncertainty on the PDF model. Each parameter is varied within $\pm 1\sigma$ of its nominal value.

5.9.7 Further sources of systematic error

- The number of $B\bar{B}$ events is derived from hadronic events and muon pairs using the methods discussed in [57]. The number of $B\bar{B}$ pairs is found to be $N_{B\bar{B}} = 88.837 \pm 0.002\,(\text{stat}) \pm 0.977\,(\text{syst}) \times 10^6$. The systematic uncertainty is thus 1.1%.
- M.L. fit bias: This is determined from embedding studies as described in sec-

tion 5.6.3 where we take the bias to be 3%.

- Selection cuts: The systematic uncertainty for $\cos(\theta^B_{\mathrm{sph}})$ is based upon the expectation that the $\cos(\theta^B_{\mathrm{sph}})$ distribution for signal Monte Carlo should be flat. Based on the signal efficiency for a selection $|\cos(\theta^B_{\mathrm{sph}})| < 0.7$ and its deviation from the expectation for a flat distribution, we assign a systematic of 2.8%. The systematic error due to $\cos(\theta_H^{K^{*+}})$ is handled using a similar approach as above. The $\cos(\theta_H^{K^{*+}})$ variable would be expected to be distributed as $\cos^2(\theta_H^{K^{*+}})$. Based on the signal efficiency for a selection $\cos(\theta_H^{K^{*+}}) > -0.7$ and its deviation from the expectation for a quadratic distribution, we assign a systematic of 1.0%.

- $B\bar{B}$ crossfeed background: In sections 5.5 and 5.6.1 we calculated the number of charmless events which must be subtracted from the signal fit yield. The modes considered are given in table 5.9. We subtract $2.12 \pm 0.58_{fit} \pm (0.46 \pm 0.14)_{\mathcal{BR}(B\bar{B})}$ events. The first error arises from the uncertainty in the number of crossfeed events used to obtain the fit mis-identification efficiencies in section 5.6.4. The second and third errors are due to the uncertainties on the branching fractions for the B modes. We add all three errors in quadrature to determine the total systematic error on the $B\bar{B}$ crossfeed background where we obtain 2.12 ± 0.75.

In table 5.15 we give all systematic corrections required to correct the signal Monte Carlo efficiency. In table 5.16 we give the systematic errors arising from the efficiency corrections, number of $B\bar{B}$ pairs and signal fit yield. For each of the corrections we add the errors in quadrature.

Table 5.15: The systematic corrections required to correct the Monte Carlo efficiency for $B^0 \to K^{*+}\pi^-$, $K^{*+} \to K^+\pi^0$.

Source	% M.C. correction in $\mathcal{BR}(B^0 \to K^{*+}(K^+\pi^0)\pi^-)$
$K^\pm/\pi^\pm$ tracking	0.984
π^0 γ smearing	0.976
Kaon ID	0.975
Total	0.936

Table 5.16: Sources of systematic uncertainties in the measurement of $\mathcal{BR}(B^0 \to K^{*+}\pi^-, K^{*+} \to K^+\pi^0)$.

Source	% Uncertainty $\mathcal{BR}(B^0 \to K^{*+}(K^+\pi^0)\pi^-)$
Efficiency systematic errors.	
$h^\pm$, $h = K, \pi$ track	7.0
Trk. Multiplicity	1.0
Kaon ID	2.0
π^0	5.0
$\cos(\theta_H^{K^{*+}}) > -0.7$	1.0
$\lvert\cos(\theta_{\rm sph}^B)\rvert < 0.7$	2.8
Total	9.4
Systematic errors on $N_{B^0\to K^{*+}\pi^-}$	
PDF model	2.0
M.L. fit bias	3.0
Crossfeed error	2.5
Total	4.4
B counting	1.1

5.10 Branching fraction result for $B^0 \to K^{*+}\pi^-$

The branching fraction is measured as:

$$\mathcal{BR}(B^0 \to K^{*+}\pi^-) = \frac{N_{B^0 \to K^{*+}\pi^-}}{N_{B\bar{B}}\epsilon \mathcal{BR}(K^{*+} \to K^+\pi^0)\mathcal{BR}(\pi^0 \to \gamma\gamma)}. \tag{5.9}$$

Where ϵ is the Monte Carlo corrected signal efficiency $\epsilon = (11.30 \pm 0.14 \pm 1.06)\%$, $\mathcal{BR}(K^{*+} \to K^+\pi^0) = 0.33$, $\mathcal{BR}(\pi^0 \to \gamma\gamma) = (98.798 \pm 0.032)\%$ [15] and $N_{B^0 \to K^{*+}\pi^-} = N_{\text{sig}} - N_{\text{Xfeed}}$. Where N_{sig} is the signal category fit yield and N_{Xfeed} is the number of $B\bar{B}$ crossfeed. The resulting branching fraction is determined to be:

$$\mathcal{BR}(B^0 \to K^{*+}\pi^-) = (8.42^{+2.51}_{-2.23}\,(\text{stat}) \pm 0.87\,(\text{syst})) \times 10^{-6}. \tag{5.10}$$

Mode	Eff(%)	# $B\bar{B}$ crossfeed	#Signal Events	$\mathcal{BR}(B^0 \to K^{*+}\pi^-)$ $\pm$ stat $\pm$ syst $\times 10^{-6}$
$K^+\pi^0$	11.30	2.12 ± 0.75	$30.0^{+8.3}_{-7.4}$	$8.42^{+2.51}_{-2.23} \pm 0.87$

The measurement presented here for $B^0 \to K^{*+}\pi^-$ lies within 2σ of the BELLE [32] and CLEO [33] results. However, the *BABAR* result obtained in this thesis has the highest statistical significance of 5.3. We find that the QCD factorisation prediction for the branching fraction $\mathcal{BR}(B^0 \to K^{*+}\pi^-) = (8.1^{+1.4+1.3+0.8+6.2}_{-1.2-1.2-0.8-1.6}) \times 10^{-6}$ agrees well with the measured value. The *BABAR* dataset will soon reach $200\,fb^{-1}$ when it will become possible to probe for direct CP effects within this mode.

Chapter 6

Branching fraction analysis of $B^0 \to K^{*0}\pi^0$

6.1 Introduction

The goal of this chapter is to present an analysis for the decay $B^0 \to K^{*0}\pi^0$ and to measure the branching fraction $\mathcal{BR}(B^0 \to K^{*0}\pi^0)$. The analysis follows closely that of $B^0 \to K^{*+}\pi^-$. The yields and continuum background parameters are determined from a maximum likelihood fit. The fit uses the variables ΔE, $\cos(\theta_H^{K^{*0}})$, $m(K^{*0})$, m_{ES} and $\mathcal{F}$. The discussion will refer to the details of the previous chapter to recapitulate the main ideas of the analysis method. The analysis centers on the development of the fit model consisting of a set of independent discrimination variables for both signal and background components. We give the correlations of the fit variables in section 6.2 and discuss the selection efficiencies in section 6.3. We give the parameterisations of the fit variables in section 6.4 and the analysis backgrounds are discussed in section 6.5. In section 6.6 validation studies are undertaken to determine bias in the estimators, effectiveness of fit reconstruction efficiency and understand how potential B backgrounds are handled by the fit. The fit results are given in section 6.8 and the analysis of systematic errors is described in section 6.9. We present the branching fraction measurement in section 6.10.

6.2 Fit variables and their correlations

In order to use the maximum likelihood technique the variables used in constructing the likelihood function must be independent for each event type. For the $B^0 \to K^{*0}\pi^0$ analysis we find no significant correlations in either signal or continuum $q\bar{q}$ background. The correlation matrices are shown in table 6.1 for signal $B^0 \to K^{*0}\pi^0$ Monte Carlo and table 6.2 for continuum Monte Carlo.

	ΔE	$\cos(\theta_H^{K^{*0}})$	$m(K^{*0})$	m_{ES}	$\mathcal{F}$
ΔE	1				
$\cos(\theta_H^{K^{*0}})$	-0.003	1			
$m(K^{*0})$	0.017	-0.003	1		
m_{ES}	0.028	0.012	-0.022	1	
$\mathcal{F}$	-0.005	0.006	0.007	-0.022	1

Table 6.1: Correlation matrix for the maximum likelihood fit variables for Signal $B^0 \to K^{*0}\pi^0$ Monte Carlo.

	ΔE	$\cos(\theta_H^{K^{*0}})$	$m(K^{*0})$	m_{ES}	$\mathcal{F}$
ΔE	1				
$\cos(\theta_H^{K^{*0}})$	-0.001	1			
$m(K^{*0})$	0.019	0.002	1		
m_{ES}	0.004	0.002	0.004	1	
$\mathcal{F}$	-0.068	0.001	0.0	-0.016	1

Table 6.2: Correlation matrix for the maximum likelihood fit variables for the $q\bar{q}$ background.

6.3 Selection efficiencies

The selection variables and pre-selection criteria are discussed in chapter 4. The $B^0 \to K^{*0}\pi^0$ selections involve a hard E_γ selection discussed in section 4.6.2. In addition, there is a looser selection on $\cos(\theta^{B}_{\mathrm{sph}})$ discussed in section 4.7. The selection on $\cos(\theta^{K^{*0}}_{H})$ requires that $-0.85 < \cos(\theta^{K^{*0}}_{H}) < 0.85$ in order to remove a small background component from $B^0 \to \rho^- K^+$ which affects the extreme $\cos(\theta^{K^{*0}}_{H}) = -1$. It also removes badly reconstructed events where high energy kaons and pions can not be correctly identified due to the acceptance of the DIRC.

In table 6.3 we show both candidate and event selection efficiencies for $B^0 \to K^{*0}\pi^0$ Monte Carlo where each efficiency is given relative to the previous selection. For $B^0 \to K^{*+}\pi^-$ the pre-selection process reconstructed many multiple candidates per event whereas in $B^0 \to K^{*0}\pi^0$ the ratio of candidates to events is significantly lower. The dominant reason for this is due to the requirement of reconstructing a high energy π^0 in the $B^0 \to K^{*0}\pi^0$. After all selection cuts we find that 1% of the remaining events contain multiple candidates. In the cases where an event contains multiple candidates then the final candidate is determined by random selection. This has been determined to be the safest and most bias free method of candidate selection. We find that the selection efficiency for $B^0 \to K^{*0}\pi^0$ is $13.70 \pm 0.11\%$.

Table 6.4 shows the event selection efficiencies for $81.878\,fb^{-1}$ on-peak data, $9.578\,fb^{-1}$ off-peak data, $1043\,fb^{-1}$ *udsc* continuum Monte Carlo and $140.5\,fb^{-1}$ combined $B\bar{B}$ B^+B^-(50%), $B^0\bar{B}^0$(50%) Monte Carlo ($B^0 \to K^{*0}\pi^0$ signal events removed) where each efficiency is given relative to the previous selection. We find that 3494 on-peak events and 489 off-peak events remain after all selections have been applied.

Pre-selected number of $K^{*0}\pi^0$ candidates	114867	-
Pre-selected number of $K^{*0}\pi^0$ events	-	61160
Eff(%) $B^0 \rightarrow K^{*0}\pi^0$	Candidates	Events
$\lvert\cos(\theta^B_{\mathrm{sph}})\rvert < 0.8$	76.8	85.2
Neutral selection		
$E_\gamma > 150.0\,\mathrm{MeV}$	77.9	83.7
$0.12 < m(\pi^0) < 0.15\,\mathrm{GeV/c^2}$	89.1	89.5
Charged track selection		
Reconstruction $\pi\,K$ PID	68.3	78.0
K^{*0} resonance		
$0.8 < m(K^{*0}) < 1.0\,\mathrm{GeV/c^2}$	58.1	77.2
$-0.85 < \cos(\theta_H^{K^{*0}}) < 0.85$	70.0	70.5
B candidate		
$\lvert\Delta E\rvert < 150\,\mathrm{MeV}$	89.6	91.3
$5.2 < m_{ES} < 5.29\,\mathrm{GeV/c^2}$	99.9	99.8
Total	13.25	13.70

Table 6.3: Selection efficiencies in $\epsilon(\%)$ for $B^0 \rightarrow K^{*0}\pi^0$ Monte Carlo. First column: Candidate selection efficiencies for all reconstructed B candidates. Second column: Per event selection efficiencies.

Eff(%)	ϵ(onpeak)	ϵ(offpeak)	ϵ(udsc M.C.)	$\epsilon(B\bar{B})$
Data pre-selection	2.1	2.1	-	-
M.C. pre-selection	-	-	2.1	0.2
$\lvert\cos(\theta^{B}_{\mathrm{sph}})\rvert < 0.8$	17.6	17.5	28.4	73.2
Neutral selection				
$E_\gamma > 150.0\,\mathrm{MeV}$	63.6	62.5	62.8	68.5
$0.12 < m(\pi^0) < 0.15\,\mathrm{GeV/c^2}$	82.3	81.0	85.0	84.7
Charged track selection				
π, K PID	26.9	26.2	25.8	26.8
K^{*0} resonance				
$0.8 < m(K^{*0}) < 1.0\,\mathrm{GeV/c^2}$	9.3	9.2	9.1	3.6
$-0.85 < \cos(\theta_H^{K^{*0}}) < 0.85$	86.1	87.4	93.3	81.5
B candidate				
$\lvert\Delta E\rvert < 150\,\mathrm{MeV}$	29.9	30.0	30.3	13.1
$5.2 < m_{ES} < 5.29\,\mathrm{GeV/c^2}$	89.8	88.1	88.2	91.5
Total	1.1×10^{-5}	1.03×10^{-5}	1.87×10^{-5}	0.8×10^{-6}

Table 6.4: Selection efficiencies for on-peak data, off-peak data, $140.5\,fb^{-1}$ $B\bar{B}$ Monte Carlo and $1043\,fb^{-1}$ udsc Monte Carlo.

6.4 Parameterisation of signal & continuum background

The parameterisations of the PDFs for the fit variables are determined from $B^0 \to K^{*0}\pi^0$ Monte Carlo and continuum $q\bar{q}$ Monte Carlo. Figure 6.1 and figure 6.2 show the distributions of each fit variable. Also shown are the results of an unbinned maximum likelihood fit used to determine the initial parameterisations of the fit variables. The primary aim is to establish the shapes of the probability density functions. The goodness of fit quality of the parameterisations is determined later in section 6.6.

- m_{ES}: The shape of the energy substituted mass m_{ES} is parameterised using the Crystal Ball function for signal and the ARGUS function for continuum $q\bar{q}$ background as in section 5.4.

- ΔE: The signal ΔE shape is parameterised with a double Gaussian. The large tail for negative ΔE is attributed to energy loss in the electromagnetic calorimeter. This effect is found for other modes which involve high energy photons such as $B^0 \to K^{*0}\gamma$ which differs from $B^0 \to K^{*0}\pi^0$ by a photon and has a similar distribution in ΔE. For continuum background, ΔE is parameterised with a first order polynomial function.

- Linear discriminant $\mathcal{F}$: The linear discriminant variable $\mathcal{F}$ for signal is parameterised with a Gaussian. The continuum background is slightly asymmetric and is parameterised using an asymmetric Gaussian distribution.

- $K^{*0}(892)$ mass: The signal K^{*0} shape is parameterised using a Breit-Wigner distribution with the mass and width fixed to the PDG values [15]. For continuum background the K^{*0} shape is parameterised with a combination of a Breit-Wigner and first order polynomial background as used for the $B^0 \to K^{*+}\pi^-$ in section 5.4.

- $\cos(\theta_H^{K^{*0}})$: The signal shape for $\cos(\theta_H^{K^{*0}})$ is described with a 2nd order Chebyshev polynomial function (equation 5.4). The distribution is essentially a pure quadratic. However, a linear term is included which is helpful in determining a systematic error due to any differences between data and the Monte Carlo.

For continuum background the $\cos(\theta_H^{K^{*0}})$ shape is parameterised with a constant function.

6.5 $B\bar{B}$ backgrounds in $B^0 \to K^{*0}\pi^0$

For $B^0 \to K^{*0}\pi^0$ the backgrounds are similar to the analysis of $B^0 \to K^{*+}\pi^-$ (chapter 5). These consist of the dominant $q\bar{q}$ continuum background and backgrounds arising from $B\bar{B}$ modes. For the continuum background the discussion is identical to the $B^0 \to K^{*+}\pi^-$ analysis and the reader is referred to section 4.7. In order to determine the B background modes specific to $B^0 \to K^{*0}\pi^0$, large samples of $B\bar{B}$ Monte Carlo are generated and reconstructed using the $B^0 \to K^{*0}\pi^0$ selection criteria in section 6.3. The samples used to study the $B\bar{B}$ backgrounds are the same as those used in the $B^0 \to K^{*+}\pi^-$ analysis corresponding to $140.5\,fb^{-1}$.

The distributions for ΔE, $\cos(\theta_H^{K^{*0}})$, $m(K^{*0})$, m_{ES}, $\mathcal{F}$ are shown in figure 6.3 for B^+B^- and $B^0\bar{B}^0$ Monte Carlo. All selection cuts in section 6.3 have been applied to the $B\bar{B}$ Monte Carlo. Table 6.5 gives the number of reconstructed $B\bar{B}$ events for the generated $B\bar{B}$ Monte Carlo. From both figure 6.3 and table 6.5 the background from B decays is seen to consist of a small combinatoric component with a significant signal-like component in the m_{ES} distribution for $B^0\bar{B}^0$. This strong peak is mainly due to the charmless decay $B^0 \to K^+K^-\pi^0$.

6.5.1 Charmless $B\bar{B}$ backgrounds

To identify backgrounds due to rare B modes, a large sample of events has been generated consisting of $B\bar{B}$ decay modes where one of the B decays is forced to decay to a mode containing no charm particles. We apply the selection criteria of section 6.3 and select those events in the m_{ES} signal region which we define to be $5.270 < m_{ES} < 5.288$ GeV/c^2.

Figure 6.4 shows the distribution of the m_{ES} and ΔE variables after all selection cuts in the charmless $B\bar{B}$ Monte Carlo. Table 6.6 describes the different charmless modes contributing in the region $5.270 < m_{ES} < 5.288$ GeV/c^2. Given the large size of the rare charmless B sample, modes contributing only one event are not expected

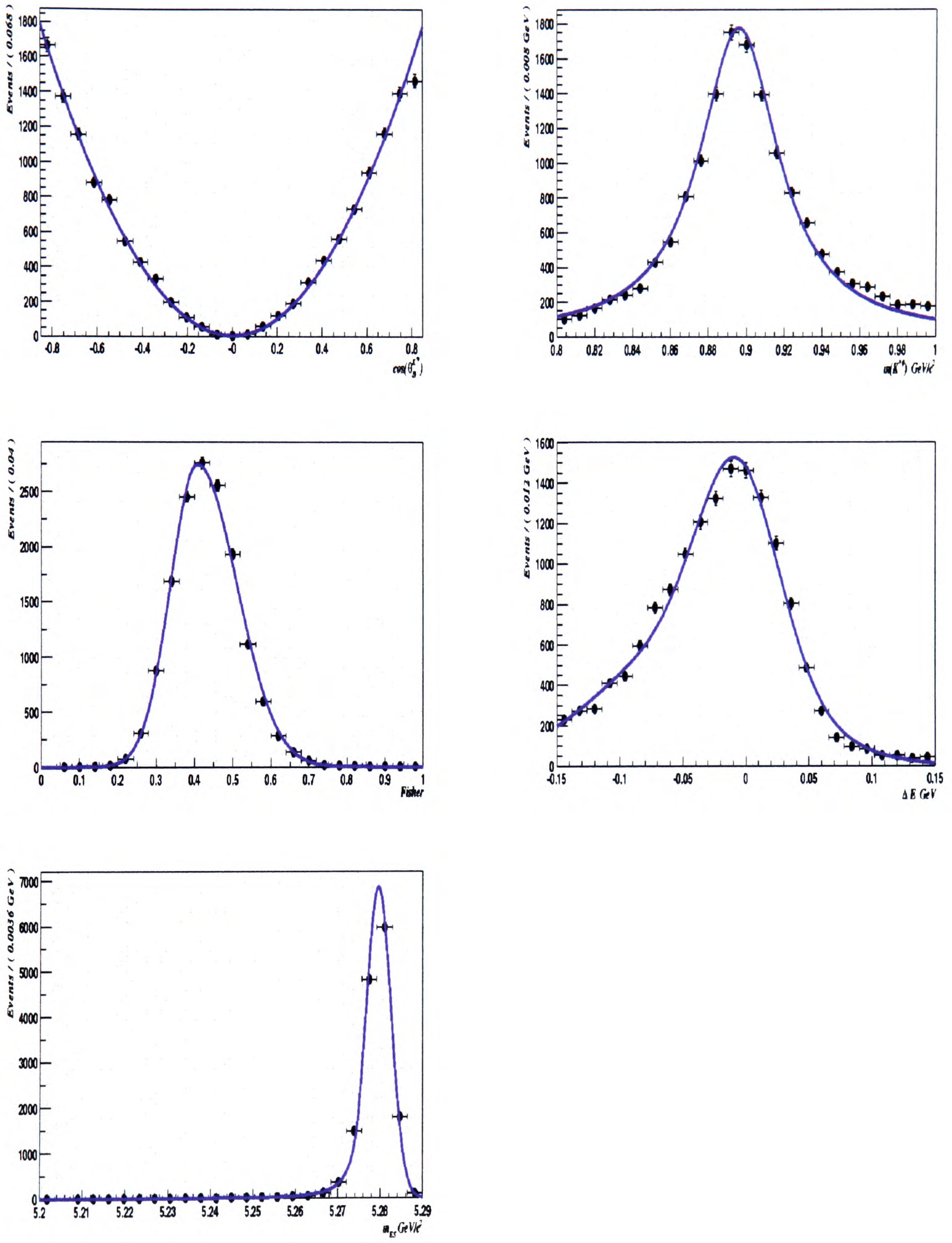

Figure 6.1: Parameterisation of the maximum likelihood fit variables for signal $B^0 \to K^{*0}\pi^0$ Monte Carlo.

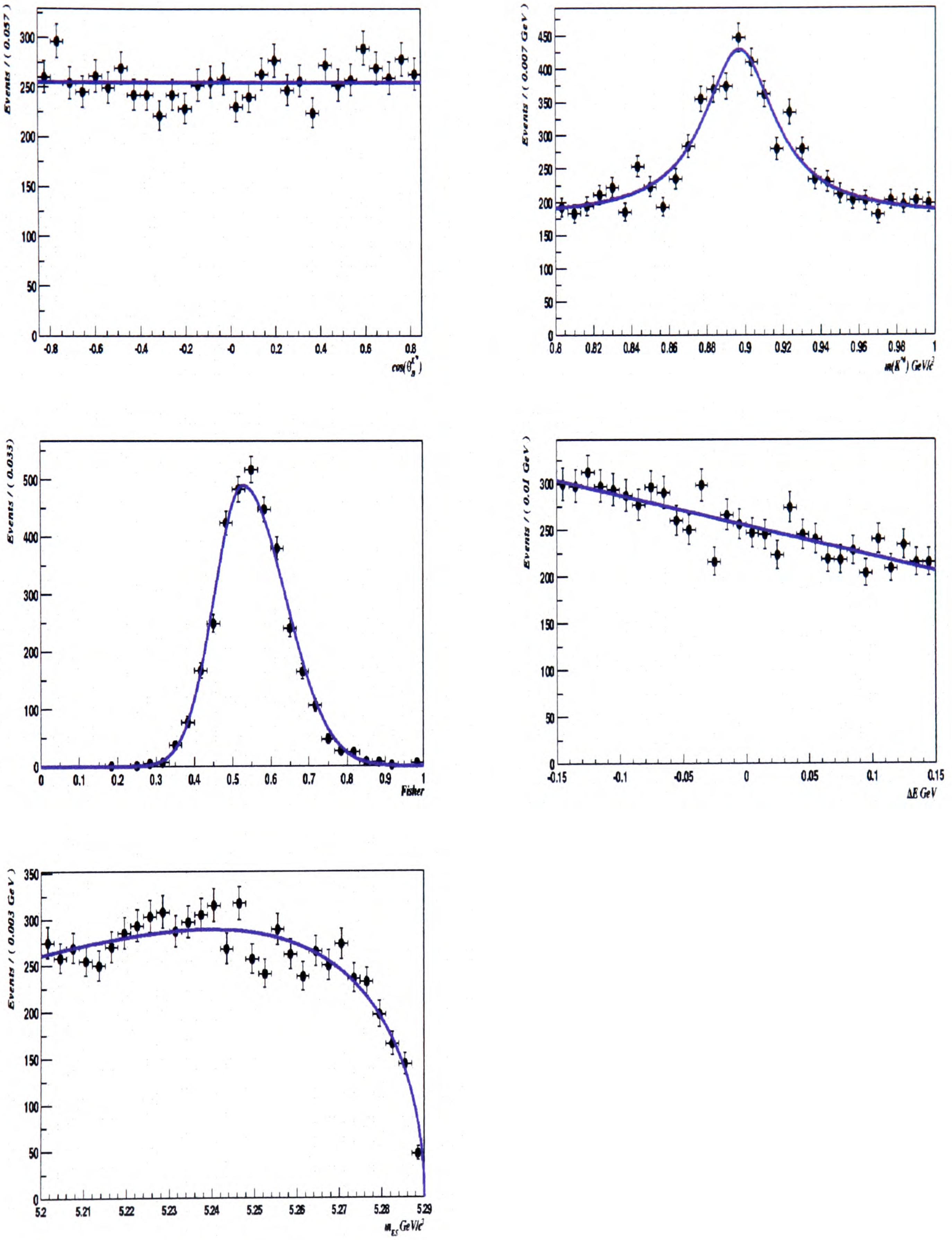

Figure 6.2: Parameterisation of the maximum likelihood fit variables for Monte Carlo continuum $q\bar{q}$ background in the $B^0 \to K^{*0}\pi^0$ analysis.

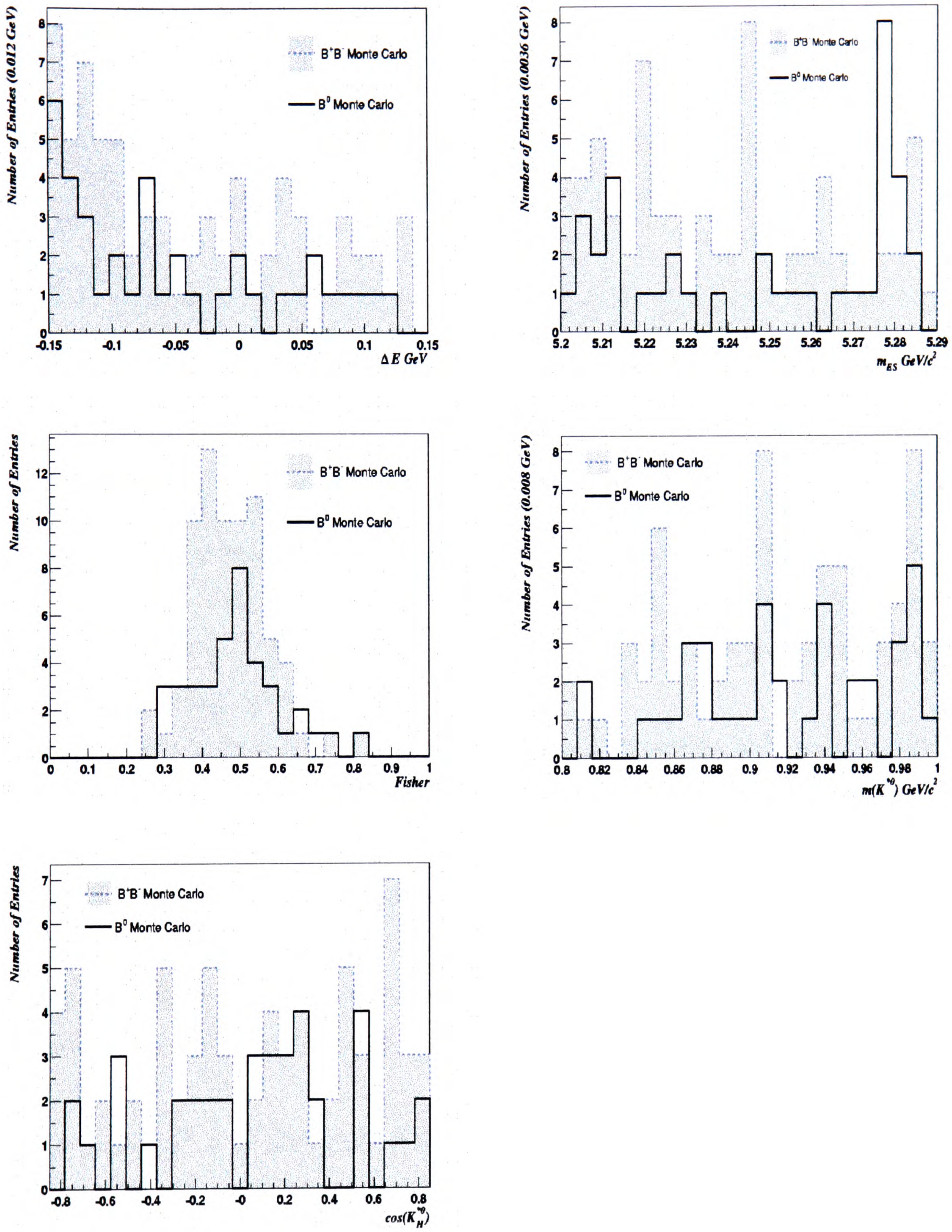

Figure 6.3: The ΔE, $\cos(\theta_H^{K^{*0}})$, $m(K^{*0})$, m_{ES}, $\mathcal{F}$ distributions in B^+B^- Monte Carlo and $B^0\bar{B}^0$ Monte Carlo. The distributions are obtained after the event selection in section 6.3.

Mode	$\mathcal{BR}(10^{-6})$	N reco ($140.5\,fb^{-1}$)	N expected ($81\,fb^{-1}$)
Peak $B\bar{B}$, $5.270 < m_{ES} < 5.288$ GeV/c^2			
$B^0 \to K^+K^-\pi^0$	< 19	10	-
$B^0 \to K^{*0}\gamma$	40.3 ± 2.5	1	-
Total $B\bar{B}$, $5.2 < m_{ES} < 5.29$ GeV/c^2			
B^+B^-	-	72	40.56
$B^0\bar{B}^0$	-	38	22.43

Table 6.5: Reconstructed $B\bar{B}$ events in $140.5\,fb^{-1}$ and expected number of events in $81\,fb^{-1}$.

to enter the signal region for $81\,fb^{-1}$. Instead they are treated as contributions to the combinatorial component of the $B\bar{B}$ background. For modes where more than one event is observed, a large statistics sample of Monte Carlo is generated to study each mode further. Where the branching fractions are measured we use the results of the heavy flavour averaging group [24].

In addition to using generic samples of $B\bar{B}$ and charmless Monte Carlo we consider in more detail those B decay modes which could be reconstructed as signal in the maximum likelihood fit. The largest signal-like backgrounds in the $B^0 \to K^{*0}\pi^0$ analysis are found to come from the non-resonant three-body decays $B^0 \to K^+\pi^-\pi^0$(N.R.) and $B^0 \to K^+K^-\pi^0$(N.R.) due to the mis-identification of a kaon as a pion. Backgrounds from $B^0 \to \rho^- K^+$ are found to be negligible due to the helicity selection. For backgrounds arising from B decays with four-body final states we expect less than one event.

The modes $B^0 \to f_0^0(980, 1270, 1370)K^{*0}, f_0 \to \pi^0\pi^0$ and $B^0 \to f_0(980, 1270, 1370)\pi^0$, $f_0 \to \pi^+\pi^-$, could possibly enter the fit region. $B^0 \to f_0(980, 1270, 1370)K^{*0}$ would be shifted in ΔE due a lost π. Thus, our ΔE cut of 150 MeV/c^2 will suppress the majority of this background.

The mode $B^0 \to f_0(980, 1270, 1370)\pi^0$ would contribute due to the misidentification of a pion. Unfortunately, no Monte Carlo was available to study all these modes in detail. The nearest mode to $B^0 \to f_0 K^{*0}$ is $B^0 \to \pi^0\pi^0 K^{*0}$. This mode is included in

Mode	$\mathcal{BR}(10^{-6})$ Generated	$\mathcal{BR}(10^{-6})$ Measured	N reco
Peak charmless $B\bar{B}$, $5.270 < m_{ES} < 5.288$ GeV/c^2			
$B^0 \to K^{*0}\pi^0\pi^0$	1.0	-	4
$B^0 \to \rho^0\pi^+\pi^0$	1.0	-	4
$B^0 \to K^+\pi^-\pi^0$	1.0	-	4
$B^0 \to \rho^+\pi^-\pi^0$	1.0	-	1
$B^0 \to f_0(980)\pi^0$	1.0	-	1
$B^0 \to K_x^{*0}\gamma$	1.0	-	2
$B^0 \to f_2(1270)\rho^+\pi^+\pi^0$	1.0	-	1
$B^+ \to K^+\pi^0\pi^0$	1.0	-	1
$B^+ \to \pi^+\pi^0\pi^0$	1.0	-	1
$B^+ \to \pi^+\pi^0\omega^0$	1.0	-	1
$B^+ \to K^+\pi^0\bar{K}^0$	1.0	-	1
$B^+ \to \pi^0K^+K^-\pi^+$	1.0	-	1
$B^0 \to K^+K^-\pi^0$	1.0	< 19	11
$B^0 \to K^{*0}\gamma$	40.3	40.3 ± 2.5	5
$B^0 \to K^{*0}\rho^+$	1.0	-	3

Table 6.6: Contributing charmless B background modes for the m_{ES} region $5.270 < m_{ES} < 5.288$ GeV/c^2 determined from charmless $B\bar{B}$ Monte Carlo. The charmless sample corresponds to an integrated luminosity of $\approx 10000\, fb^{-1}$.

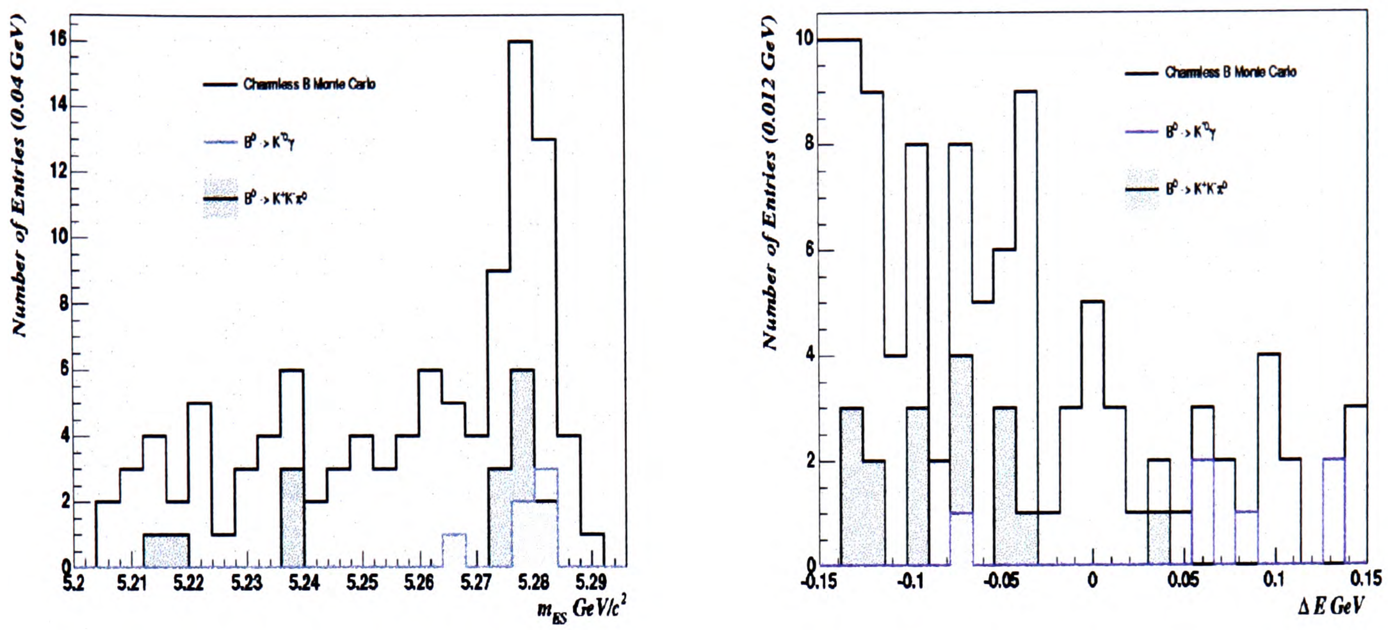

Figure 6.4: m_{ES} and ΔE distributions in charmless $B\bar{B}$ Monte Carlo.

our charmless sample where we expect 0.022 events. We assume that any backgrounds from $B^+ \rightarrow f_0(980, 1270, 1370)K^{*+}$ are similarly suppressed. Possible contamination from decay modes with a higher kaon resonance is estimated from the BELLE result for $B^0 \rightarrow K_x^{*0}\pi^0$. Table 6.7 shows the results for the dominant sources of B background. The main source of error on the number of $B\bar{B}$ is due to the uncertainty of the branching fraction for each background mode. Where the branching fractions are measured we use the results of the heavy flavour averaging group [24]. In the cases where branching fractions are not yet measured they are estimated using the nominal value of 1.0×10^{-6}. For these unmeasured modes we obtain a systematic error as the number of expected events using a branching fraction of 10×10^{-6}.

6.5.2 Summary of $B\bar{B}$ backgrounds

There are two components for the $B\bar{B}$ background. A combinatoric component where we expect 63 events for a sample of 81 fb^{-1}. This background is expected to be handled by the continuum background PDF models. This is studied in section 6.6. In addition, there is a charmless crossfeed component where B events closely resemble the signal mode $B^0 \rightarrow K^{*0}\pi^0$. These events will be reconstructed as signal in the maximum likelihood fit. From table 6.7 we expect $6.69 \pm 1.22 \pm 3.19$ events. In section 6.6

Mode	$\mathcal{BR}(10^{-6})$	Eff	# Gen	# Exp ($81\,fb^{-1}$)
$B^0 \to K^+K^-\pi^0$(N.R.)	< 19 [24]	1.2×10^{-3}	47K	1.00 ± 1.00
$B^0 \to K^+\pi^-\pi^0$(N.R.)	$5.7^{+2.7+0.5}_{-2.5-0.4}$ [32]	4.3×10^{-3}	42K	$2.18^{+1.04+0.19}_{-0.97-0.23}$
$B^0 \to K_x^{*0}\pi^0$	$6.1^{+1.6+0.5}_{-1.5-0.6}$ [32]	4.3×10^{-3}	-	$2.33^{+0.63+0.19}_{-0.56-0.23}$
$B^0 \to K^{*0}\gamma$	40.3 ± 2.5 [24]	2.3×10^{-4}	163K	0.82 ± 0.14
$B^0 \to \rho^0\pi^+\pi^0$	1.0	$< 0.2 \times 10^{-4}$	50K	0.0
$B^0 \to K^{*0}\pi^0\pi^0$	1.0	3.5×10^{-4}	20K	$0.02^{+0.22}_{-0.02}$
$B^+ \to K^{*0}\rho^+$ (Long.)	1.0	3.8×10^{-3}	49K	$0.33^{+3.00}_{-0.33}$
$B^+ \to K^{*0}\rho^+$ (Trans.)	1.0	1.6×10^{-4}	49K	$0.01^{+0.13}_{-0.01}$
Total				$6.69 \pm 1.22 \pm 3.19$

Table 6.7: Main expected sources of signal-like crossfeed $B\bar{B}$ background for the $B^0 \to K^{*0}\pi^0$ analysis. The number of events given, is for the full fit region.

we perform studies to determine how many crossfeed B events are reconstructed as signal using the additional information in the fit. From these studies we can determine the number to subtract from the reconstructed signal yield. For the remainder of the analysis we reserve the term crossfeed for the charmless backgrounds resulting from $B^0 \to K^+\pi^-\pi^0$ (N.R.), higher kaon resonance modes and non-resonant $B^0 \to K^+K^-\pi^0$.

6.6 Fit validation

In this section we summarise the validation studies. The techniques used to validate the maximum likelihood fit method are discussed in section 5.6.1. We present the results of the studies in Table 6.8.

We choose to float some of the background PDF parameters in the maximum likelihood fit. The floating of the background serves two purposes. It eliminates the need to include systematic errors on the background model parameters as they are not determined from Monte Carlo. Secondly, it includes the small $B\bar{B}$ component which is largely combinatorial. Validation studies are performed as in section 6.6.1, to determine if the fit is stable. The following parameters are allowed to float within the maximum likelihood fit:

- **Number of reconstructed events.**

  $N_{\rm sig}$: Number of reconstructed $B^0 \to K^{*0}\pi^0$.

  $N_{q\bar{q}}$: Number of reconstructed continuum background.

- **Continuum parameters**

  ξ: The m_{ES} ARGUS shape parameter.

  c_1: 1st order coefficient of ΔE.

  σ_L: Left width of $\mathcal{F}$ distribution.

  σ_R: Right width of $\mathcal{F}$ distribution.

  μ: Mean of $\mathcal{F}$ distribution.

6.6.1 Monte Carlo studies

The pull distributions for 1000 pure toy Monte Carlo experiments are shown for the $B^0 \to K^{*0}\pi^0$ analysis in figures 6.5 and 6.6. Pull distributions are given for all floating parameters and the signal and background yields. The results indicate that there is no significant bias observed in either the event yield estimators or the estimators of the floating parameters of the continuum background. We perform an identical Monte Carlo study as described in section 5.6.3 to validate our $B^0 \to K^{*0}\pi^0$ signal PDF model. The signal yield pull distribution is shown in figure 6.7 (right plot) for embedded signal Monte Carlo and continuum toy events for a set of 500 experiments with inputs $N_{\rm sig} = 25$, $N_{\rm bkg} = 3580$. We observe no significant bias in floating the background parameters. The signal yield $N_{\rm sig}$ has a small bias which we include in our systematic errors.

The $B\bar{B}$ background for this analysis is expected to contain both a combinatoric $B\bar{B}$ and crossfeed component as discussed in section 6.5. Following the method of section 5.6.4 we embed the expected number of 60 $B\bar{B}$ Monte Carlo events into a sample of 25 signal Monte Carlo and 3520 toy continuum Monte Carlo. We do not include any of the $B^0 \to K^+\pi^-\pi^0$ or $B^0 \to K^+K^-\pi^0$ crossfeed events. Figure 6.7 (left plot) shows the resulting pull distribution for the signal yield. We observe no significant difference to the bias thus concluding that at the level of sensitivity required, most of the $B\bar{B}$ background is handled by the continuum background model in section 6.4.

To study the sensitivity of signal yield in the presence of the crossfeed B backgrounds we follow the same method as detailed in section 5.6.4. The results are given in table 6.8. We find that for $B^0 \to K^+\pi^-\pi^0$ the fit crossfeed reconstruction efficiency is $50 \pm 15\%$ and $10 \pm 20\%$ for $B^0 \to K^+K^-\pi^0$ (N.R.). Thus, we expect a total of $3.53 \pm 0.71_{fit} \pm (0.61 \pm 3.02)_{\mathcal{BR}(B\bar{B})}$ charmless background events to be reconstructed as signal. The first error is the fit efficiency error. The second and third errors are from the errors on the B mode branching fractions.

6.6.2 Comparisons of $-\log \mathcal{L}_{\mathrm{max}}$

Figure 6.8 shows the comparison of the distribution of $-\log \mathcal{L}$ obtained from Monte Carlo studies discussed earlier in section 5.6.5 with the value obtained from data. The agreement between the mean of the $-\log \mathcal{L}$ distribution and the data value of $-\log \mathcal{L}_{\mathrm{max}} = -46267$ indicate that the continuum $q\bar{q}$ background is well described by the parameterisations described in section 6.2.

6.7 Comparisons of data and Monte Carlo

To make the comparison, we choose the ΔE side-band region defined as $0.2 < \Delta E < 0.4\,\mathrm{GeV}$ as here there is only a small amount of $B\bar{B}$ contamination. Figure 6.9 shows the distribution of ΔE and m_{ES} in $B\bar{B}$ Monte Carlo. The number of $B\bar{B}$ events with $0.2 < \Delta E < 0.4\,\mathrm{GeV}$ and satisfying the same selections as above is $34\,B^+B^-$ events, $12\,B^0\bar{B}^0$ events and the number expected in $81\,fb^{-1} = 26.2$. This is small compared to the 3537 on-peak side-band events.

In figure 6.10 we compare off-peak and on-peak data to continuum Monte Carlo in the ΔE side-band region. All figures contain events which pass the entire set of selection cuts in section 6.4 apart from the looser restrictions on $\cos(\theta^B_{\mathrm{sph}})$ and ΔE. We see that Monte Carlo describes data well and confirms our chosen background shapes

Figure 6.5: Pure toy Monte Carlo results showing the pull distributions of the yields and floated parameters for the $B^0 \rightarrow K^{*0}\pi^0$ analysis.

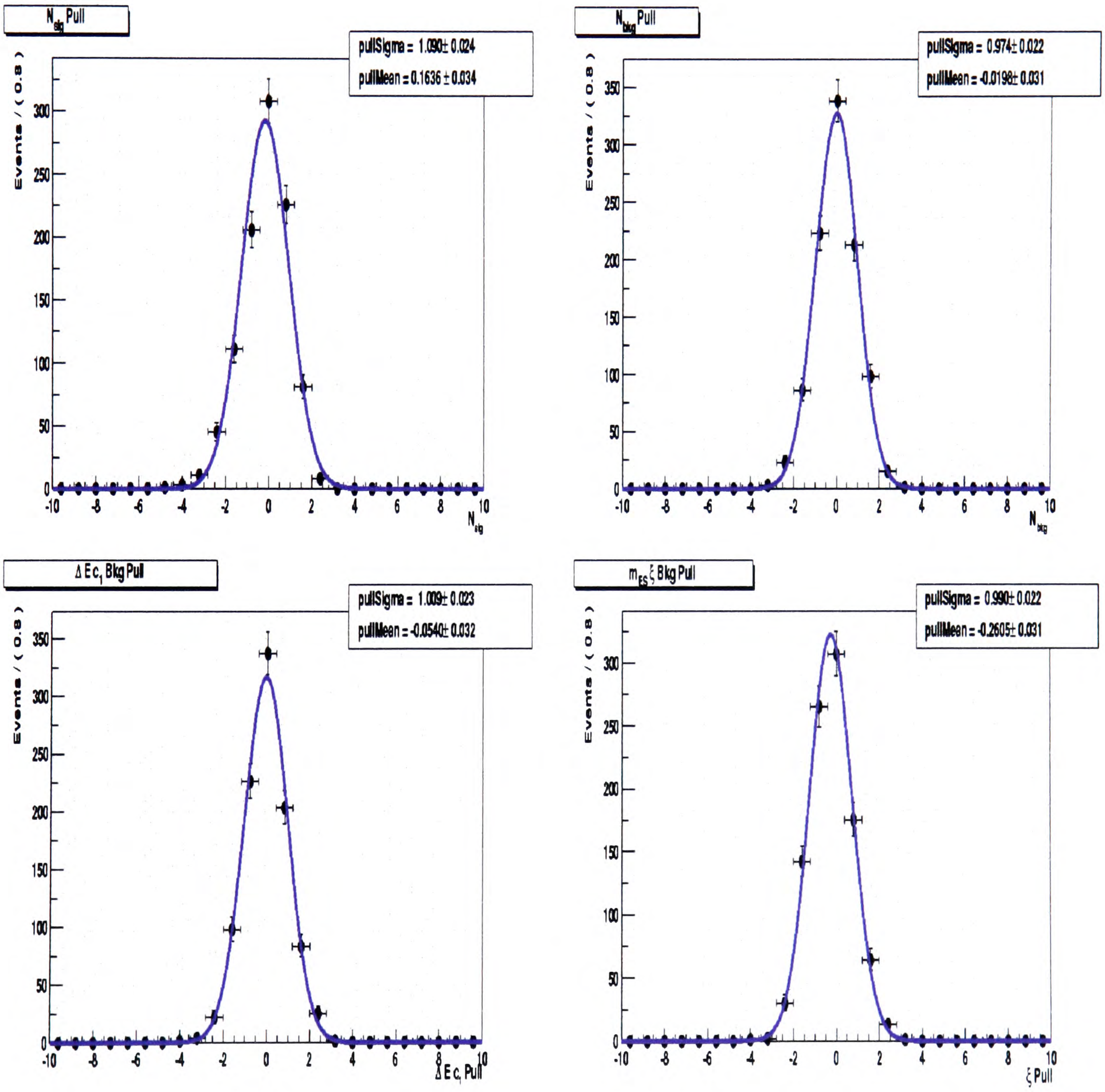

Figure 6.6: Further pure toy Monte Carlo results showing the pull distributions of the yields and floated parameters.

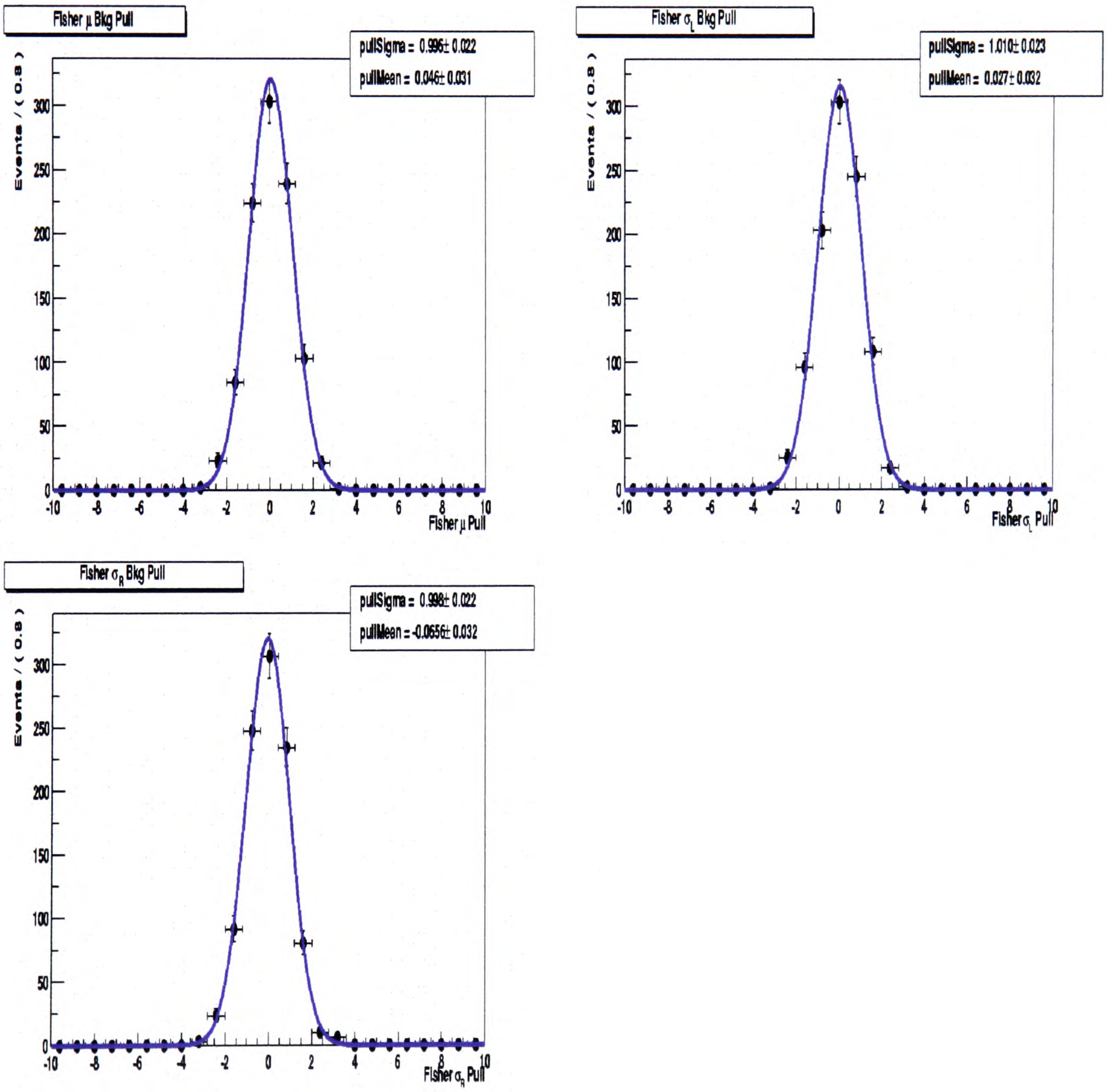

Figure 6.7: Monte Carlo studies showing the $B^0 \to K^{*0}\pi^0$ signal pull distributions for 500 experiments. Right: Embedded signal Monte Carlo and continuum toy events. Left: Embedded signal Monte Carlo, combinatoric $B\bar{B}$ Monte Carlo and continuum toy events.

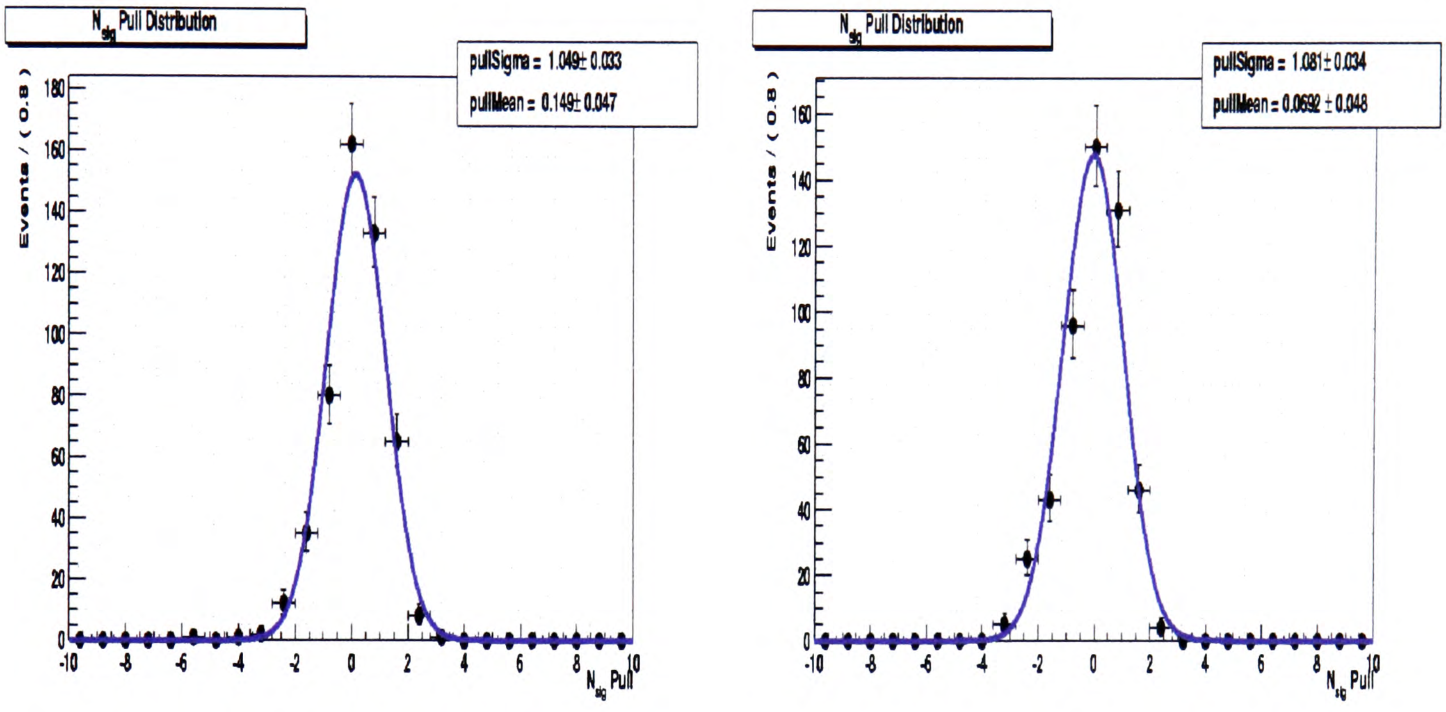

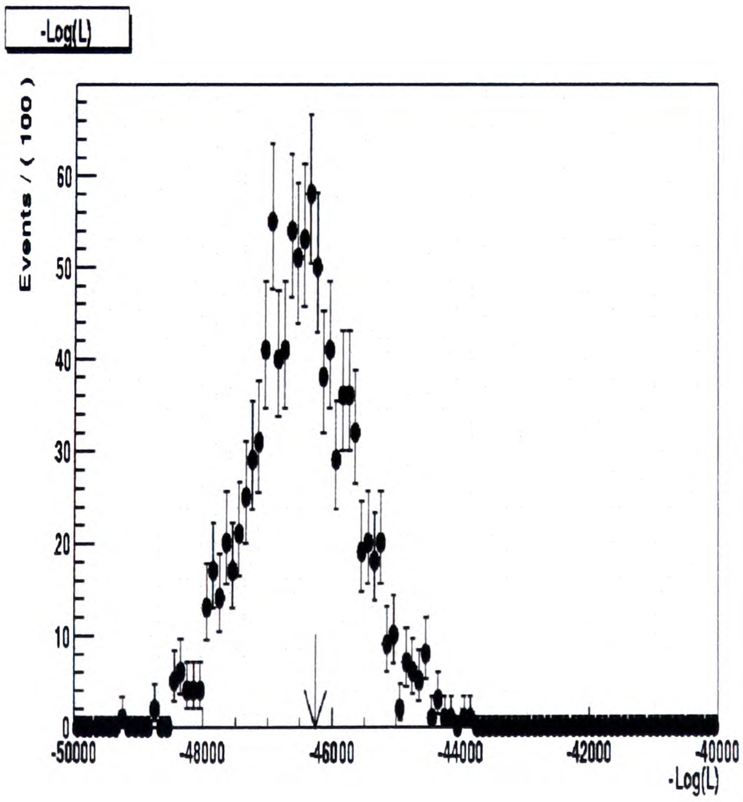

Figure 6.8: Figure showing the distribution of $-\log\mathcal{L}$ and the value obtained from data. The figure indicates that the assumed background model agrees well with data.

N_{total} Input	$B\bar{B}$ Input	$N_{K^{*0}\pi^0}$ Input	$\mu(N_{\text{sig}})$ fit	$\mu(N_{q\bar{q}})$ fit	μ(Bias)	$\mu(-\log\mathcal{L}_{\text{max}})$
I: Pure toy Monte Carlo.						
3605	0.0	25	26.5 ± 9.5	3578.5 ± 60.0	0.06	−46250
II: Embedded signal Monte Carlo and toy continuum.						
3605	0.0	25	25.7 ± 9.5	3579.3 ± 60.0	0.02	−46400
III: Embedded signal Monte Carlo, Monte Carlo $B\bar{B}$ and toy continuum.						
3605	60.0	25	26.4 ± 9.5	3578.6 ± 60.0	0.06	−46400
IV: $B^0 \to K^+K^-\pi^0$ and toy continuum.						
3610	30.0	0.0	3.0 ± 6.0	3580 ± 60.0	0.90	-
IV: $B^0 \to K^+\pi^-\pi^0$ and toy continuum.						
3640	60.0	0.0	30.0 ± 9.0	3580 ± 60.0	0.50	-

Table 6.8: Fit results. 500 experiments each. I: Pure toy, II: Embedded signal Monte Carlo and toy continuum, III: Embedded signal Monte Carlo, $B\bar{B}$ Monte Carlo and toy continuum, IV: Embedded signal-like crossfeed $B\bar{B}$ Monte Carlo and toy continuum.

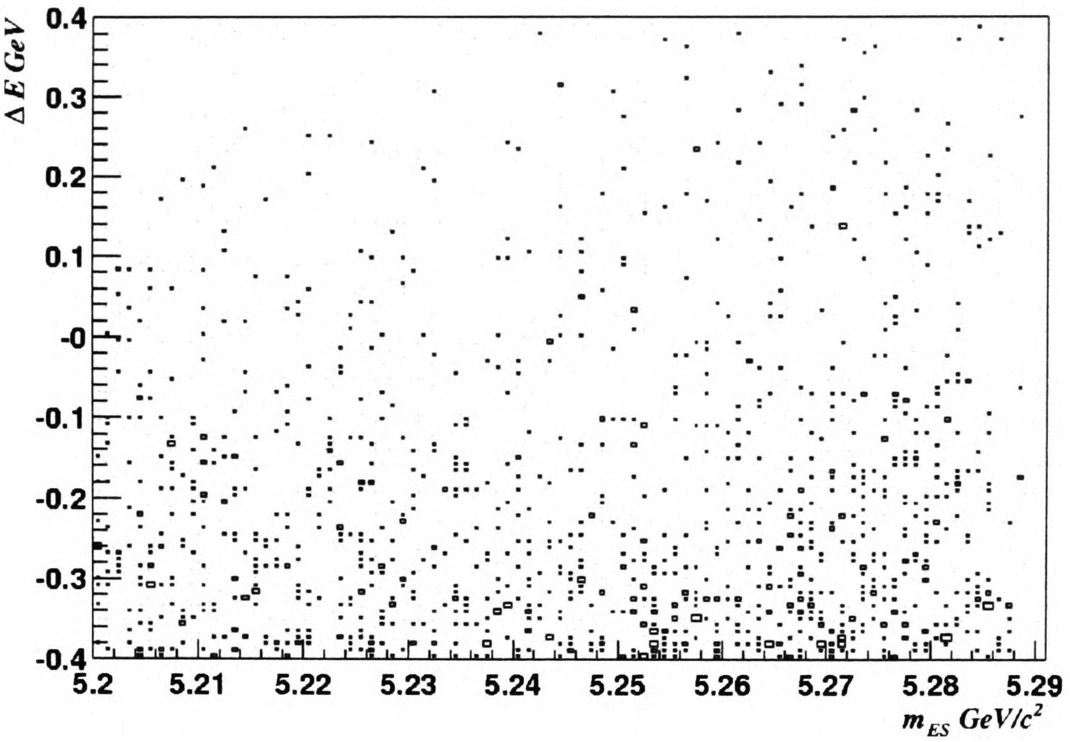

Figure 6.9: $B\bar{B}$ generic Monte Carlo showing the amount of $B\bar{B}$ pollution in the ΔE variable for the $B^0 \to K^{*0}\pi^0$ analysis.

described in section 6.4.

6.8 Fit results

This section discusses the results of the extended maximum likelihood fit. In table 6.9 we give the values of all fixed model parameters and also the values of those parameters obtained from the fit. All values of the fixed parameters are the data corrected values and for each parameter we give the largest error. These corrections are discussed in the systematics section 6.9. For those parameters determined from the fit, the errors shown are determined using the methods discussed in section 4.8.2. We obtain $N_{\rm sig} = 20.0^{+9.7}_{-8.6}$ and $N_{q\bar{q}} = 3474 \pm 59$. The correlation matrix for the floating fit parameters is given in table 6.10.

As discussed in the previous chapter in the Gaussian approximation, the log likelihood distribution is given by $e^{-\chi^2/2}$. From this, the significance of the result can be determined by computing $\sqrt{-2\log(\mathcal{L}/\mathcal{L}_{S=0})}$ as described in section 5.8. From figure 6.11 a significance of 2.77 is obtained. The projection methods described in section 5.8 will

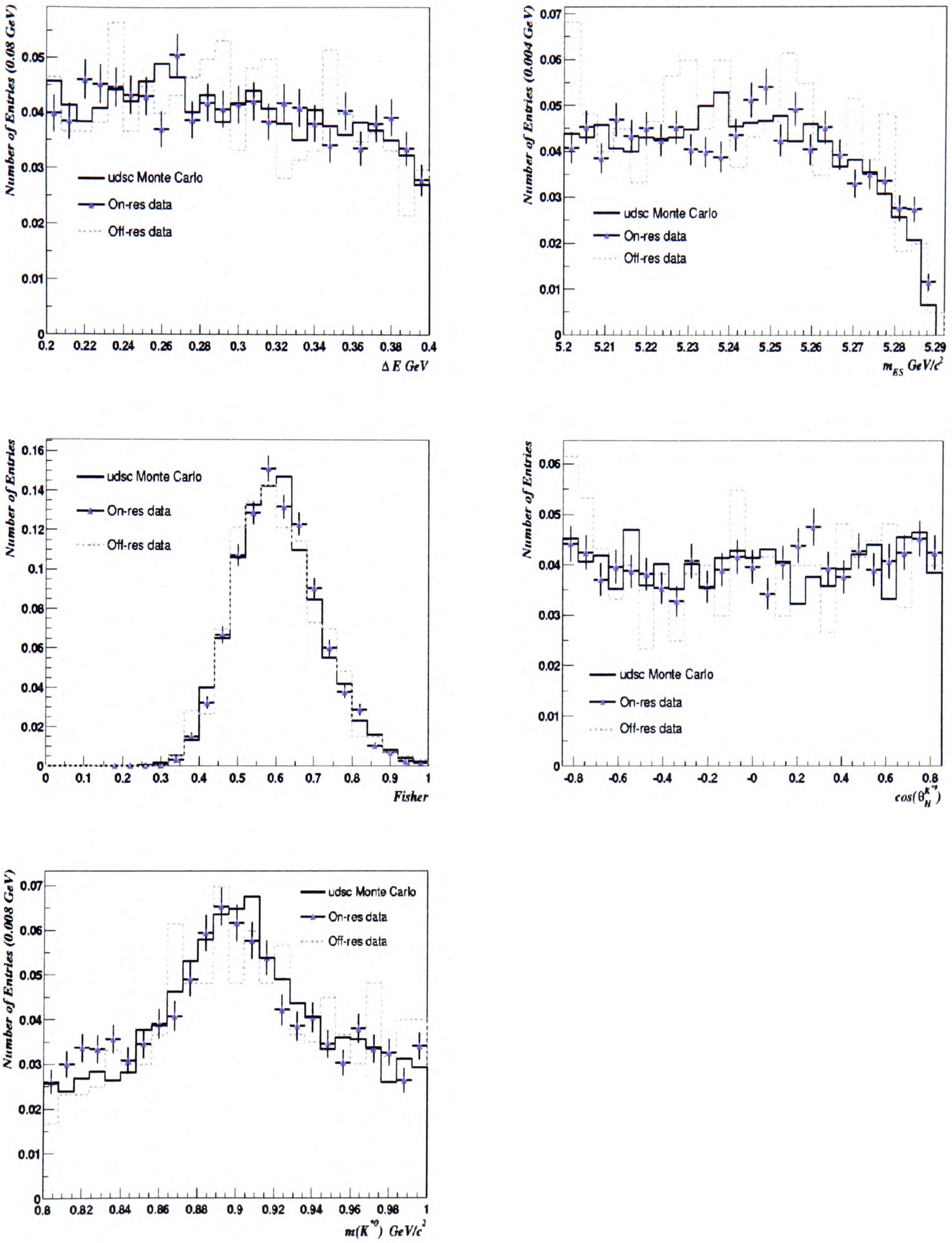

Figure 6.10: udsc Monte Carlo, off-peak and on-peak data comparison for $0.2 < \Delta E < 0.4$ GeV. The selection cuts are described in the text of section 6.7.

not show a clear signal excess. In figure 6.12 we show the projection plots where there is evidence for a signal, especially in the m_{ES} distribution. We must substract our estimated number of 3.53 crossfeed background from the determined signal yield. After subtracting the crossfeed we retain a significance of 2.14.

Parameter	Description	Value
$N_{\rm sig}$	Number of $B^0 \to K^{*0}\pi^0$	$20.0^{+9.7}_{-8.6}$
$N_{q\bar{q}}$	Number of $q\bar{q}$ background	3474 ± 59
$B^0 \to K^{*0}\pi^0$ fit parameters. All parameters fixed		
$\sigma(m_{ES})$	Resolution of the Crystal Ball for m_{ES} signal MeV/c^2	2.80 ± 0.15
$\mu(m_{ES})$	Mean of the Crystal Ball for m_{ES} signal GeV/c^2	5.280 ± 0.0002
α	m_{ES} C.B. parameter	1.591 ± 0.026
n	m_{ES} C.B. order parameter	2.556 ± 0.103
$\mu_C(\Delta E)$	Mean of core Gaussian component of ΔE signal MeV	-3.6 ± 2.5
$\sigma_C(\Delta E)$	Resolution of core ΔE Gaussian GeV	0.032 ± 0.001
$\mu_T(\Delta E)$	Mean of tail Gaussian component of ΔE signal GeV	-0.045 ± 0.003
$\sigma_T(\Delta E)$	Resolution of tail ΔE Gaussian GeV	0.070 ± 0.003
Frac$_C$	Core Gaussian contribution	0.448 ± 0.044
$\sigma(\mathcal{F})$	Width of signal Fisher Gaussian	0.087 ± 0.001
$\mu(\mathcal{F})$	Mean of signal Fisher Gaussian	0.433 ± 0.001
$\Gamma(K^{*0})$	Width of K^{*0} resonance GeV/c^2	0.050 ± 0.005
$\mu(K^{*0})$	Mass of K^{*0} resonance GeV/c^2	0.896 ± 0.002
$c_1(\cos(\theta_H^{K^{*0}})$	Linear coefficient of the $\cos(\theta_H^{K^{*+}})$ distribution	-0.011 ± 0.009
$c_2(\cos(\theta_H^{K^{*0}})$	Quadratic coefficient of the $\cos(\theta_H^{K^{*+}})$ distribution	0.996 ± 0.002
$q\bar{q}$ background parameters determined from fit.		
ξ	ARGUS $q\bar{q}$ background shape parameter	-25.37 ± 1.95
$c_1(\Delta E)$	ΔE linear coefficient of $q\bar{q}$ background	-1.514 ± 0.196
$\mu(\mathcal{F})$	Mean of background Fisher Gaussian	0.527 ± 0.004
$\sigma_L(\mathcal{F})$	Left width of background Fisher Gaussian	0.082 ± 0.002
$\sigma_R(\mathcal{F})$	Right width of background Fisher Gaussian	0.118 ± 0.003
$q\bar{q}$ background parameters fixed in fit.		
m_0	Endpoint of ARGUS function.	5.29
$\Gamma(K^{*0})$	Width of K^{*0} resonance in $q\bar{q}$ background GeV/c^2	0.050 ± 0.005
$\mu(K^{*0})$	Mass of K^{*0} resonance in $q\bar{q}$ background GeV/c^2	0.896 ± 0.002
$c_1(K^{*0})$	Linear K^{*0} background component in $q\bar{q}$ background	0.0 ± 0.05
Frac$_{K^{*0}}$	Contribution of K^{*0} component	0.291 ± 0.032
$c_1(\cos(\theta_H^{K^{*0}})$	Coefficient of the $\cos(\theta_H^{K^{*0}})$ distribution	0.00 ± 0.1

Table 6.9: Values of the fit parameters and signal yield results of the final fit to data.

Parm	$\xi(m_{ES})$	$\mu(\mathcal{F})$	$\sigma_L(\mathcal{F})$	$\sigma_R(\mathcal{F})$	$c_1(\Delta E)$	$N_{q\bar{q}}$	$N_{\rm sig}$
$\xi(m_{ES})$	1						
$\mu(\mathcal{F})$	0.011	1					
$\sigma_L(\mathcal{F})$	-0.012	0.827	1				
$\sigma_R(\mathcal{F})$	0.003	0.773	0.570	1			
$c_1(\Delta E)$	0.014	0.001	-0.006	0.000	1		
$N_{q\bar{q}}$	0.038	0.006	-0.008	0.002	0.012	1	
$N_{\rm sig}$	-0.213	-0.039	0.044	-0.013	-0.062	-0.128	1

Table 6.10: Correlation between the yields and floating parameters in the maximum likelihood fit to data.

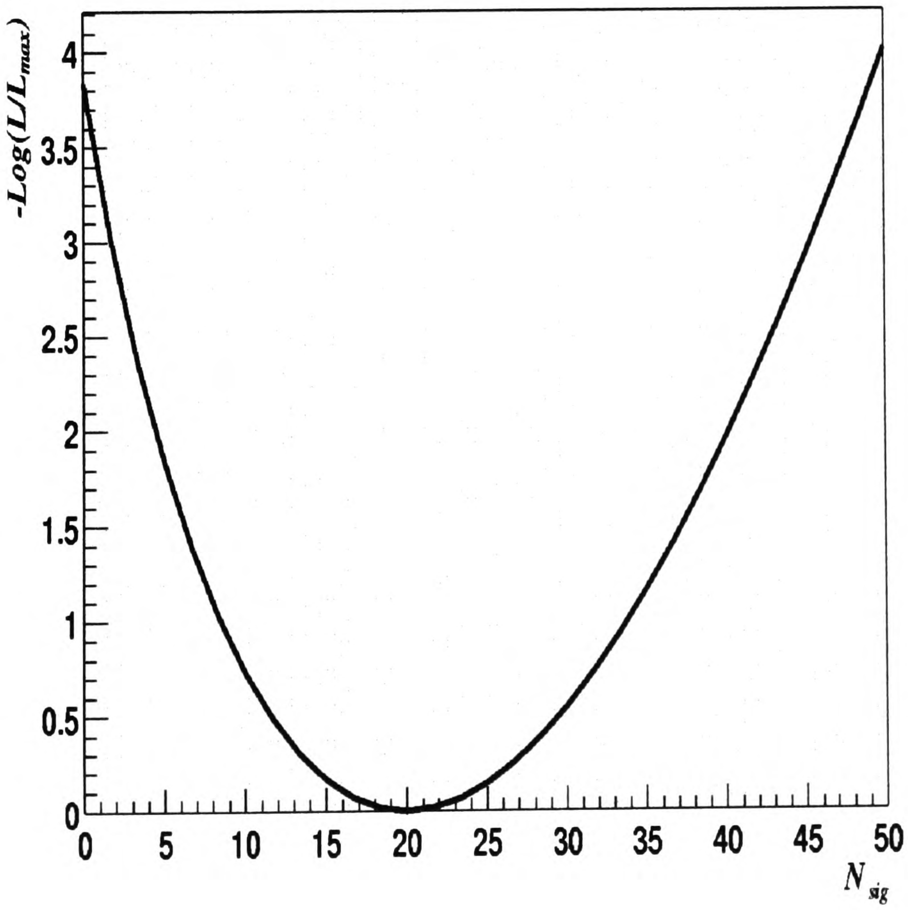

Figure 6.11: $-log(\mathcal{L}/\mathcal{L}_{\rm max})$ scan for the $B^0 \to K^{*0}\pi^0$ analysis.

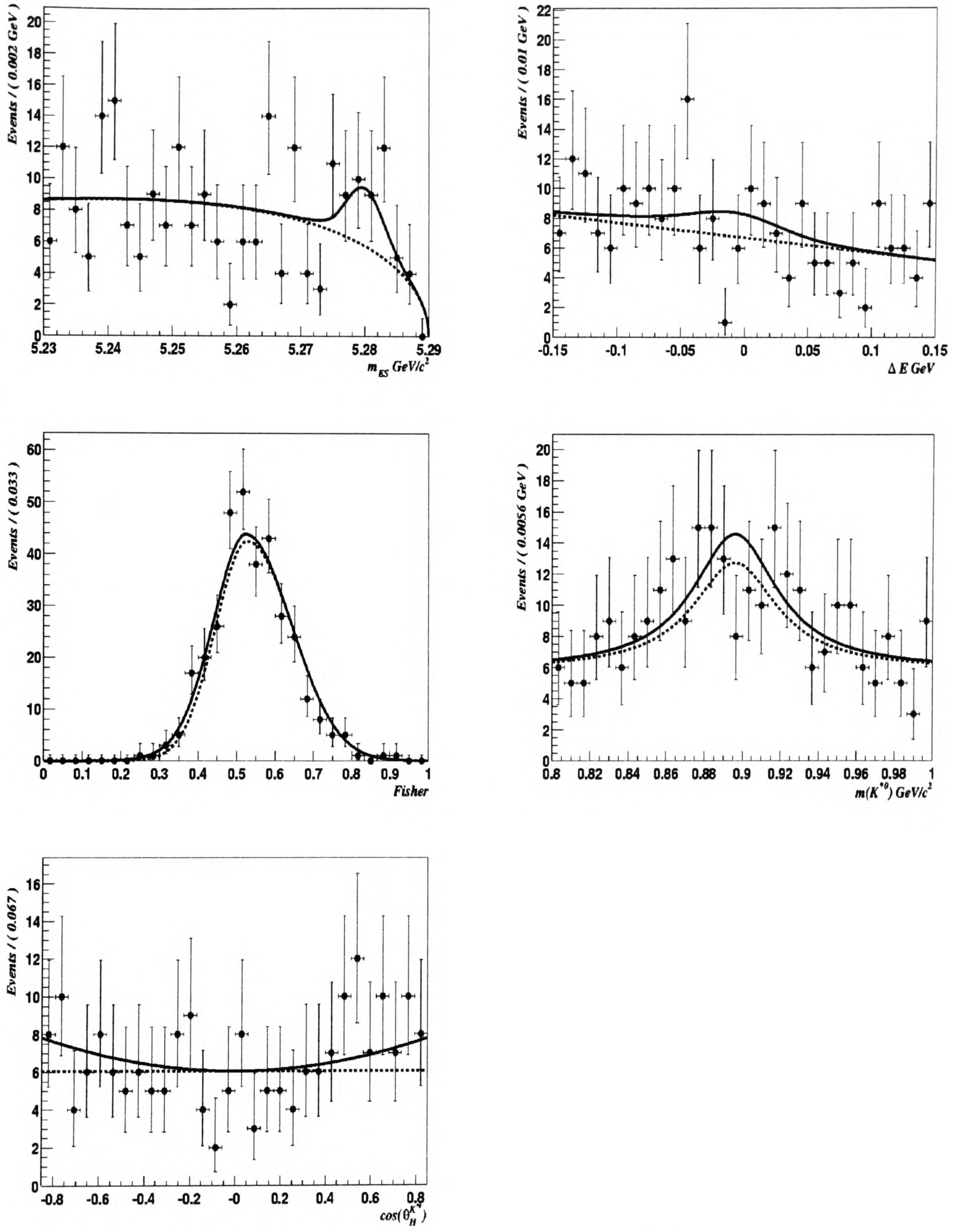

Figure 6.12: Projection plots for the analysis of $B^0 \rightarrow K^{*0}\pi^0$ made using the method discussed in section 5.8 for data. The projected variables are respectively m_{ES}, ΔE, $\mathcal{F}$, $m(K^{*0})$, $\cos(\theta_H^{K^{*0}})$. The projections shown are: background and signal PDFs (solid line) and background only PDFs (dashed line).

6.9 Systematics

In this section we introduce the sources of systematic errors for the analysis of $B^0 \to K^{*0}\pi^0$, $K^{*0} \to K^+\pi^-$. We follow an almost identical procedure as in section 5.9.1 for the $B^0 \to K^{*+}\pi^-$ analysis. The principal differences are due to the PDF model which we now discuss.

6.9.1 Model PDF systematics

Determining the corrections to each of the fit variables follows closely that of section 5.9.5. For ΔE, m_{ES}, we use the same corrections obtained from the $B^+ \to \bar{D}^0\pi^+$, $\bar{D}^0 \to K^+\pi^-\pi^0$. The largest correction is due to shifting the mean value of the ΔE distribution. The mode $B^0 \to \bar{D}^0\pi^0$, $\bar{D}^0 \to K^+\pi^-$ can not be used as a control sample as it has a branching fraction of $11.02 \pm 0.5 \times 10^{-6}$ comparable to the signal mode. Thus, not enough statistics are available to accurately determine corrections to the Monte Carlo. As a cross-check we looked at the correction in the mean of ΔE obtained from $B^+ \to \bar{D}^0\rho^+$, $\bar{D}^0 \to K^+\pi^-$, $\rho^+ \to \pi^0\pi^+$. This mode can have a fast π^0 (as in $K^{*0}\pi^0$) due to the polarisation of the ρ. The assigned systematic error of 2.5 MeV [56] easily incorporates any differences due to the presence of a fast π^0. For $\mathcal{F}$, $m(K^{*0})$ and $\cos(\theta_H^{K^{*0}})$ we follow the exact same procedure as in the $B^0 \to K^{*+}\pi^-$ analysis. For the background model we only need to consider systematic corrections for the $K^{*0}(892)$ and $\cos(\theta_H^{K^{*0}})$ variables which are held fixed. We use the following prescription for the background $K^{*0}(892)$:

- We fix the K^{*0} parameters to the PDG [15] values.
- $\mathrm{Frac}_{K^{*0}}$: In order to account for any possible $B\bar{B}$ component we take $\mathrm{Frac}_{K^{*0}} = 0.291^{+0.034}_{-0.031}$ from on-peak data in the $0.2 < \Delta E < 0.4$ side band.
- $c_1(K^{*0})$: There is little sensitivity to this parameter thus we fix $c_1(K^{*0}) = 0.0$. We determine the systematic error as the difference between the fitted $c_1(K^{*0})$ value in on-peak data and zero. This results in a systematic error of 0.05.

For the background $\cos(\theta_H^{K^{*0}})$ distribution we expect the distribution for background to be flat. Thus, in the fit we fix $c_1(\cos(\theta_H^{K^{*0}})) = 0.0$. We determine a systematic error as the difference between the fitted[1] linear coefficient $c_1(\cos(\theta_H^{K^{*0}}))$ and zero. This results in a systematic error of 0.1.

6.9.2 Maximum likelihood fit yield error

The statistical and systematic uncertainties on the M.L. signal yields due to the modelling of the PDFs are determined by varying each model parameter within 1σ of their fitted values while performing the full extended likelihood fit. The dominant errors are the systematic uncertainties discussed in the last section. We use the resulting change in the signal yields to determine a systematic uncertainty on the signal yield (N_{sig}) due to the PDF model. The results are shown in table 6.11 for each of the discriminating fit variables. We obtain a total systematic error of 3.4 events which corresponds to 17% of the nominal fitted yield.

Var	m_{ES}		ΔE		$\cos(\theta_H^{K^{*0}})$		K^{*0}		$\mathcal{F}$	
$\pm\sigma$	+	-	+	-	+	-	+	-	+	-
$\Delta(N_{\text{sig}})$	1.273	0.842	0.538	1.695	1.117	1.168	2.465	−0.473	1.263	1.074
$\Delta(N_{q\bar{q}})$	−1.262	−0.924	−0.582	−1.706	−0.892	−0.942	−2.501	0.421	−1.255	−1.171
Background										
$\Delta(N_{\text{sig}})$	-	-	-	-	0.874	1.296	0.630	1.597	-	-
$\Delta(N_{q\bar{q}})$	-	-	-	-	−1.012	−1.243	−0.713	−1.527	-	-

Table 6.11: Change in nominal fitted yields due to the uncertainty on the PDF model. Each parameter is varied within $\pm 1\sigma$ of their nominal fit values.

6.9.3 $B\bar{B}$ crossfeed background

In sections 5.5 and 6.6 we calculated the number of signal-like crossfeed events from the dominant $B^0 \to K^+K^-\pi^0$, $B^0 \to K^+\pi^-\pi^0$ modes and other smaller contributions given in table 6.7. We find that $3.53 \pm 0.71_{fit} \pm (0.61 \pm 3.02)_{\mathcal{BR}(B\bar{B})}$ events must be substracted from the signal fit yield. The first error arises from the uncertainty in the number of crossfeed events used to obtain fit mis-identification efficiencies in section 6.6.1. The second error is the error due to the uncertainties on the branching

---

[1] on-peak data in the $0.2 < \Delta E < 0.4$ side band.

fractions for the B modes. We add all three errors in quadrature to determine the total systematic error on the $B\bar{B}$ crossfeed background where we obtain 3.53 ± 3.16.

Table 6.13 details the sources of systematic uncertainty for the $B^0 \to K^{*0}\pi^0$. The largest sources of uncertainty come from the π^0 and the estimation of the $B\bar{B}$ background. The $B\bar{B}$ uncertainty will only be improved through measurements of the B contamination background modes and better Monte Carlo. In table 6.12 we give all systematic corrections required to correct the signal Monte Carlo efficiency. In table 6.13 we give the systematic errors arising from the efficiency corrections, number of $B\bar{B}$ pairs and signal fit yield. For each of the corrections we add the errors in quadrature.

Table 6.12: The systematic correction factors required to correct the Monte Carlo efficiency for $B^0 \to K^{*0}\pi^0$, $K^{*0} \to K^+\pi^-$.

Source	% M.C. correction in $\mathcal{BR}(B^0 \to K^{*0}(K^+\pi^-)\pi^0)$
$K^\pm/\pi^\pm$ tracking	0.984
π^0 γ smearing	0.991
Kaon ID	0.975
Total	0.951

Table 6.13: Sources of systematic uncertainties in the measurement of $\mathcal{BR}(B^0 \to K^{*0}\pi^0, K^{*0} \to K^+\pi^-)$.

Source	% Uncertainty in $\mathcal{BR}(B^0 \to K^{*0}(K^+\pi^-)\pi^0)$
Efficiency systematic errors.	
$h^\pm$, $h = K, \pi$ track	7.0
Trk. Multiplicity	1.0
Kaon ID	2.0
π^0	5.0
$\lvert\cos(\theta_H^{K^{*0}})\rvert < 0.85$	1.0
$\lvert\cos(\theta_{\mathrm{sph}}^B)\rvert < 0.8$	5.2
Total	10.3
Systematic errors on $N_{\mathrm{B^0 \to K^{*0}}\pi^0}$	
PDF model	17.0
M.L. fit bias	6.0
Crossfeed error	15.8
Total	23.9
B counting	1.1

6.10 Branching fraction result for $B^0 \to K^{*0}\pi^0$

The branching fraction is measured as:

$$\mathcal{BR}(B^0 \to K^{*0}\pi^0) = \frac{N_{B^0 \to K^{*0}\pi^0}}{N_{B\bar{B}}\epsilon\mathcal{BR}(K^{*0} \to K^+\pi^-)\mathcal{BR}(\pi^0 \to \gamma\gamma)}. \tag{6.1}$$

Where ϵ is the Monte Carlo corrected signal efficiency $\epsilon = (13.02 \pm 0.10 \pm 1.34)\%$, $\mathcal{BR}(K^{*0} \to K^+\pi^-) = 0.667$, $\mathcal{BR}(\pi^0 \to \gamma\gamma) = 98.798 \pm 0.032$ and $N_{B^0 \to K^{*0}\pi^0} = N_{\text{sig}} - N_{\text{Xfeed}}$ where N_{sig} is the signal category fit yield and N_{Xfeed} is the number of $B\bar{B}$ crossfeed. The resulting branching fraction is determined to be:

$$\mathcal{BR}(B^0 \to K^{*0}\pi^0) = (2.1^{+1.3}_{-1.1}\,(\text{stat}) \pm 0.6\,(\text{syst})) \times 10^{-6}. \tag{6.2}$$

Eff(%)	$\#B\bar{B}$ crossfeed	# Signal Events	$\mathcal{BR}(B^0 \to K^{*0}\pi^0)$ $\pm$ stat $\pm$ syst $\times 10^{-6}$
13.0	3.5 ± 3.2	$20.0^{+9.7}_{-8.6}$	$2.1^{+1.3}_{-1.1} \pm 0.6$

We determine the 90.0% upper limit by integrating the likelihood function:

$$\frac{\int_0^{N_{UL}} \mathcal{L}_{\max}(N)dN}{\int_0^{\infty} \mathcal{L}_{\max}(N)dN} = 90.0\%. \tag{6.3}$$

We obtain the upper limit on the branching fraction of 3.9×10^{-6} without systematics and 4.1×10^{-6} including the branching fraction systematic error of 0.6×10^{-6}. Both BELLE [32] and CLEO [33] have so far not observed any events in this decay channel. We find that the QCD factorisation prediction $(2.5^{+0.1+0.5+0.3+2.6}_{-0.1-0.4-0.3-0.5}) \times 10^{-6}$ is in good agreement with our measured value. The *BABAR* experiments data set will soon reach $200\,fb^{-1}$. With this amount of data it will be possible to provide a more precise measurement of this rare decay mode.

Bibliography

[1] Yang, C.N. and Lee, T.D. Question of parity conservation in weak interactions. *Phys. Rev.*, D104:254, 1956.

[2] Wu, C.S. *et al.* Experimental test of parity conservation in beta decay. *Phys. Rev.*, D105:1413, 1957.

[3] Goldhaber, M. *et al.* Helicity of neutrinos. *Phys. Rev.*, 109:1015, 1958.

[4] Landau, L. On the conversation laws for weak interactions. *Nucl. Phys.*, 3:127, 1957.

[5] Christenson, J. H. and Cronin, J. W. and Fitch, V. L. and Turlay, R. Evidence for the 2π decay of the K_2^0 meson. *Phys. Rev. Lett.*, 13:138–140, 1964.

[6] Sakharov, A. D. Violation of CP invariance, C asymmetry, and baryon asymmetry of the Universe. *Pisma Zh. Eksp. Teor. Fiz.*, 5:32–35, 1967.

[7] Aubert, B. *et al.* Observation of CP violation in the B^0 meson system. *Phys. Rev. Lett.*, 87:091801, 2001.

[8] Abe, K. *et al.* Observation of large CP violation in the neutral B meson system. *Phys. Rev. Lett.*, 87:091802, 2001.

[9] Kobayashi, M. and Maskawa, T. CP violation in the renormalizable theory of the weak interaction. *Prog. Theor. Phys.*, 49:652–657, 1973.

[10] Yukawa, H. On the interactions of elementary particles. *Proc. Phys. Math. Soc. Jap.*, 17:48–57, 1935.

[11] Higgs, Peter W. Spontaneous symmetry breaking without massless bosons. *Phys. Rev.*, 145:1156–1163, 1966.

[12] Chau, L.L. and Keung, W.Y. Comments on the parametrization of the Kobayashi-Maskawa matrix. *Phys. Rev. Lett.*, 53:1802, 1984.

[13] Wolfenstein, L. Parametrization of the Kobayashi-Maskawa matrix. *Phys. Rev. Lett.*, 51:1945, 1983.

[14] Editors: Battaglia, M. and Buras, A.J. and Gambino, P. and Stocchi, A. 2002. Workshop on the CKM unitarity triangle CERN, Geneva, Switzerland, 13-16 Feb 2002.

[15] Hagiwara, K. *et al.* Review of particle physics. *Phys. Rev.*, D66, 010001, 2002.

[16] Editors: Harrison, P. F. and Quinn, Helen R. The *BABAR* physics book: physics at an asymmetric B factory. SLAC-R-0504 1998.

[17] Höcker, A. and Lacker, H. and Laplace, S. and Le Diberder,F. A new approach to a global fit of the CKM matrix. *Eur. Phys. J.*, C21:225–259, 2001.

[18] Kakuno, H. *et al.* Measurement of $|V_{ub}|$ using inclusive $B \to X_u l\nu$ decays with a novel X_u reconstruction method. 2003. hep-ex/0311048.

[19] Aubert, B. *et al.* Measurement of the inclusive charmless semileptonic branching ratio of B mesons and determination of $|V_{ub}|$. *Phys. Rev. Lett.*, 92:071802, 2004.

[20] Aubert, B. *et al.* Measurement of $|V_{cb}|$ using $\bar{B}^0 \to D^{*+}l^-\bar{\nu}_l$ decays. 2003. 21st international symposium on lepton and photon interactions at high energies (LP 03), Batavia, Illinois, 11-16 Aug 2003, hep-ex/0308027.

[21] Abe, K. *et al.* Measurement of the inclusive semileptonic branching fraction of B mesons and $|V_{cb}|$. *Phys. Lett.*, B547:181–192, 2002.

[22] Aubert, B.*et al.* Measurement of the CP violating asymmetry amplitude $\sin(2\beta)$. *Phys. Rev. Lett.*, 89:201802, 2002.

[23] Abe, K. *et al.* Improved measurement of mixing-induced CP violation in the neutral B meson system. *Phys. Rev.*, D66:071102, 2002.

[24] http://www.slac.stanford.edu/xorg/hfag. May 2002. Heavy flavours averaging group.

[25] G Buchalla, A. J. Buras, and M E. Lautenbacher. Weak decays beyond leading logarithms. *Rev. Mod. Phys.*, 68:1125–1144, 1996.

[26] Buchalla, G. Heavy Quark Theory. 55th Scottish Universities Summer School in Physics: Heavy flavour physics, St. Andrews, Scotland 7-23 August 2001.

[27] Beneke, M. and Neubert, M. QCD factorization for $B \to PP$ and $B \to PV$ decays. *Nucl. Phys.*, B675:333–415, 2003.

[28] Beneke, M. and Buchalla, G. and Neubert, M. and Sachrajda, C. T. QCD factorization in $B \to \pi K$, $\pi\pi$ decays and extraction of Wolfenstein parameters. *Nucl. Phys.*, B606:245–321, 2001.

[29] Davies, C. Lattice quantum chromodynamics. 55th Scottish Universities Summer School in Physics: Heavy flavour physics, St. Andrews, Scotland 7-23 August 2001.

[30] Beneke, M. and Buchalla, G. and Neubert, M. and Sachrajda, C.T. QCD factorization for exclusive, non-leptonic B meson decays: general arguments and the case of heavy-light final states. *Nucl. Phys.*, B591:313–418, 2000.

[31] Neubert, M. Aspects of QCD factorisation. *AIP Conf. Proc.*, 602:168–179, 2001.

[32] Abe, K. *et al.* Observation of the decays $B^0 \to K^+\pi^-\pi^0$ and $B^0 \to \rho^- K^+$.

[33] Eckhart, E. *et al.* Observation of $B \to K^0_S\pi^+\pi^-$ and evidence for $B \to K^{*\pm}\pi^{\mp}$. *Phys. Rev. Lett.*, 89:251801, 2002.

[34] Chiang, C.W. Gronau, M. Luo, Z. Rosner, J.L. and Suprun, D.A. Charmless $B \to VP$ decays using flavour $SU(3)$ symmetry. 2003. hep-ph/0307395.

[35] Zeppenfeld, D. *Z. Phys.*, C8:77, 1981.

[36] Gronau, M. Hernandez, O. F. and London, D. and Rosner, J. L. Decays of B mesons to two light pseudoscalars. *Phys. Rev.*, D50:4529–4543, 1994.

[37] Gronau, M. Hernandez, O. F. London, D. and Rosner, J. L. Electroweak penguins and two-body B decays. *Phys. Rev.*, D52:6374–6382, 1995.

[38] Seeman, J. *et al.* The PEP-II storage rings. *SLAC-PUB-8786*, 2001.

[39] Stanford Linear Accelerator Center. PEP-II, An asymmetric B Factory - conceptual design report. SLAC-PUB-0418 1993.

[40] Aubert, B. *et al.* The *BABAR* detector. *Nucl. Instrum. Meth.*, A479:1–116, 2002.

[41] Billoir, P. Track fitting with multiple scattering: a new method. *Nucl. Instr. Meth.*, A225:352, 1984.

[42] Bell, R. A. *et al.* The *BABAR* superconducting coil: design, construction and test. *Nucl. Phys. Proc. Suppl.*, 78:559–564, 1999.

[43] Sjostrand, Torbjorn. PYTHIA 5.7 and JETSET 7.4. 1995. CERN-TH-7112-93.

[44] D. J. Lange. The EvtGen particle decay simulation package. *Nucl. Instrum. Meth.*, A462:152–155, 2001.

[45] Agostinelli, S. *et al.* GEANT 4. A simulation toolkit. *Nucl. Instrum. Meth.*, A506:250–303, 2003.

[46] Bona, M. *et al.* Report of the tracking efficiency task force for 2001. July 2001. *BABAR* Analysis Document, BAD-324.

[47] Bellini, F. Brunet, S. and Di Lodovico, F. Comparison between Monte Carlo and data of the π^0 detection and reconstruction efficiency using τ 1-on-1 decays. September 2003. *BABAR* Analysis Document, BAD-378.

[48] Fisher, R. A. The use of multiple measurements in taxonomic problems. *Annals Eugen.*, 7:179, 1936.

[49] The CLEO collaboration, Battle, M. *et al.* Observation of B^0 Decays to two charmless mesons . *Phys. Rev. Lett.*, 71:3922–3926, 1993.

[50] Cowan, G. Statistical data analysis. *Oxford University Press,*, 1998.

[51] The ARGUS collaboration, Albrecht, H. *et al.* ARGUS: a universal detector at DORIS-II. *Nucl. Instrum. Meth.*, A275:1–48, 1989.

[52] Aubert, B. *et al.* Measurements of branching fractions and CP-violating asymmetries in $B^0 \to \rho^{\pm}h^{\mp}$ decays. *Phys. Rev. Lett.*, 91:201802, 2003.

[53] http://www.slac.stanford.edu/BFROOT/www/Physics/Tools/BetaTools/MicroNeutralKilling-RUN2.html. June 2002. *BABAR* Analysis Group.

[54] http://www.slac.stanford.edu/BFROOT/www/Physics/TrackEfficTaskForce/Recipe/GoodTracksLoose-Run2.html. June 2002. *BABAR* Analysis Group.

[55] http://www.slac.stanford.edu/BFROOT/www/Physics/Tools/Pid/PidKilling/PidKilling.html. June 2002. *BABAR* Analysis Group.

[56] Mir, L. and Gritsan, A. Search for the decays $B^+ \to \rho K^*$ and $B^+ \to \rho^0\rho^+$. July 2003. *BABAR* Analysis Document, BAD-483.

[57] Hearty, C. Measurement of the number of $\Upsilon(4S)$ mesons produced in Run I (B counting). January 2001. *BABAR* Analysis Document, BAD-134.